



SÜLEYMAN DEMİREL UNIVERSITY

JOURNAL OF CERAMICS AND COMPOSITES

VOLUME:01

ISSUE:01

YEAR:2025

ISSN:0000-0000





SÜLEYMAN DEMİREL UNIVERSITY

EDITORS-IN-CHIEF


Professor Mehmet AVCAR, PhD

 0000-0002-0689-0601

Suleyman Demirel University
Department of Civil Engineering
Isparta, Turkey

VICE EDITOR-IN-CHIEF

Assistant Professor Yasemin ŞİMŞEK TÜRKER, PhD

 0000-0002-3080-0215

Suleyman Demirel University
Department of Civil Engineering
Isparta, Turkey

EDITORS

Professor Subrata Kumar PANDA, PhD

Central University of Rajasthan,
Ajmer, Rajasthan, India

Professor Nicholas FANTUZZI, PhD

University of Bologna,
Bologna, Italy

Professor Reza KOLAHCHI, PhD

Islamic Azad University,
Jasb, Iran

Associate Professor Serap ÜNAL

Suleyman Demirel University
Isparta, Turkey

TECHNICAL EDITORS

Research Assistant Burak İKİNCİ

(Layout Editor)

Suleyman Demirel University
Isparta, Turkey

Elif ŞİMŞEK YEŞİL

(Layout Editor)

Suleyman Demirel University
Isparta, Turkey



SÜLEYMAN DEMİREL UNIVERSITY

CONTENTS

Research Articles

Finite element-based buckling analysis of bio-inspired laminated composite plates

Aman Garg1

Manufacturing methods of functionally graded materials: a comprehensive review

Burak İkinci6

Pyrite effect: correlation between compressive strength and durability properties for concrete samples

Zafer Kurt, İlker Ustabas, Muhammet Emin Aydın, Ceren İlkur Ustabas21

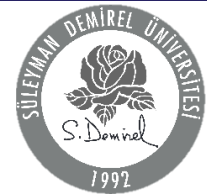
Influence of corner radius on the axial compressive behavior of FRP-confined rectangular reinforced concrete columns

Ali Juma Noorzad, Hakan Dilmaç26

Comparison of offshore fish cage flotation systems designs using finite element method

Mehmet Emin Özdemir, Şevval Öztürk, Sevil Ay, İrem Mirzaloğlu, Merve Terzi, Murat Yaylacı40





Finite element-based buckling analysis of bio-inspired laminated composite plates

Aman Garg^{a,b,*}

^aState Key Laboratory of Intelligent Manufacturing Equipment and Technology, School of Mechanical Science and Engineering, Huazhong University of Science and Technology, Wuhan, China

^bDepartment of Multidisciplinary Engineering, The NorthCap University, Gurugram, Haryana, India

Highlights

- Buckling behavior of bio-inspired laminates
- Analysis carried out using finite element method
- Lamination schemes inspired from mantis shrimp
- Lamination scheme affects free vibration behavior

Abstract

The helicoidal structures can cater to the loads effectively and efficiently without large deflections or stresses. These structures can even sustain environmental loads without failing. Also, these structures can take impact loads without failing. The present work aims to carry out buckling analysis of bio-inspired helicoidal laminated composite plates using finite element-based model within the framework of ANSYS. The plate is modeled using SOLID191 finite element (20-node 3D layered structural solid). The present model is validated by comparing the present results with those available in the literature. Influence of end conditions over the buckling behavior of bio-inspired helicoidal laminated composite plates is explored. Some new results are also presented in the present work, which will serve as the benchmark for future studies.

Information

Received: 14.11.2024
 Received in revised: 08.01.2025
 Accepted: 09.01.2025

Keywords: : Buckling, bio-inspired plate, helicoidal plate, finite element

1. Introduction

Laminated configurations are used in constructing various structures in the fields of civil, automobile, aerospace, marine, defense industries, etc. as the engineering properties in laminated structures can be modified by changing the ply-angle and thickness of each layer [1]. Thus, due to the property of tailorability possessed by laminated composite structures, these structures can sustain the loads effectively. Conventionally, the angle and the number of the ply are chosen randomly and then analyzed for different conditions under the required loading conditions.

The arrangement of tissues in the layers in the biological creatures helps in sustaining the loads in an efficient manner to which they are encountered. The venation in the leaves of the trees helps in connecting them with the branches without encountering large stresses. The elliptical shape of the shell and the material from which it is made up help in protecting him from adverse conditions and prey. The helicoidal structure is present in the various living organisms and helps in withstanding impact loading [2,3]. Even the basic life form, i.e., DNA present in the creatures possesses helicoidal structures. The beetles can

even withstand the puncture load of 23 N in its forewing area which is much higher than its fighting force [4] (Figure 1).

Several theories are available in the literature for the bending, free vibration, and buckling analysis of laminated composite and sandwich plates under various loading conditions [5–12]. Mohamed et al. [13] carried out buckling analysis of 32-layered laminated composite plate made up of helicoidal scheme using first-order shear deformation theory (FSDT). Sharma et al. [14] predicted the bending behavior of helicoidal laminated composite plates using higher order shear deformation theory. Garg et al. [15] predicted the free vibration behavior of helicoidal laminated composite plates using higher-order zigzag theory. Garg et al. [16] predicted the free vibration and buckling behavior of helicoidal laminated sandwich plates using finite element based higher-order zigzag theory. Sharma et al. [17] predicted first-ply failure load for cross- and double-helicoidal laminated sandwich plates. Due to the presence of the helicoidal schemes, the crack propagation becomes difficult within the laminate and a higher strength can be achieved.

*Corresponding author: aman_garg@hust.edu.cn (A. Garg), +86-15623020583

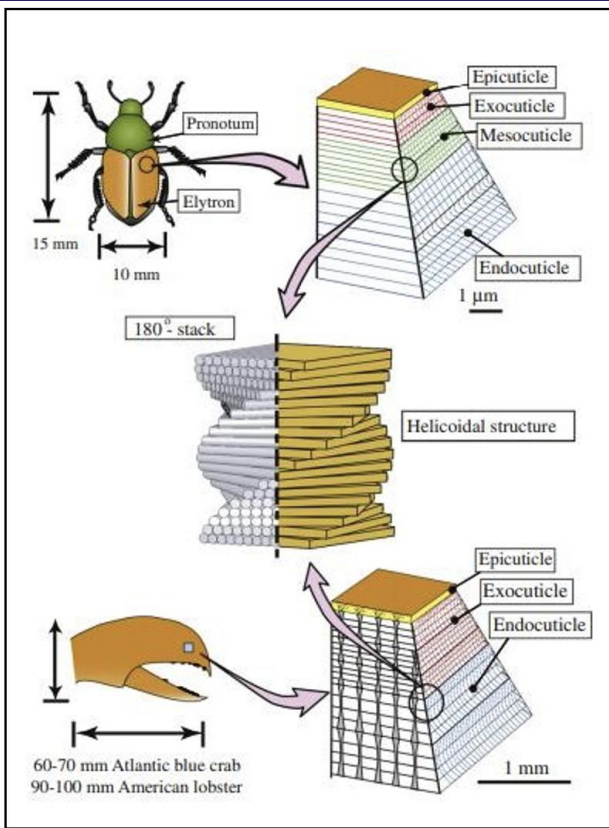


Figure 1. The hierarchical structures of the exoskeletons from *Homarus americanus*, *Callinectes sapidus*, and *Popillia japonica*. The helicoidal structural pattern is observed in different regions of all the exoskeletons [18].

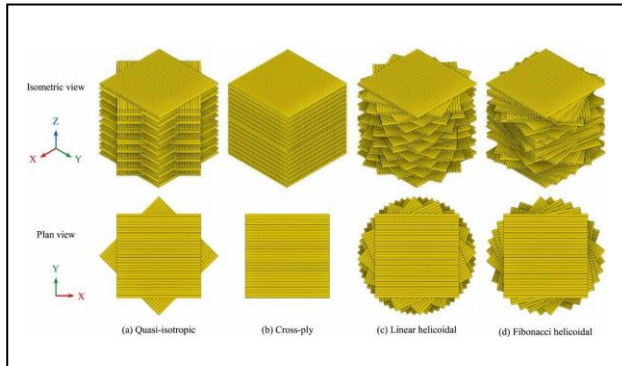


Figure 2. Different lay-up configurations of (a) quasi-isotropic (QI), (b) cross-ply (CP), (c) linear helicoidal (LH), and (d) Fibonacci helicoidal (FH) bio-inspired laminated configurations employed during the present study [4].

Singh et al. [18] in their work reported that by adopting the helicoidal schemes in laminated composite structures, the buckling strength of the plate can be increased. From the review work it has been observed that the influence of end conditions on the buckling behavior of bio-inspired helicoidal laminated composite plates is not fully explored. In the present work, an attempt has been made to carry out the buckling analysis of laminated composite plates containing bio-inspired helicoidal scheme using ANSYS. The efficiency of the present model is demonstrated by comparing the obtained results with those available obtained by Mohamed et al. [13]. Several new results are also

reported, which will serve as a benchmark for future studies in a similar direction.

2. Materials and Geometric Modeling

For modeling the helicoidal bio-inspired 32-layered laminated composite plate in ANSYS, SOLID191 finite element (20-node 3D layered structural solid) is employed as this element is specially used for modeling the laminated structures. The helicoidal schemes used during the present study are shown in Table 1 and Figure 2.

The accuracy of the results obtained using the finite element method (FEM), depends on the number of elements adopted. Therefore, at first convergence study is carried out. The material properties used for the same are: $E1/E2 = \text{Open}$, $E2 = E3 = 1E6$, $G12 = G13 = 0.5E6$, $G23 = 0.2E6$, $\nu12 = \nu13 = \nu23 = \nu32 = 0.25$, $\nu21 = 0.01$, $\nu31 = 0.01$. The value for $a/h = 20$ with all edges clamped is taken during the analysis. The results of the buckling for the convergence study are presented in Table 2 for different helicoidal schemes. The present results converges when the mesh size reaches 24×24 . Therefore, in further studies, the same mesh size is adopted. The present results are in good agreement with those reported by Mohamed et al. [13] and Garg et al. [16]. Some deviation in the present results compared to those reported by Mohamed et al. [13] because of the application of FSDT. FSDT is not able to predict the behavior of laminated structures effectively as this theory assumes constant transverse shear stresses across the thickness of the plate [20].

Table 1. Layup configuration adopted taken from Wang et al [4].

| Representation | Number of layers | Stacking sequence |
|----------------|------------------|---|
| UD | 32 | $[0^\circ/0^\circ \dots /0^\circ]$ |
| CP | 32 | $[0^\circ/90^\circ/0^\circ/90^\circ/\dots/0^\circ/90^\circ]$ |
| QI | 32 | $[0^\circ/45^\circ/90^\circ/-45^\circ]_4s$ |
| LH | 32 | $[0^\circ/24^\circ/\dots/360^\circ]_s$ |
| FH | 32 | $[0^\circ/10^\circ/10^\circ/20^\circ/30^\circ/50^\circ/80^\circ/130^\circ/210^\circ/340^\circ/190^\circ/170^\circ/360^\circ/170^\circ/170^\circ/340^\circ]_s$ |

Table 2. Validation study on buckling load $\bar{\lambda} = \lambda a^2/E_2 h^3$ of bio-inspired helicoidal laminated composite plate.

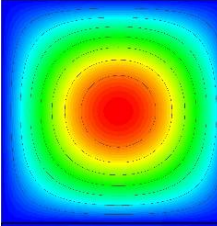
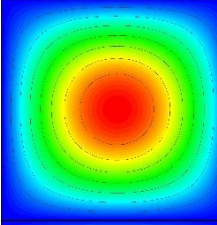
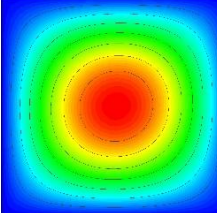
| Source | UD | LH | FH |
|---------------------|---------|---------|---------|
| Present (16 × 16) | 13.6957 | 18.2253 | 17.0588 |
| Present (20 × 20) | 12.1025 | 16.9875 | 15.8840 |
| Present (24 × 24) | 11.8259 | 15.4124 | 14.5007 |
| Present (28 × 28) | 11.8259 | 15.4124 | 14.5007 |
| Mohamed et al. [13] | 11.7802 | 16.2265 | 15.3801 |
| Garg et al. [16] | 11.7480 | 15.5931 | 14.9292 |

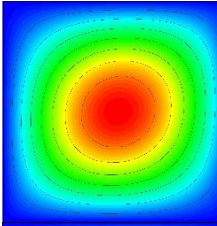
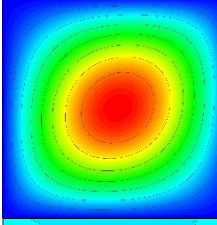
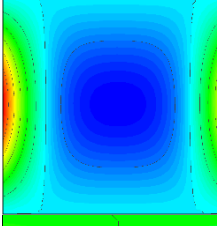
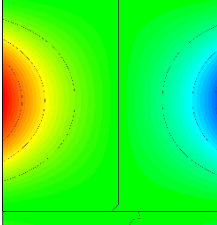
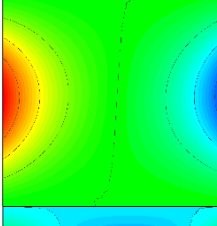
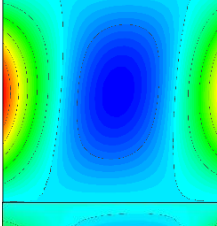
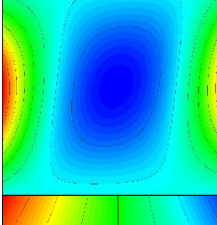
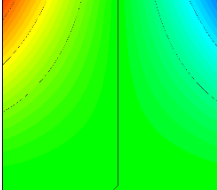
3. Results and Discussion

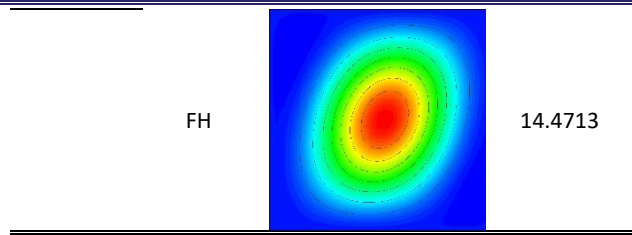
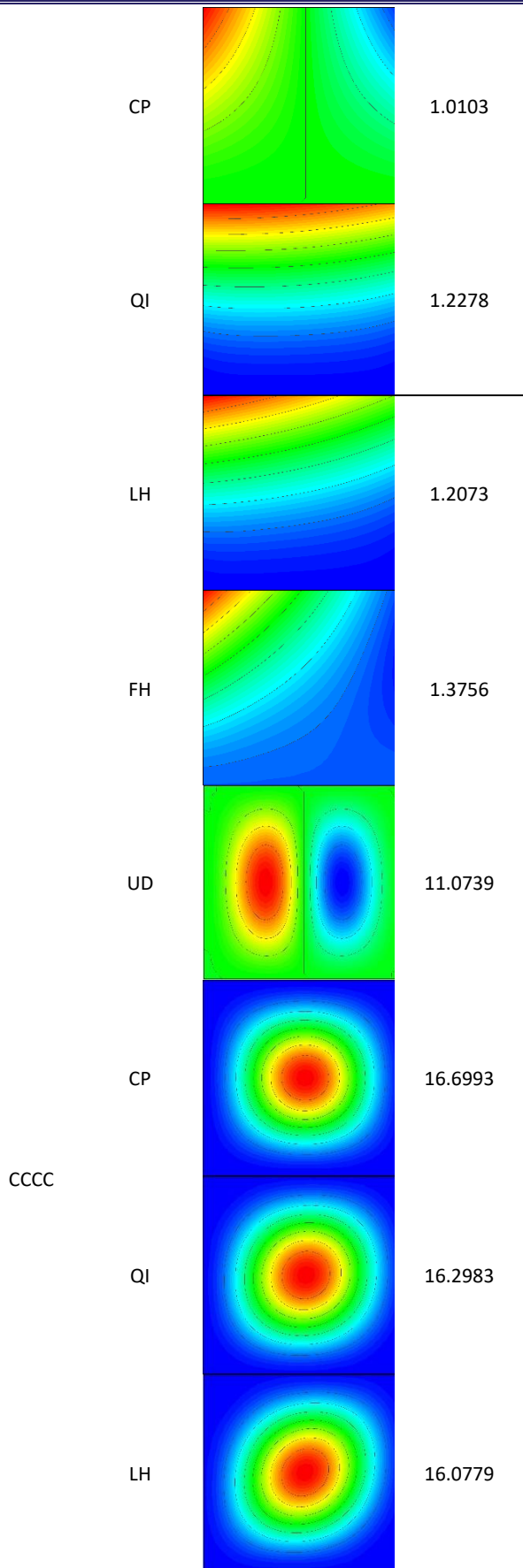
After validating the present model, the new results are presented in this section on the buckling analysis of

helicoidal laminated composite plates having different boundary conditions. The material properties used for the same are as follows: $E_1 = 131$ GPa, $E_2 = E_3 = 10.34$ GPa, $G_{12} = G_{13} = 6.895$ GPa, $G_{23} = 6.205$ GPa, $\nu_{12} = \nu_{13} = 0.22$, $\nu_{23} = \nu_{32} = 0.49$, $\nu_{21} = \nu_{31} = 0.017$. The first buckling mode shape along with the non-dimensional critical buckling load are presented in Table 3. The influence of four different boundary conditions, namely SSSS (all edges simply supported), CCCC (all edges clamped), CCFF (edges parallel to X-axis are simply supported and edges parallel to Y-axis are free), and CFFF (one edge parallel to X-axis is clamped and remaining three edges are free) on the buckling behavior of 32-layered bio-inspired laminated composite plate is studied for the different layup schemes as reported in Table 1. The maximum value for the non-dimensional critical buckling load is observed for CCCC boundary conditions and minimum for CFFF end conditions as expected. For bio-inspired laminated lay-ups, the buckling mode shape is slightly different when compared with the conventional lay-up schemes (UD, CP, and QI). Due to the presence of the corrugations, the crack propagation becomes difficult within the laminate and a higher strength can be achieved. Because of the symmetric helicoidal schemes with respect to the middle-axis of the plate, the mode shapes obtained are symmetric in nature with symmetric end conditions.

Table 3. Mode shape and non-dimensional critical buckling load for square shaped bio-inspired laminated composite plates with different layup schemes and boundary conditions ($a/h = 10$).

| Boundary condition | Layup scheme | Mode shape | Non-dimensional buckling load |
|--------------------|--------------|---|-------------------------------|
| SSSS | UD |  | 5.9473 |
| | CP |  | 6.3195 |
| | QI |  | 7.7598 |

| | | | |
|------|----|---|--------|
| CCFF | LH |  | 7.6236 |
| | FH |  | 6.9483 |
| | UD |  | 5.2493 |
| CFFF | CP |  | 8.2359 |
| | QI |  | 8.678 |
| | LH |  | 8.5283 |
| CFFF | FH |  | 6.9050 |
| | UD |  | 1.2803 |



4. Conclusion

In the present article, buckling analysis of 32-layered bio-inspired helicoidal laminated composite plate is carried out using ANSYS. Following important points are noted down during the present study:

1. Bio-inspired helicoidal laminated composite plate is found to perform better than the conventional lay-up schemes.
2. Boundary conditions widely determine the buckling behavior of bio-inspired laminated composite plates.
3. CCCC ended plate gives maximum value for non-dimensional critical buckling load, whereas CFFF end condition gives the minimum value.
4. The mode shape for bio-inspired helicoidal scheme is symmetric about the diagonal of the square, for UD, CP, and QI, the same is symmetric about the mid edge-axis and diagonals (for SSSS and CCCC boundary conditions).

Declaration of Interest Statement

The authors declare that they have no known competing financial interests or personal relationships that could have appeared to influence the work reported in this paper.

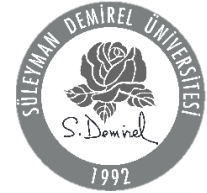
Acknowledgement

Present work received no financial grant in any form.

References

- [1] Garg, A., & Chalak, H.D. (2021). Bending analysis of laminated sandwich plates under hygrothermal loadings. *Materials Today: Proceedings*, 42, 626–630. <https://doi.org/10.1016/j.matpr.2020.11.045>.
- [2] Bouligand, Y. (1972). Twisted fibrous arrangements in biological materials and cholesteric mesophases. *Tissue Cell*, 4, 189–217. [https://doi.org/10.1016/S0040-8166\(72\)80042-9](https://doi.org/10.1016/S0040-8166(72)80042-9).
- [3] Ha, N.S., & Lu, G. (2020). A review of recent research on bio-inspired structures and materials for energy absorption applications. *Composites Part B: Engineering*, 181, 107496. <https://doi.org/10.1016/j.compositesb.2019.107496>.
- [4] Wang, H., Wang, C., Hazell, P. J., Wright, A., Zhang, Z., Lan, X., Zhang, K., & Zhou, M. (2021). Insights into the high-

- velocity impact behaviour of bio-inspired composite laminates with helicoidal lay-ups. *Polymer Testing*, 103, 107348. <https://doi.org/https://doi.org/10.1016/j.polymertesting.2021.107348>.
- [5] Reddy, J.N. (1989). On refined computational models of composite laminates. *International Journal for Numerical Methods in Engineering*, 27, 361–382. <https://doi.org/10.1002/nme.1620270210>.
- [6] Noor, A.K., & Burton, W.S. (1992). Computational Models for High-Temperature Multilayered Composite Plates and Shells. *Applied Mechanics Reviews*, 45, 419–446. <https://doi.org/10.1115/1.3119742>.
- [7] Zhang, Y.X., & Yang, C.H. (2009). Recent developments in finite element analysis for laminated composite plates. *Composite Structures*, 88, 147–157. <https://doi.org/10.1016/j.compstruct.2008.02.014>.
- [8] Liew, K.M., Zhao, X., & Ferreira, A.J.M. (2011). A review of meshless methods for laminated and functionally graded plates and shells. *Composite Structures*, 93, 2031–2041. <https://doi.org/10.1016/j.compstruct.2011.02.018>.
- [9] Sayyad, A.S., & Ghugal, Y.M. (2015). On the free vibration analysis of laminated composite and sandwich plates: A review of recent literature with some numerical results, *Composite Structures*, 129, 177–201. <https://doi.org/10.1016/j.compstruct.2015.04.007>.
- [10] Garg, A., & Chalak, H.D. (2019). A review on analysis of laminated composite and sandwich structures under hygrothermal conditions. *Thin-Walled Structures*, 142, 205–226. <https://doi.org/10.1016/j.tws.2019.05.005>.
- [11] Liew, K.M., Pan, Z.Z., & Zhang, L.W. (2019). An overview of layerwise theories for composite laminates and structures: Development, numerical implementation and application. *Composite Structures*, 216, 240–259. <https://doi.org/10.1016/j.compstruct.2019.02.074>.
- [12] Garg, A., Chalak, H.D., Belarbi, M.-O., & Zenkour, A.M. (2022). A parametric analysis of free vibration and bending behavior of sandwich beam containing an open-cell metal foam core. *Archives of Civil and Mechanical Engineering*, 22, 56. <https://doi.org/10.1007/s43452-021-00368-3>.
- [13] Mohamed, S., Mohamed, N., & Eltaher, M.A. (2022). Bending, buckling and linear vibration of bio-inspired composite plates. *Ocean Engineering*, 259, 111851. <https://doi.org/10.1016/j.oceaneng.2022.111851>.
- [14] Sharma, A., Belarbi, M.O., Garg, A., & Li, L. (2023). Bending analysis of bio-inspired helicoidal/Bouligand laminated composite plates. *Mechanics of Advanced Materials and Structures*, 0, 1–15. <https://doi.org/10.1080/15376494.2023.2214934>.
- [15] Garg, A., Belarbi, M.-O., Li, L., Sharma, N., Gupta, A., & Chalak, H.D. (2023). Free vibration analysis of bio-inspired helicoid laminated composite plates. *Journal of Strain Analysis for Engineering Design*, 030932472311604. <https://doi.org/10.1177/03093247231160414>.
- [16] Garg, A., Belarbi, M.O., Chalak, H.D., Li, L., Sharma, A., Avcar, M., Sharma, N., Paruthi, S., & Gulia, R. (2023). Buckling and free vibration analysis of bio-inspired laminated sandwich plates with helicoidal/Bouligand face sheets containing softcore. *Ocean Engineering*, 270, 113684. <https://doi.org/10.1016/j.oceaneng.2023.113684>.
- [17] Sharma, A., Tonk, A., Garg, A., Li, L., & Chalak, H.D. (2023). First-Ply Failure Analysis of Bioinspired Double and Cross-Helicoidal Laminated Sandwich Plates. *AIAA Journal*, 1–9. <https://doi.org/10.2514/1.J063176>.
- [18] Cheng, L., Thomas, A., Glancey, J.L., & Karlsson, A.M. (2010). Mechanical behavior of bio-inspired laminated composites. *Composites Part A: Applied Science and Manufacturing*, 42, 211–220. <https://doi.org/10.1016/j.compositesa.2010.11.009>.
- [19] Singh, A., Garg, A., & Sahu, V. (2023). Stability and mode shape analysis of doubly-and cross-helicoidal laminated sandwich plates inspired from dactyl's club. *Mechanics of Advanced Materials and Structures*, 1-17. <https://doi.org/10.1080/15376494.2023.2263000>.
- [20] Garg, A., & Chalak, H.D. (2021). Analysis of non-skew and skew laminated composite and sandwich plates under hygro-thermo-mechanical conditions including transverse stress variations. *Journal of Sandwich Structures and Materials*, 23, 3471–3494. <https://doi.org/10.1177/1099636220932782>.



Manufacturing methods of functionally graded materials: a comprehensive review

Burak İkinci^{a,*}

^aDepartment of Civil Engineering, Engineering and Natural Sciences Faculty, Suleyman Demirel University, Isparta, Turkey

Highlights

- Introduction
- FGM manufacturing methods
- Classification of FGM manufacturing methods
- Comparison of FG manufacturing methods

Abstract

Various problems arise in traditional composites and the gradient of these materials needs to be controlled for more specific purposes. At this stage, functionally graded materials, which are a more specific area of advanced composites, come into play. High strength-to-weight ratio, wear resistance, thermal insulation, controlled porosity and many other features can be obtained by using functionally graded materials. A wide variety of functionally graded materials and their manufacturing methods are available. In this study, the classifications of properties of functionally graded materials and manufacturing methods in the literature are examined. The basic principles for each method are presented. In addition to the advantages and disadvantages of the methods, the difficulties in the production phase are also examined.

Information

Received: 11.12.2024
 Received in revised: 14.01.2025
 Accepted: 17.01.2025

Keywords: Functionally graded, classification, manufacturing methods, composites, advantages

1. Introduction

Composites, produced by combining two or more materials, offer versatile properties for various applications. Conventional composites generally consist of fibers that serve as reinforcement and a matrix medium in which these fibers are dispersed. Although there are lots of advantages, combining different materials can cause problems such as stresses because of the differences in thermal expansion coefficients, residual stresses occurring, and surface incompatibilities after production [1-3]. Functionally graded materials (FGM) offer solutions in various fields. FGMs are used in areas by modifying material properties, such as aerospace, electronics, military industry, biomedical areas, the textile industry and more. FGM is produced by gradually changing the material content in directions. Concrete, industrial tools, ship hulls, microchips are artificial FG materials. Bones, bamboo and teeth etc. can be given as examples of natural FGM structures. Just as the density of bone increases progressively closer to the joints, optimizing its structural integrity for higher strength. Similarly, bamboo demonstrates a gradual transition from a soft, flexible outer layer to a harder, more rigid inner core. The primary advantage of FGMs is to eliminate the stress jumps at interfaces that occur in conventional

composites. FGMs have features such as high strength-to-weight ratio, the ability to be designed according to the desired feature, lightness, damping and vibration control, and resistance to high temperature differences. Despite their advantages, FGMs face challenges such as complex manufacturing processes, high costs, and limited applications.

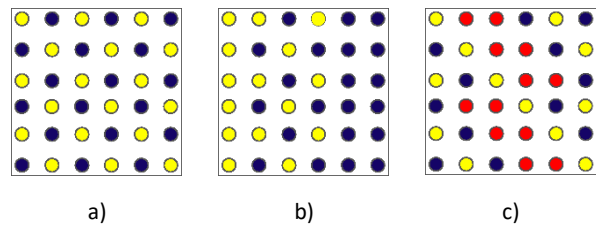


Figure 1. Variation of a) typical composite, b) single FGM, c) double FGM [7]

The mechanical properties of an object produced with an FGM, with the selection of direction or more than one direction; are defined by volume fraction and material gradient. Linear gradients promote uniform stress distribution, while nonlinear gradients can induce more localized stress fields. The differences in characteristics between typical composites and FGMs are shown in Figure 1. In contrast to typical composites, a single FGM

*Corresponding author: burakikinci@sdu.edu.tr (B., İkinci), +90-246-211-1222

can be produced by a single dispersed ingredient or phase that is not evenly distributed throughout the matrix [4-6].

Double FGM requires multiple components or phases [7]. Functionally Graded Materials (FGMs) are characterized by variations in their composition and microstructural properties. These variations, which define the material gradient, can be categorized into four main types: fraction gradient, shape gradient, size gradient, and orientation gradient, as illustrated in Figure 2, which depicts different gradient methodologies explaining material gradient [8].

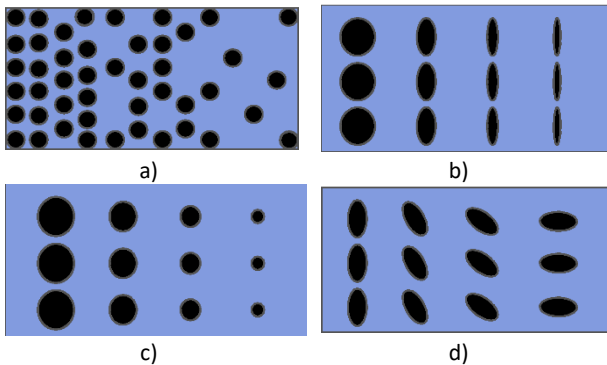


Figure 2. Different gradient types of FGM: a) fraction, b) shape, c) size, d) orientation

FGM, in terms of material composition change; It is divided into three types according to whether it changes ladder, sudden, and gradually, as shown in Figure 3 [9].

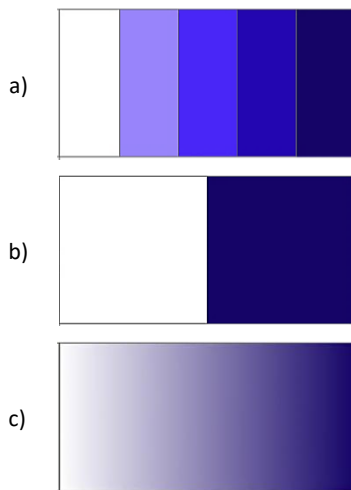


Figure 3. Variation of gradient transition types in FGM: a) ladder, b) sudden, c) gradual

Composition change of the material can be through longitudinal or the thickness of the structure as shown in Figure 4.

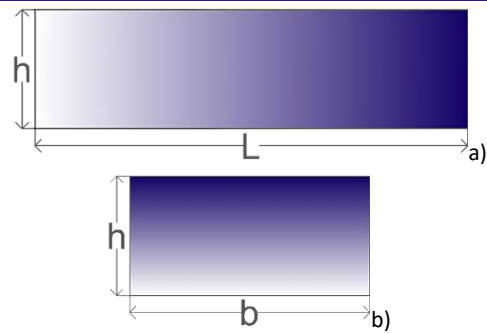


Figure 4. Variation of material properties along a) longitudinal direction, b) thickness direction [10]

Additionally, composition, microstructure, and porosity are the types FGMs based on grading [6,10]. For FGMs with porous structure, porosity can be divided into two different types as shown in Figure 5.

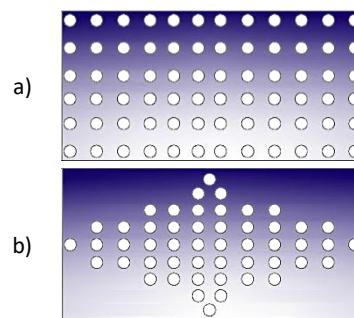


Figure 5. Porous FGM with a) even, b) uneven distribution

In some cases, superior properties need to be achieved, such as thermal stress. Multi-directional (MD) FGMs are designed by changing material properties in more than one direction as can be seen in Figure 6. MD FGMs vary from simple 1D variations observed in layered structures like the thickness of a plate, where material properties gradually transition, to 2D variations like those seen in the surface of a plate with varying thermal conductivity, and complex 3D gradients found in advanced components such as turbine blades with intricate internal cooling channels, where material composition graded to withstand complex stress and temperature gradients [12].

However, the successful realization of FGMs hinges on the development of advanced manufacturing techniques that can accurately control the gradient profile and microstructure.

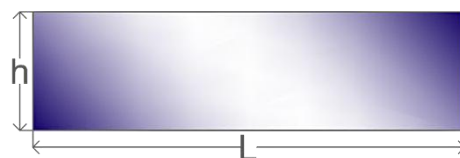


Figure 6. A 2D FGM in which material properties are varied in the longitudinal and thickness direction

This review covers state-of-the-art manufacturing processes for FGMs, including traditional techniques such as vapor deposition methods, and powder metallurgy, as

well as emerging additive manufacturing methods such as fused deposition modeling. Furthermore, it compares characteristics of products such as porosity, improved strength, high cost, production difficulty and more. By understanding the strengths and limitations of these techniques, the design and manufacturing of FGMs can be optimized to meet specific performance requirements [12,13-15].

2. FGM Manufacturing Methods

FGM manufacturing methods are comprehensively examined in this section. The strengths and weaknesses of each approach are analyzed, and the characteristics of FGM products produced by different methods (such as porosity, strength, cost, and production difficulty) are compared to guide the selection of the most suitable manufacturing process for specific applications [6].

2.1. Vapor deposition methods

Vapor deposition methods are used for coating purposes to increase material properties, such as corrosion and wear resistance. While offering precise control over composition, these methods can be slow and energy intensive. These methods sometimes produce hazardous by-products and mostly not suitable for bulk production [16-19]. A comparison of these methods is shown in Table 1.

2.1.1. Chemical vapor deposition [CVD]

In CVD, a gas or vapor undergoes a chemical reaction on the surface, forming a solid coating [19]. CVD is widely used in the electronics industry for thin film deposition. A schematic of CVD setup is shown in Figure 7.

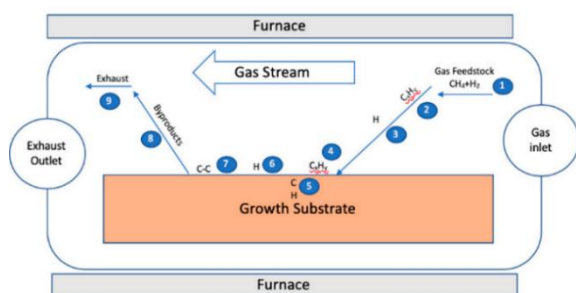


Figure 7. A schematic representation of thermal CVD growth of graphene, taken from [20]

2.1.2. Physical vapor deposition [PVD]

PVD involves deposition onto a surface through physical reactions. Pure coatings can be obtained using PVD. Automotive and aerospace industries products made by this method [17]. A schematic of PVD setup is shown in Figure 8.

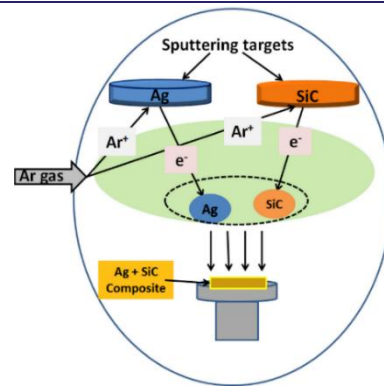


Figure 8. A schematic representation of manufacturing Ag based composite prepared by PVD, taken from [21]

2.1.3. Jet vapor deposition (JVP)

In JVD, a carrier inert gas is used to deposit the material. The vaporized material is directed to the material surface with a high-speed jet flow. It can be applied in a low vacuum environment and that allows use of multiple jet tips, making this method relatively faster [16].

2.1.4. Directed vapor deposition (DVD)

DVD enables the efficient use of electron beams on various materials, including highly reactive metals. The gas is delivered by focusing on a specific area. Provides more controllable and better targeted coverage [18].

2.2. Plasma spray (PS)

PS involves plasma sputtering of metals, ceramics and polymers. Different types of materials can be deposited simultaneously with different melters, but obtaining a homogeneous distribution can be challenging. Polymers, ceramics and metals can be coated. Additionally, PS can be combined with vapor deposition and other methods [20-22].

Table 1. Comparison of vapor deposition methods [16-21]

| Method | Advantages | Disadvantages |
|--------|--|--|
| CVD | Suitable for thin films, req. low temps. proc. | Complex equipment, toxic byproduct |
| PVD | High quality coatings, strong adhesion, low cost | Low deposition. rate, unfit for comp. geometry |
| JVD | Fast coating, suitable in low vacuum conditions | Complex equipment, energy consumption |
| DVD | Precision coating, high efficiency | Complex equipment, high cost |

Table 2 presents an overview of the temperature ranges and typical precursors employed in various vapor deposition techniques. CVD is operated within a range of 200-1600°C, depending on the reaction temperature. PVD has a very broad temperature range, 25-1200°C. JVD is generally operated between 100-300°C for organic molecules, and it can increase for inorganics. DVD is operated between 200-600°C [16-19,23,24].

Table 2. The comparison of applied temperature range and precursors of vapor deposition methods

| Method | Temperature Range (°C) | Typical Precursors |
|--------|------------------------|-----------------------------|
| CVD | 200-1600 | Halides, Metals, Organics |
| PVD | 25-1200 | Metals, Ceramics, Alloys |
| JVD | 100-300 | Organic/Inorganic Molecules |
| DVD | 200-600 | Organic/Inorganic Molecules |

2.3. Powder metallurgy (PM)

PM is used in the production of metals with varying melting points. The method involves combining, compressing and sintering two or more different materials, resulting in a porous structure. High cost of powder, and relatively low strength are drawbacks of this method. However, it results in fewer defects and cracks. PM enables the production of metal-ceramic composites, as well as machine parts and magnetic materials [28-31]. A schematic of PM process is given in Figure 9.

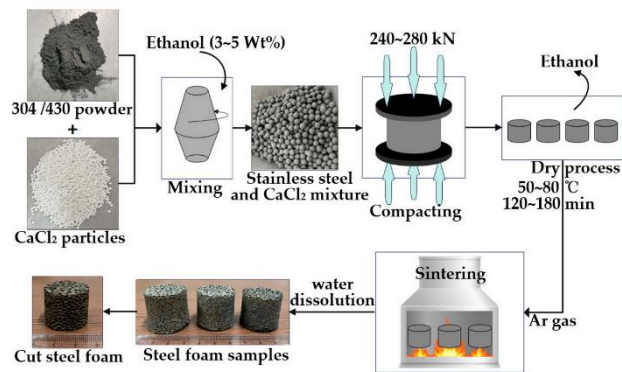


Figure 9. A schematic representation of manufacturing stainless steel foam using PM, taken from [32]

2.4. Self-propagating high-temperature synthesis (SHS)

SHS is a method based on an exothermic reaction occurring in an ignited mixture. It is applied to ceramics, metal alloys, and nanocomposites. Metallic foams are used in the production of ceramic composites and for surface hardening of metals. Although SHS requires higher temperatures and longer processing times relatively, its results are more pure products [26,33-35].

2.5. Friction stir processing (FSP):

FSP is a solid-state processing method used to modify the microstructure of metal. A tool is immersed into the workpiece and rotated to generate frictional heat, the resulting heat and pressure cause the material to deform plastically, forming a new microstructure with new properties. FSP offers detailed control over the materials microstructure, resulting in improving its mechanical properties, while at the same time providing relatively less time and low energy consumption. The method is used in the production of metal and ceramic-reinforced

composites, and graded foams. However, surface defects on product and wear may occur in the tools used [36-37].

2.6. Casting methods

Casting methods offer ability to produce different shapes and varying sizes, low tooling costs, and high production rates, but have limited microstructure control, potential for defects, and often require post-processing. A general comparison of casting methods is provided in Table 3.

2.6.1. Centrifugal casting

In this method, molten metal mix is poured into a rotating mold and subjected to high-pressure centrifugal force. The material is graded by utilizing the effect of rotation and the density difference of the materials. It provides continuous grading, can be applied to cylindrical shapes and is suitable for large-scale casting [38-40]. A schematic of centrifugal casting method is given in Figure 10.

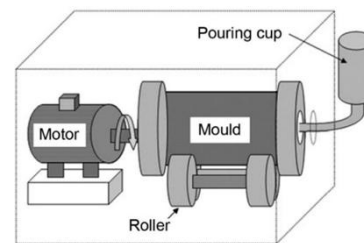


Figure 10. A schematic representation of Centrifugal Casting setup, taken from [41]

2.6.2. Tape casting

Tape casting is frequently used in the production of ceramic materials as thin layers. It also enables producing flat and thin parts over a wide area. It is particularly effective in the production of gradient materials thinner than 1 mm [42].

2.6.3. Slip casting

In this method, a pre-prepared liquid poured into a porous mold. The liquid is absorbed by the mold, leaving behind a solid layer. This process is often used for producing complex shapes and large volumes of ceramic products. Slip casting can be combined with centrifugal casting method, magnetic field or pressure. Pressure slip cast ceramics show improved mechanical properties [43].

2.6.4. Gel casting

In this method, a prepared powder is mixed with monomer solution and poured into a mold. After, the molded part is rested to be dried and proceeds to sintering. Viscosity during casting can be changed by applying heating or cooling during production. This method is environmentally friendly and can create complex shaped products [44-46].

2.6.5. Freeze casting

Freeze casting is used to obtain mostly dense ceramic that has highly controlled, complex pore structures. Metals, ceramics, polymers and composites are used in this method. The drying process of this may be time consuming. It has applications in energy storage and biomedical field [47].

2.6.6. Cast-decant-cast (CDC)

CDC based on casting layers with different material properties on top of each other. Gradient thickness can be controlled, and the thickness of the layers is limited. CDC is unsuitable for complex geometry production. Mold can be used repeatedly [48-49].

Table 3. Comparison of casting methods [34-49]

| Method | Advantages | Disadvantages |
|---------------------|--|--|
| Centrifugal Casting | Fit for cylindrical components, high production rates | Limited to cylindrical shapes, specialized equipment is needed |
| Tape Casting | Fit for thin, flat components, thin-film gradients | Limited to simple shapes, post-process is required |
| Slip Casting | Fit for complex shapes and large volumes, can be combined | Time-consuming, slurry control is important |
| Gel Casting | Eco-friendly, Fit for complex shapes, controlled viscosity | Sensitive to conditions, post-process is required |
| Freeze Casting | Fit for porous structures, various materials | Time-consuming, and specialized equipment is needed |
| CDC | Simple, inexpensive, controlled layer thickness | Limited to simple shapes and gradient profiles |

2.7. Additive manufacturing methods (AM):

Complex structured products and controlled microstructure can be obtained by AM which product is modeled by CAD or CAM. An after process may be required for these methods. A comparison of AM methods, and the materials being used for each method, as well as type of process applied are given in Table 4 and Table 5, with respect. Some of the AM methods, e.g. FDM, are slow and energy consuming when considered volume produced [6,45,50].

2.7.3. Stereolithography (SLA)

SLA uses laser to selectively cure a liquid photopolymer resin layer by layer. It is able produce 3D complex models. Only one material can be printed at a time and the product may need to be supported during the process [50-52]. SLA is fitting for producing prototypes and

biomedical applications. A typical SLA machine can be seen in Figure 11.

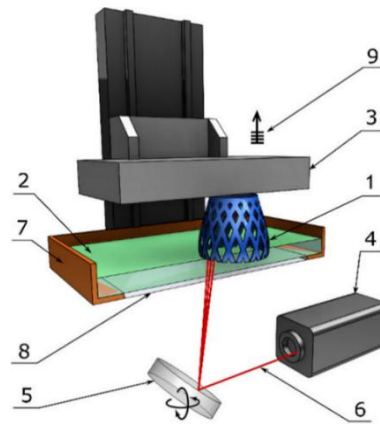


Figure 11. Components of A typical SLA machine: 1) Printed part, 2) liquid resin, 3) building platform, 4) UV laser source, 5) axis scanning mirror, 6) beam, 7) resin tank, 8) window, and 9) elevation layer-by-layer, taken from [53]

2.7.2. Solid ground curing (SGC)

SGC is curing a liquid photopolymer resin layer by layer using a projector. It's a laser-based (LB) relatively fast process but suffers from accuracy issues and material limitations [50,51].

2.7.3. Liquid thermal polymerization (LTP)

In LTP, layers of heat-sensitive polymers hardened layer by layer using laser heat. There are few research on this method in the literature [50,51].

2.7.4. Beam interference solidification (BIS)

BIS uses two laser beams to solidify liquid resin. The interference pattern of the beams creates a 3D structure within the resin. This technique is also still under development and has not yet been commercialized [50,51].

2.7.5. Holographic interference solidification (HIS)

By exposing the resin to the holographic image, the entire surface is solidified in HIS. This method hasn't been commercialized [50,51].

2.7.6. Fused deposition modelling (FDM)

FDM extrudes molten materials layer by layer to create 3D objects. This process is commonly used to produce lightweight structures. Widely used in aerospace, automotive, and biomedical applications [48,49]. FDM has lesser precision compared to SLA [54-56]. A modified schematic of FDM 3D polyether ether ketone (PEEK) printer is given in Figure 12.

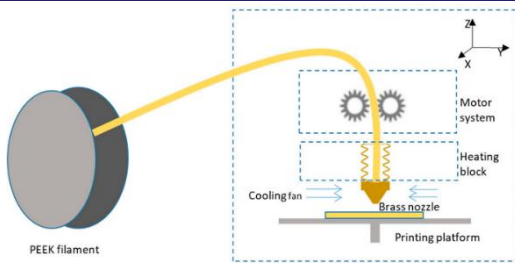


Figure 12. A schematic representation of FDM 3D PEEK printer, modified and taken from [57]

2.7.7. Material jetting [MJT]

MJT deposits tiny droplets of liquid material onto a build platform. These droplets, typically photopolymer resins, are cured with UV light to form solid structures [58]. Widely used in biomedical applications and investment casting. A schematic of MJT is given in Figure 13.

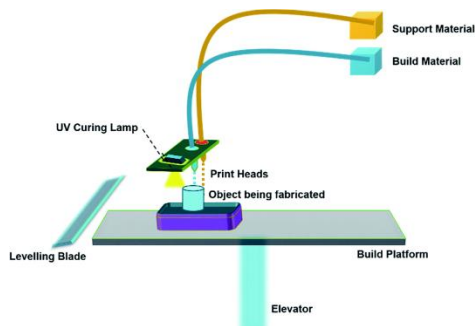


Figure 13. A schematic representation of MJT, taken from [59]

2.7.8. Binder jetting [BJ]

BJ selectively deposits a liquid binder onto a powder bed to create a 3D object. Binder jetting relies on a binding agent to adhere the particles together. It is not suitable for structural parts [58]. BJ is used to produce large cast molds and low-cost metals.

2.7.9. Selective laser melting (SLM)

In SLM, a high-powered laser is used to fuse metal powder layer by layer. This technology is increasingly being used to fabricate porous metal implants, which mimic the structure of natural bone and promote better integration with body [60]. SLM is widely used for automotive and aerospace, printing metal alloys. A schematic of SLM is given in Figure 14.

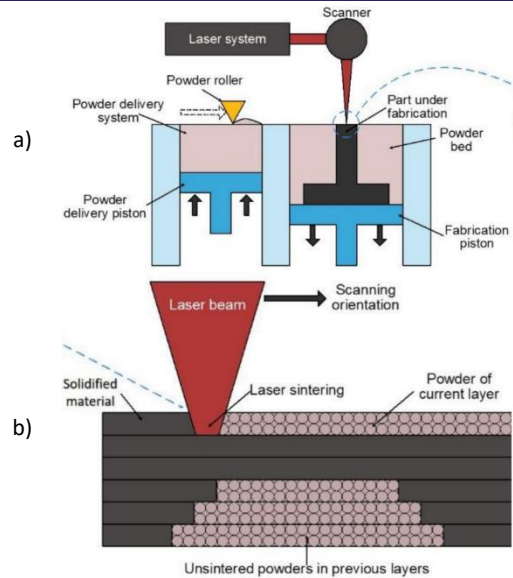


Figure 14. A schematic representation of a) SLM and b) closer look to laser-substrate region, taken and modified from [62]

2.7.10. Selective laser sintering (SLS)

SLS is a time and cost saving manufacturing process where a laser beam is used to selectively fuse powdered material under the melting point, mostly polymers, layer by layer then creating a 3D object such as detailed automotive and aerospace parts. Due to sintering, the product has a porous structure, and the mechanical strength of material is lower in SLS than in SLM. [61,62].

2.7.11. Laser cladding (LC)

LC is based on melting metal powder with a high-powered laser and depositing it onto a substrate layer by layer. LC is mainly used for surface modification, repair, and coating applications of ceramics, metals and composites [63,64]. A schematic of LC setup is given in Figure 15.

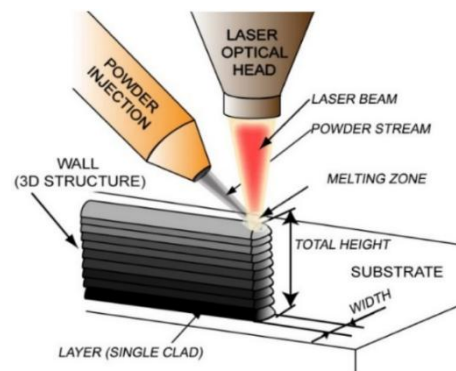


Figure 15. A schematic representation of LC setup, taken from [64]

Table 4. Comparison of AM methods [50-52,58,60,61]

| Method | Advantages | Disadvantages |
|-----------------|--|--|
| SLA | Detailed surfaces, biocompatible materials | High cost, limited volume |
| SGC | Fit for large parts | No commercial use |
| LTP | Fit for large parts, fast production | Less accuracy, |
| BIS | Fit for complex geometries, high precision | No commercial use |
| HIS | Fit for large surfaces, fast production | No commercial use |
| FDM | Desing flexibility, low cost | Slow production, poor surface quality |
| MJT | Fit for complex geometries, high precision, variety part shapes | High cost, slow producing, low strength |
| BJ | Fit for large parts, fast production., extensive materials, low cost | Low detailing, post processing might need |
| SLM | Fit for complex geometries, high strength, porosity | High cost, limited part size |
| SLS | Fit for complex geometries, extensive materials, high strength | Unfit for complex geometries, slow producing |
| LC | Surface coating-repair, wear resistance | High cost, porosity, inaccuracy |
| LENS | Fit for complex geometries, porosity | Poor surface quality, manufacturing defects |
| SPS | Rapid process, low sintering temps. | High cost, limited product size |
| LOM | Eco-friendly, size flexibility, low cost | Narrow material choice |
| EBM | Pure product, high strength | High cost, high energy consumption, relies on powder |
| Infiltration | Fit for thin layer production, high strength | Production difficulty |
| Electrospinning | High precision, high tensile strength | Degradation, dissolution, low strength |

2.7.12. Laser engineered net shaping (LENS)

LENS uses a high-powered laser, melting metal powder and depositing it layer by layer to create a 3D object. LENS allows for the direct fabrication of complex shapes with high precision. Powder characteristics, thermal properties and laser absorption influences the process. Larger volume can be produced with LENS, compared to SLM LENS is also used for repair and doesn't require post-processing [65]. A schematic of LENS given in Figure 16.

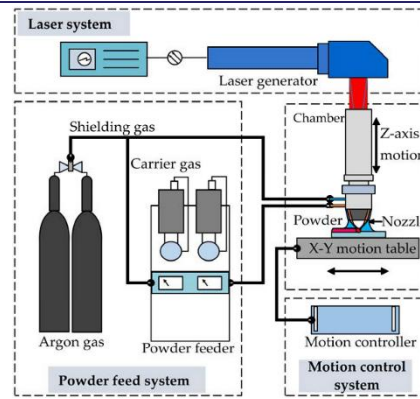


Figure 16. A schematic representation of LENS, taken from [66]

2.7.13. Spark plasma sintering (SPS)

SPS conjoins powdered materials with high density in a very short time and at low temperatures. Electricity is used to create sparks, and bonds are formed between materials. It is used to produce ceramics, metals, and composite materials [61]. High strength and high-wear resistance machine parts and materials can be produced. A schematic of SPS is given in Figure 17.

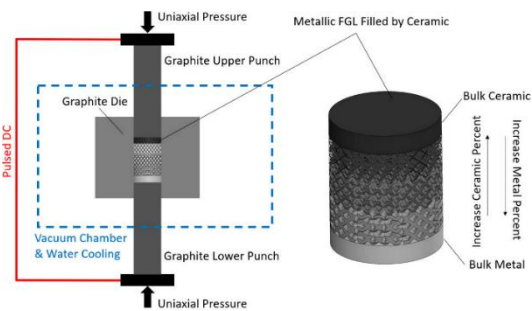


Figure 17. A schematic representation of ceramic-metal composite produced by SPS, taken from [67]

2.7.14. Laminated object manufacturing (LOM)

2D and 3D objects can be produced by LOM, layering sheets of material, and then cutting away the excess material. LOM relies on adhesives for bonding and widely used producing polymer, metal and paper laminates [68].

2.7.15. Electron beam melting (EBM)

EBM uses electron particle beam to melt powder metals, fusing the melted powder into a solid layer. It requires minimal post-processing [69]. EBM is being used in automotive, aerospace and biomedical industry. A comparison between composite material produced using EBM and SLM is given in Figure 18.

Beam-based AM methods exhibit a range of processing temperatures and power levels depending on the energy source and material. SLA uses UV light to cure liquid resins at ambient temperatures and very low power. LENS and SLM are used for melting metals, operate at high temperatures (higher than 1000°C) and utilize high-power lasers in the near-infrared spectrum. SLS operates at

sintering temperatures below the material's melting point. LOM, bonds sheet materials at much lower temperatures. EBM, distinct from the laser-based processes, utilizes a high-power electron beam to melt metal powders in a vacuum, operating at elevated temperatures [6,45-52,54,55,58].

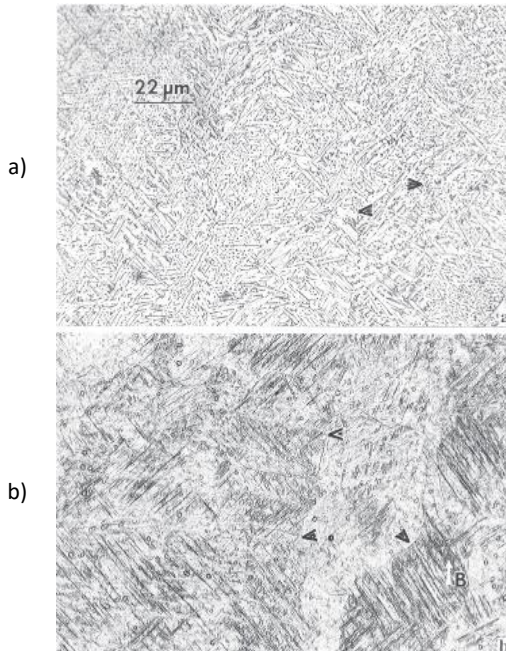


Figure 18. Comparison of microstructures for Ti-6Al-4V produced using a) EBM and b) SLM. (Arrow tips indicate columnar grain boundaries), taken from [70]

2.7.16. Infiltration

This method is used to create ceramic matrix composites by filling the pores of a ceramic preform with a molten metal. It is usually used for metal-ceramic composites. Oxidation and interface reactions may occur [71,72].

2.7.17. Electrophoretic deposition (EPD)

Charged particles suspended in a liquid are deposited onto an electrode under the influence of an electric field. EPD is used for producing automotive parts and conductive ceramic and coatings, with a continuous gradient [25]. A schematic of EPD setup is given in Figure 19.

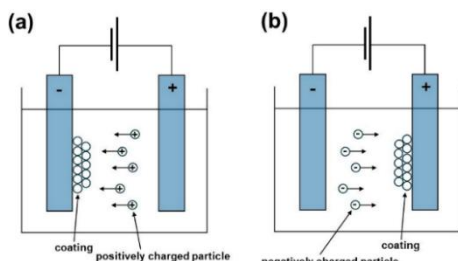


Figure 19. A schematic representation of a) cathodic and b) anodic EPD setup, taken from [73]

2.7.18. Electrospinning

Electrospinning uses a high voltage to draw a liquid substance into fibers that can be controlled at the nanometer scale. Biomedicine, nanofiber reinforced composites, electronics and optical devices are manufactured by this method. It is a relatively simple method [74-77]. A schematic of the electrospinning setup is given in Figure 20.

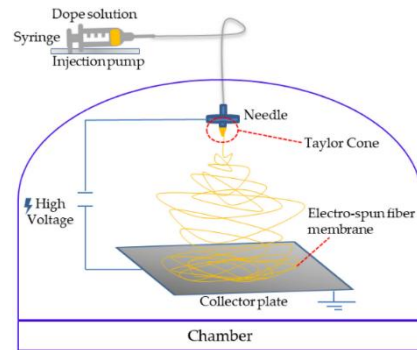


Figure 20. Schematic representation of electrospinning setup, taken from [78]

Table 5. Materials and process types of AM methods

| Method | Materials | Process Type |
|-----------------|---------------------------------------|---------------------------|
| SLA | Polymer, ceramic, composite, hydrogel | LB |
| SGC | Polymer | LB |
| LTP | Polymer | LB |
| BIS | Polymer | LB |
| HIS | Polymer | LB |
| FDM | Polymer, composite, ceramic, hydrogel | Thermal Extrusion |
| MJT | Polymer | Material jetting |
| BJ | Metal, polymer ceramic | Liquid binding |
| SLM | Polymer, metal, ceramic | LB |
| SLS | Polymer, ceramic, composite | LB |
| LC | Metal | LB |
| LENS | Metal, ceramic, composite | LB |
| SPS | Metal, ceramic | Electricity forming |
| LOM | Paper, polymer, metal, ceramic | Adhesive usage |
| EBM | Metal | Electron beam |
| Infiltration | Metal, ceramic | Injection molting |
| EPD | Polymer, ceramic, metal | Electric field |
| Electrospinning | Polymer, ceramic, composite | High voltage-spin forming |

3. Classification of FGM Manufacturing Methods

Extensive research has been conducted on FGM methods in literature, exploring their potential for diverse engineering applications. The type of process (solid, liquid, or deposition) affects the final product's properties based on the heat, pressure, and forces involved during manufacturing. To begin, a general comparison of methods based on state of product during process is shown in Figure 21 [6,8-11,24,25,50-52,55,58,68,71]. Solid states contain powder materials whereas liquid state includes molten.

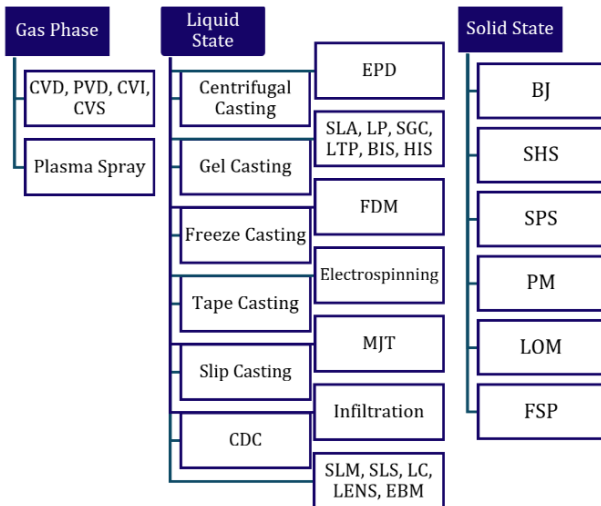


Figure 21. Classification of FGM manufacturing methods based on products state during process

As can be seen from Table 6 modified from [6], a comparison of FGM manufacturing methods based on FGM products size can be made. Bulk methods are most suited for process 3D objects, while thin methods, known as coating techniques, are inappropriate for creating structural designs [6,25,45]. Bulk and thin film methods can be combined and used to create components with optimized performance.

Additionally, based on the number of process steps, equipment requirements, and the degree of control over the microstructure and composition gradient, classification of methods are concluded, as shown in Figure 22 [109-140].

Lastly, another classification of manufacturing methods is conventional methods and additive methods. Conventional methods include casting, vapor deposition, SHS, and PM, whereas other methods are referred to as additive, as shown in Figure 23.

Table 6. Manufacturing methods based on size of FG product

| Size | Methods |
|---------------|-------------------------------------|
| Thin | CVD, PVD, JVD, DVD [27] |
| | Plasma Spray [79,80] |
| | EPD [81,82] |
| | LC [39] |
| Bulk | Centrifugal Casting [83,84] |
| | Gel Casting [85,86] |
| | Freeze Casting [86] |
| | Tape Casting [87,88] |
| | Slip Casting [89-91] |
| | CDC [92,93] |
| | SLM, SLS, LENS, EBM [60,61,65] |
| | SLA, LP, SGC, LTP, BIS, HIS [96,97] |
| | MJT [6,7] |
| | BJ [6,7] |
| | FDM [98-100] |
| | Electrospinning [100,101] |
| | Infiltration [71,72] |
| | SHS [33,34] |
| SPS [102] | |
| PM [28,103] | |
| LOM [104] | |
| FSP [105,106] | |

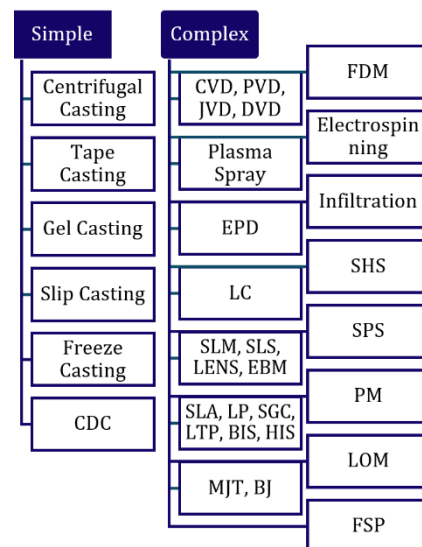


Figure 22. Relative complexity of methods

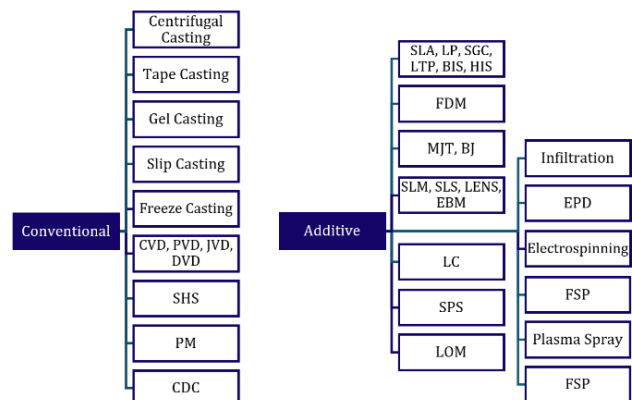


Figure 23. Conventional and additive methods, taken and modified from [6,8-11,19,21,120,125]

4. Conclusion

This review has comprehensively explored the diverse manufacturing techniques of FGMs, which is a unique approach to material design by enabling tailored properties within a component, mitigating interfacial stresses and enhancing mechanical performance compared to conventional composites. Applications of FGM span diverse fields, including aerospace, electronics, and biomedicine. This review examined a range of FGM manufacturing methods which selection of the appropriate method depends on the desired material properties, geometric complexity, production volume, and budget.

5. Discussion

The practical application of FGMs is directly linked to advanced production methods. Each method has advantages and disadvantages. AM methods are promising FGM manufacturing methods that have excellent design flexibility and ability to create complex geometries. However, AM also has limitations, including relatively slow processing speeds and high energy consumption. Therefore, future research should focus on optimizing process parameters, developing innovative energy-efficient techniques for example, exploring hybrid manufacturing approaches, and adopting a life-cycle assessment perspective for FGM products to promote sustainable manufacturing practices. This will facilitate wider application of FGMs in varying industrial sectors.

Declaration of Interest Statement

The author declares that he has no known competing financial interests or personal relationships that could have appeared to influence the work reported in this paper.

References

- [1] Wang, S. S. (1983). Fracture mechanics for delamination problems in composite materials. *Journal of Composite Materials*, 17(3), 210-223. <https://doi.org/10.1177/002199838301700302>
- [2] Gürdal, Z., Haftka, R. T., & Hajela, P. (1999). Design and optimization of laminated composite materials. John Wiley & Sons.
- [3] Nikbakt, S. K. M. S. S., Kamarian, S., & Shakeri, M. (2018). A review on optimization of composite structures Part I: Laminated composites. *Composite Structures*, 195, 158-185. <https://doi.org/10.1016/j.compstruct.2018.03.063>
- [4] Şimşek, M. (2015). Bi-directional functionally graded materials (BDFGMs) for free and forced vibration of Timoshenko beams with various boundary conditions. *Composite Structures*, 133, 968-978. <https://doi.org/10.1016/j.compstruct.2015.08.021>
- [5] Najibi, A., & Mokhtari, T. (2023). Functionally graded materials for knee and hip arthroplasty; an update on design, optimization, and manufacturing. *Composite Structures*, 117350. <https://doi.org/10.1016/j.compstruct.2023.117350>
- [6] El-Galy, I. M., Saleh, B. I., & Ahmed, M. H. (2019). Functionally graded materials classifications and development trends from industrial point of view. *SN Applied Sciences*, 1, 1-23. <https://doi.org/10.1007/s42452-019-1413-4>
- [7] Gasik, M. M. (1998). Micromechanical modelling of functionally graded materials. *Computational Materials Science*, 13(1-3), 42-55. [https://doi.org/10.1016/S0927-0256\(98\)00044-5](https://doi.org/10.1016/S0927-0256(98)00044-5)
- [8] Zhang, R., Jiang, F., Xue, L., & Yu, J. (2022). Review of additive manufacturing techniques for large-scale metal functionally graded materials. *Crystals*, 12(6), 858. <https://doi.org/10.3390/cryst12060858>
- [9] Yao, L., Ramesh A., Xiao, Z., Chen, Y., & Zhuang, Q. (2023). Multimetal research in powder bed fusion: a review. *Materials*, 16(12), 4287. <https://doi.org/10.3390/ma16124287>
- [10] Mahmoud, D., & Elbestawi, M. A. (2017). Lattice structures and functionally graded materials applications in additive manufacturing of orthopedic implants: a review. *Journal of Manufacturing and Materials Processing*, 1(2), 13. <https://doi.org/10.3390/jmmp1020013>
- [11] Zhang, C., Chen, F., Huang, Z., Jia, M., Chen, G., Ye, Y., ... & Lavernia, E. J. (2019). Additive manufacturing of functionally graded materials: A review. *Materials Science and Engineering: A*, 764, 138209. <https://doi.org/10.1016/j.msea.2019.138209>
- [12] Wei, C., Sun, Z., Chen, Q., Liu, Z., & Li, L. (2019). Additive manufacturing of horizontal and 3D functionally graded 316L/Cu10Sn components via multiple material selective laser melting. *Journal of Manufacturing Science and Engineering*, 141(8), 081014. <https://doi.org/10.1115/1.4043983>
- [13] Nemat-Alla, M. (2003). Reduction of thermal stresses by developing two-dimensional functionally graded materials. *International journal of solids and structures*, 40(26), 7339-7356. <https://doi.org/10.1016/j.ijsolstr.2003.08.017>
- [14] Sharma, P., & Khinchi, A. (2023). Finite element modeling of two-directional FGM beams under hygrothermal effect. *International Journal on Interactive Design and Manufacturing (IJIDeM)*, 1-8. <https://doi.org/10.1007/s12008-022-01190-8>
- [15] Ghazwani, M. H., Alnujaie, A., Avcar, M., & Van Vinh, P. (2024). Examination of the high-frequency behavior of functionally graded porous nanobeams using nonlocal simple higher-order shear deformation theory. *Acta Mechanica*, 1-20. <https://doi.org/10.1007/s00707-024-03858-6>
- [16] Zhang, J. Z., McAvoy, D. T., Halpern, B. L., Schmitt, J. J., Zanoni, R., & Schaschek, K. (1994). Jet vapor deposition of organic guest-inorganic host thin films for optical and electronic applications. *Journal of electronic materials*, 23, 1239-1244. <https://doi.org/10.1007/BF02649976>
- [17] Wood, M., & Ward-Close, M. (1995). Fibre-reinforced intermetallic compounds by physical vapour deposition. *Materials Science and Engineering: A*, 192, 590-596. [https://doi.org/10.1016/0921-5093\(94\)03282-3](https://doi.org/10.1016/0921-5093(94)03282-3)
- [18] Groves, J. F., & Wadley, H. N. G. (1997). Functionally graded materials synthesis via low vacuum directed vapor deposition. *Composites Part B: Engineering*, 28(1-2), 57-69. [https://doi.org/10.1016/S1359-8368\(96\)00023-6](https://doi.org/10.1016/S1359-8368(96)00023-6)
- [19] Fathi, R., Wei, H., Saleh, B., Radhika, N., Jiang, J., Ma, A., ... & Ostrikov, K. K. (2022). Past and present of functionally

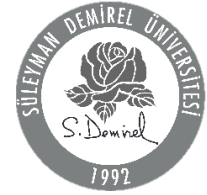
- graded coatings: Advancements and future challenges. *Applied Materials Today*, 26, 101373.. <https://doi.org/10.1016/j.apmt.2022.101373>
- [20] Saeed, M., Alshammari, Y., Majeed, S. A., & Al-Nasrallah, E. (2020). Chemical vapour deposition of graphene—Synthesis, characterisation, and applications: A review. *Molecules*, 25(17), 3856. <https://doi.org/10.3390/molecules25173856>
- [21] Nur-E-Alam, M., Basher, M. K., Vasiliev, M., & Das, N. (2021). Physical vapor-deposited silver (Ag)-based metal-dielectric nanocomposites for thin-film and coating applications. *Applied Sciences*, 11(15), 6746. <https://doi.org/10.3390/app11156746>
- [22] Bhavar, V., Kattire, P., Thakare, S., & Singh, R. K. P. (2017, September). A review on functionally graded materials (FGMs) and their applications. In *IOP conference series: materials science and engineering*, 229(1), 012021. <https://doi.org/10.1088/1757-899X/229/1/012021>
- [23] Grammes, T., Emmerich, T., & Aktaa, J. (2021). W/EUROFER functionally graded coatings for plasma facing components: Technology transfer to industry and upscaling. *Fusion Engineering and Design*, 173, 112940. <https://doi.org/10.1016/j.fusengdes.2021.112940>
- [24] Ramesh, M., Karthik, A., James, D. J. D., & Pandiyan, G. K. (2023). Functionally graded materials: review on manufacturing by liquid and gas based techniques. *Materials Research Express*, 10(8), 085305. <https://doi.org/10.1088/2053-1591/acf1f1>
- [25] Hirai, T., & Sasaki, M. (1991). Vapor-deposited functionally graded materials. *JSME international journal. Ser. 1, Solid mechanics, strength of materials*, 34(2), 123-129. https://doi.org/10.1299/jsmea1988.34.2_123
- [26] Choy, K. L. (2003). Chemical vapour deposition of coatings. *Progress in materials science*, 48(2), 57-170. [https://doi.org/10.1016/S0079-6425\(01\)00009-3](https://doi.org/10.1016/S0079-6425(01)00009-3)
- [27] Wang, X., Chu, X., Zhao, H., Lu, S., Fang, F., Li, J., ... & Wang, X. (2014). Controllable growth of functional gradient ZnO material using chemical vapor deposition. *Integrated Ferroelectrics*, 151(1), 1-6. <https://doi.org/10.1080/10584587.2014.898552>
- [28] Jin, G., Takeuchi, M., Honda, S., Nishikawa, T., & Awaji, H. (2005). Properties of multilayered mullite/Mo functionally graded materials fabricated by powder metallurgy processing. *Materials Chemistry and Physics*, 89(2-3), 238-243. <https://doi.org/10.1016/j.matchemphys.2004.03.031>
- [29] Übeyli, M., Balci, E., Sarikan, B., Öztaş, M. K., Camuşcu, N., Yildirim, R. O., & Keleş, Ö. (2014). The ballistic performance of SiC-AA7075 functionally graded composite produced by powder metallurgy. *Materials & Design*, 56, 31-36. <https://doi.org/10.1016/j.matdes.2013.10.092>
- [30] Erdemir, F., Canakci, A., & Varol, T. (2015). Microstructural characterization and mechanical properties of functionally graded Al2024/SiC composites prepared by powder metallurgy techniques. *Transactions of Nonferrous Metals Society of China*, 25(11), 3569-3577. [https://doi.org/10.1016/S1003-6326\(15\)63996-6](https://doi.org/10.1016/S1003-6326(15)63996-6)
- [31] Tripathy, A., Sarangi, S. K., & Panda, R. (2017). Fabrication of functionally graded composite material using powder metallurgy route: an overview. *Int. J. Mech. Prod. Eng. Res. Dev*, 7(6), 135-145.
- [32] Liang, J., Zhang, G., Zhou, Y., Song, S., Zuo, X., & Wang, H. (2022). The Microstructure and the Properties of 304 and 430 Steel Foams Prepared by Powder Metallurgy Using CaCl₂ as a Space Holder. *Metals*, 12(7), 1182. <https://doi.org/10.3390/met12071182>
- [33] Mishra, S. K., & Pathak, L. C. (2009). Self-propagating high-temperature synthesis (SHS) of advanced high-temperature ceramics. *Key Engineering Materials*, 395, 15-38. <https://doi.org/10.4028/www.scientific.net/KEM.395.15>
- [34] Yong, C., Xunjia, S., Genliang, H., & YaKun, X. (2013, March). Research on self-propagating high temperature synthesis prepared ZrC-ZrB₂ composite ceramic. In *Journal of Physics: Conference Series*, 419(1), 012057. IOP Publishing. <https://doi.org/10.1088/1742-6596/419/1/012057>
- [35] Parihar, R. S., Setti, S. G., & Sahu, R. K. (2018). Recent advances in the manufacturing processes of functionally graded materials: a review. *Science and Engineering of Composite Materials*, 25(2), 309-336. <https://doi.org/10.1155/secm-2015-0395>
- [36] Liechty, B. C., & Webb, B. W. (2008). Flow field characterization of friction stir processing using a particle-grid method. *Journal of Materials Processing Technology*, 208(1-3), 431-443. <https://doi.org/10.1016/j.jmatprotec.2008.01.008>
- [37] Karthikeyan, L., Senthilkumar, V. S., & Padmanabhan, K. A. (2010). On the role of process variables in the friction stir processing of cast aluminum A319 alloy. *Materials & Design*, 31(2), 761-771. <https://doi.org/10.1016/j.matdes.2009.08.001>
- [38] Fu, P. X., Kang, X. H., Ma, Y. C., Liu, K., Li, D. Z., & Li, Y. Y. (2008). Centrifugal casting of TiAl exhaust valves. *Intermetallics*, 16(2), 130-138. <https://doi.org/10.1016/j.intermet.2007.08.007>
- [39] Rajan, T. P. D., Pillai, R. M., & Pai, B. C. (2008). Centrifugal casting of functionally graded aluminium matrix composite components. *International Journal of Cast Metals Research*, 21(1-4), 214-218. <https://doi.org/10.1179/136404608X361972>
- [40] Sobczak, J. J., & Drenchev, L. (2013). Metallic functionally graded materials: a specific class of advanced composites. *Journal of Materials Science & Technology*, 29(4), 297-316. <https://doi.org/10.1016/j.jmst.2013.02.006>
- [41] Singh, S. P., Rohith, R. P., Nirmal, S. F., Raja, D. E., & Ravichandran, P. (2024). Improvement in manufacturing of aluminium-based functionally graded materials through centrifugal casting—A review. *Engineering Proceedings*, 61(1), 16. <https://doi.org/10.3390/engproc2024061016>
- [42] Mercadelli, E., Sanson, A., Pinasco, P., Roncari, E., & Galassi, C. (2010). Tape cast porosity-graded piezoelectric ceramics. *Journal of the European Ceramic Society*, 30(6), 1461-1467. <https://doi.org/10.1016/j.jeurceramsoc.2009.12.004>
- [43] Schafföner, S., & Aneziris, C. G. (2012). Pressure slip casting of coarse grain oxide ceramics. *Ceramics International*, 38(1), 417-422. <https://doi.org/10.1016/j.ceramint.2011.06.064>
- [44] Baskin, D. M., Zimmerman, M. H., Faber, K. T., & Fuller, E. R. (1997). Forming single-phase laminates via the gelcasting technique. *Journal of the American Ceramic Society*, 80(11), 2929-2932. <https://doi.org/10.1111/j.1151-2916.1997.tb03213.x>
- [45] Zimmerman, M. H., Faber, K. T., & Fuller Jr, E. R. (1997). Forming textured microstructures via the gelcasting technique. *Journal of the American Ceramic Society*, 80(10), 2725-2729. <https://doi.org/10.1111/j.1151-2916.1997.tb03184.x>

- [46] Topateş, G., Akça, E., Tür, Y. K., & Duran, C. (2024). Functionally graded Al₂O₃-based ceramic systems by gel casting method. *International Journal of Applied Ceramic Technology*, 22(1), e14898. <https://doi.org/10.1111/ijac.14898>
- [47] Sofie, S. W. (2007). Fabrication of functionally graded and aligned porosity in thin ceramic substrates with the novel freeze-tape-casting process. *Journal of the American Ceramic Society*, 90(7), 2024-2031. <https://doi.org/10.1111/j.1551-2916.2007.01720.x>
- [48] Scanlan, M., Browne, D. J., & Bates, A. (2005). New casting route to novel functionally gradient light alloys. *Materials Science and Engineering: A*, 413, 66-71. <https://doi.org/10.1016/j.msea.2005.09.004>
- [49] Rahvard, M. M., Tamizifar, M., Boutorabi, M. A., & Shiri, S. G. (2014). Effect of superheat and solidified layer on achieving good metallic bond between A390/A356 alloys fabricated by cast-decant-cast process. *Transactions of Nonferrous Metals Society of China*, 24(3), 665-672. [https://doi.org/10.1016/S1003-6326\(14\)63109-5](https://doi.org/10.1016/S1003-6326(14)63109-5)
- [50] Kruth, J. P. (1991). Material increment manufacturing by rapid prototyping techniques. *CIRP annals*, 40(2), 603-614. [https://doi.org/10.1016/S0007-8506\(07\)61136-6](https://doi.org/10.1016/S0007-8506(07)61136-6)
- [51] Bikas, H., Stavropoulos, P., & Chryssolouris, G. (2016). Additive manufacturing methods and modelling approaches: a critical review. *The International Journal of Advanced Manufacturing Technology*, 83, 389-405. <https://doi.org/10.1007/s00170-015-7576-2>
- [52] Guessasma, S., Tao, L., Belhabib, S., Zhu, J., Zhang, W., & Nouri, H. (2018). Analysis of microstructure and mechanical performance of polymeric cellular structures designed using stereolithography. *European Polymer Journal*, 98, 72-82. <https://doi.org/10.1016/j.eurpolymj.2017.10.034>
- [53] Pagac, M., Hajnys, J., Ma, Q. P., Jancar, L., Jansa, J., Stefek, P., & Mesicek, J. (2021). A review of vat photopolymerization technology: materials, applications, challenges, and future trends of 3D printing. *Polymers*, 13(4), 598. <https://doi.org/10.3390/polym13040598>
- [54] Wang, J., & Shaw, L. L. (2006). Fabrication of functionally graded materials via inkjet color printing. *Journal of the American Ceramic Society*, 89(10), 3285-3289. <https://doi.org/10.1111/j.1551-2916.2006.01206.x>
- [55] Chen, Y., Ye, L., Kinloch, A. J., & Zhang, Y. X. (2022). 3D printed carbon-fibre reinforced composite lattice structures with good thermal-dimensional stability. *Compos. Sci. Technol.*, 227, 109599. <https://doi.org/10.1016/j.compscitech.2022.109599>
- [56] Garg, A., Sharma, A., Zheng, W., & Li, L. (2025). A review on artificial intelligence-enabled mechanical analysis of 3D printed and FEM-modelled auxetic metamaterials. *Virtual and Physical Prototyping*, 20(1), e2445712. <https://doi.org/10.1080/17452759.2024.2445712>
- [57] Wang, Y., Müller, W. D., Rumjahn, A., & Schwitalla, A. (2020). Parameters influencing the outcome of additive manufacturing of tiny medical devices based on PEEK. *Materials*, 13(2), 466. <https://doi.org/10.3390/ma13020466>
- [58] Alkunte, S., Fidan, I., Naikwadi, V., Gudavasov, S., Ali, M. A., Mahmudov, M., ... & Cheepu, M. (2024). Advancements and Challenges in Additively Manufactured Functionally Graded Materials: A Comprehensive Review. *Journal of Manufacturing and Materials Processing*, 8(1), 23. <https://doi.org/10.3390/jmmp8010023>
- [59] Sireesha, M., Lee, J., Kiran, A. S. K., Babu, V. J., Kee, B. B., & Ramakrishna, S. (2018). A review on additive manufacturing and its way into the oil and gas industry. *RSC advances*, 8(40), 22460-22468. <https://doi.org/10.1039/C8RA03194K>
- [60] Nian, Y., Wan, S., Avcar, M., Yue, R., & Li, M. (2023). 3D printing functionally graded metamaterial structure: Design, fabrication, reinforcement, optimization. *International Journal of Mechanical Sciences*, 258, 108580. <https://doi.org/10.1016/j.ijmecsci.2023.108580>
- [61] Han, C., Li, Y., Wang, Q., Cai, D., Wei, Q., Yang, L., ... & Shi, Y. (2018). Titanium/hydroxyapatite (Ti/HA) gradient materials with quasi-continuous ratios fabricated by SLM: material interface and fracture toughness. *Materials & Design*, 141, 256-266. <https://doi.org/10.1016/j.matdes.2017.12.037>
- [62] Ansari, P., Rehman, A. U., Pitir, F., Veziroglu, S., Mishra, Y. K., Aktas, O. C., & Salamci, M. U. (2021). Selective laser melting of 316L austenitic stainless steel: Detailed process understanding using multiphysics simulation and experimentation. *Metals*, 11(7), 1076. <https://doi.org/10.3390/met11071076>
- [63] Del Val, J., Arias-González, F., Barro, O., Riveiro, A., Comesaña, R., Penide, J., ... & Pou, J. (2017). Functionally graded 3D structures produced by laser cladding. *Procedia Manufacturing*, 13, 169-176. <https://doi.org/10.1016/j.promfg.2017.09.029>
- [64] Lai, Q., Abrahams, R., Yan, W., Qiu, C., Mutton, P., Paradowska, A., & Soodi, M. (2017). Investigation of a novel functionally graded material for the repair of premium hypereutectoid rails using laser cladding technology. *Composites Part B: Engineering*, 130, 174-191. <https://doi.org/10.1016/j.compositesb.2017.07.089>
- [65] Liu, W., & DuPont, J. N. (2003). Fabrication of functionally graded TiC/Ti composites by laser engineered net shaping. *Scripta Materialia*, 48(9), 1337-1342. [https://doi.org/10.1016/S1359-6462\(03\)00020-4](https://doi.org/10.1016/S1359-6462(03)00020-4)
- [66] Kim, H., Cong, W., Zhang, H. C., & Liu, Z. (2017). Laser engineered net shaping of nickel-based superalloy Inconel 718 powders onto AISI 4140 alloy steel substrates: Interface bond and fracture failure mechanism. *Materials*, 10(4), 341. <https://doi.org/10.3390/ma10040341>
- [67] Rahmani, R., Lopes, S. I., & Prashanth, K. G. (2023). Selective laser melting and spark plasma sintering: a perspective on functional biomaterials. *Journal of Functional Biomaterials*, 14(10), 521. <https://doi.org/10.3390/jfb14100521>
- [68] Tofail, S. A., Koumoulos, E. P., Bandyopadhyay, A., Bose, S., O'Donoghue, L., & Charitidis, C. (2018). Additive manufacturing: scientific and technological challenges, market uptake and opportunities. *Materials today*, 21(1), 22-37. <https://doi.org/10.1016/j.mattod.2017.07.001>
- [69] Pompe, W., Worch, H., Eppe, M., Friess, W., Gelinsky, M., Greil, P., ... & Schulte, K. J. M. S. (2003). Functionally graded materials for biomedical applications. *Materials Science and Engineering: A*, 362(1-2), 40-60. [https://doi.org/10.1016/S0921-5093\(03\)00580-X](https://doi.org/10.1016/S0921-5093(03)00580-X)
- [70] Murr, L. E., Martinez, E., Amato, K. N., Gaytan, S. M., Hernandez, J., Ramirez, D. A., ... & Wicker, R. B. (2012). Fabrication of metal and alloy components by additive manufacturing: examples of 3D materials science. *Journal of Materials Research and Technology*, 1(1), 42-54. [https://doi.org/10.1016/S2238-7854\(12\)70009-1](https://doi.org/10.1016/S2238-7854(12)70009-1)
- [71] Corbin, S. F., Zhao-Jie, X., Henein, H., & Apte, P. S. (1999). Functionally graded metal/ceramic composites by tape casting, lamination and infiltration. *Materials Science and Engineering: A*, 262(1-2), 192-203. [https://doi.org/10.1016/S0921-5093\(98\)01019-3](https://doi.org/10.1016/S0921-5093(98)01019-3)

- [72] Zahedi, A. M., Rezaie, H. R., Javadpour, J., Mazaheri, M., & Haghghi, M. G. (2009). Processing and impact behavior of Al/SiCp composites fabricated by the pressureless melt infiltration method. *Ceramics International*, 35(5), 1919-1926. <https://doi.org/10.1016/j.ceramint.2008.10.024>
- [73] Drevet, R., Fauré, J., & Benhayoune, H. (2024). Electrophoretic Deposition of Bioactive Glass Coatings for Bone Implant Applications: A Review. *Coatings*, 14(9), 1084. <https://doi.org/10.3390/coatings14091084>
- [74] Ghosh, S., Haldar, S., Gupta, S., Chauhan, S., Mago, V., Roy, P., & Lahiri, D. (2022). Single unit functionally graded bioresorbable electrospun scaffold for scar-free full-thickness skin wound healing. *Biomaterials Advances*, 139, 212980. <https://doi.org/10.1016/j.bioadv.2022.212980>
- [75] Li, D., & Xia, Y. (2004). Electrospinning of nanofibers: reinventing the wheel?. *Advanced materials*, 16(14), 1151-1170. <https://doi.org/10.1002/adma.200400719>
- [76] Greiner, A., & Wendorff, J. H. (2007). Electrospinning: a fascinating method for the preparation of ultrathin fibers. *Angewandte Chemie International Edition*, 46(30), 5670-5703. <https://doi.org/10.1002/anie.200604646>
- [77] Qasim, S. B., Najeeb, S., Delaine-Smith, R. M., Rawlinson, A., & Rehman, I. U. (2017). Potential of electrospun chitosan fibers as a surface layer in functionally graded GTR membrane for periodontal regeneration. *Dental Materials*, 33(1), 71-83. <https://doi.org/10.1016/j.dental.2016.10.003>
- [78] Russo, F., Ursino, C., Avruscio, E., Desiderio, G., Perrone, A., Santoro, S., ... & Figoli, A. (2020). Innovative Poly (Vinylidene Fluoride)(PVDF) electrospun nanofiber membrane preparation using DMSO as a low toxicity solvent. *Membranes*, 10(3), 36. <https://doi.org/10.3390/membranes10030036>
- [79] Jayachandran, M., Tsukamoto, H., Sato, H., & Watanabe, Y. (2013). Formation Behavior of Continuous Graded Composition in Ti-ZrO₂ Functionally Graded Materials Fabricated by Mixed-Powder Pouring Method. *Journal of Nanomaterials*, 2013(1), 504631. <https://doi.org/10.1155/2013/504631>
- [80] Pakseresht, A. H., Ghasali, E., Nejati, M., Shirvanimoghaddam, K., Javadi, A. H., & Teimouri, R. (2015). Development empirical-intelligent relationship between plasma spray parameters and coating performance of Yttria-Stabilized Zirconia. *The International Journal of Advanced Manufacturing Technology*, 76, 1031-1045. <https://doi.org/10.1007/s00170-014-6212-x>
- [81] Lim, Y. M., Park, Y. J., Yun, Y. H., & Hwang, K. S. (2002). Functionally graded Ti/HAP coatings on Ti-6Al-4V obtained by chemical solution deposition. *Ceramics International*, 28(1), 37-41. [https://doi.org/10.1016/S0272-8842\(01\)00055-4](https://doi.org/10.1016/S0272-8842(01)00055-4)
- [82] Besra, L., & Liu, M. (2007). A review on fundamentals and applications of electrophoretic deposition (EPD). *Progress in Materials Science*, 52(1), 1-61. <https://doi.org/10.1016/j.pmatsci.2006.07.001>
- [83] Shailesh, P., Sundarajan, S., & Komaraiah, M. (2014). Optimization of process parameters of Al-Si alloy by centrifugal casting technique using Taguchi design of experiments. *Procedia Materials Science*, 6, 812-820. <https://doi.org/10.1016/j.mspro.2014.07.098>
- [84] Arsha, A. G., Jayakumar, E., Rajan, T. P. D., Antony, V., & Pai, B. C. (2015). Design and fabrication of functionally graded in-situ aluminium composites for automotive pistons. *Materials & Design*, 88, 1201-1209. <https://doi.org/10.1016/j.matdes.2015.09.099>
- [85] Wang, F., Jiang, K., & Xu, X. (2009). Gel casting of stainless steel powder through mold DIS process. *Tsinghua Science and Technology*, 14(S1), 216-222. [https://doi.org/10.1016/S1007-0214\(09\)70095-1](https://doi.org/10.1016/S1007-0214(09)70095-1)
- [86] Tallon, C., & Franks, G. V. (2011). Recent trends in shape forming from colloidal processing: A review. *Journal of the Ceramic Society of Japan*, 119(1387), 147-160. <https://doi.org/10.2109/jcersj2.119.147>
- [87] Yeo, J. G., Jung, Y. G., & Choi, S. C. (1998). Design and microstructure of ZrO₂/SUS316 functionally graded materials by tape casting. *Materials Letters*, 37(6), 304-311. [https://doi.org/10.1016/S0167-577X\(98\)00111-6](https://doi.org/10.1016/S0167-577X(98)00111-6)
- [88] Fu, C., Chan, S. H., Liu, Q., Ge, X., & Pasciak, G. (2010). Fabrication and evaluation of Ni-GDC composite anode prepared by aqueous-based tape casting method for low-temperature solid oxide fuel cell. *International Journal of Hydrogen Energy*, 35(1), 301-307. <https://doi.org/10.1016/j.ijhydene.2009.09.101>
- [89] Katayama, T., Sukenaga, S., Saito, N., Kagata, H., & Nakashima, K. (2011, October). Fabrication of Al₂O₃-W functionally graded materials by slipcasting method. In *IOP Conference Series: Materials Science and Engineering*, 18(20), 202023. IOP Publishing. <http://dx.doi.org/10.1088/1757-899X/18/20/202023>
- [90] Bulatova, R., Bahl, C., Andersen, K., Kuhn, L. T., & Pryds, N. (2015). Functionally Graded Ceramics Fabricated with Side-by-Side Tape Casting for Use in Magnetic Refrigeration. *International Journal of Applied Ceramic Technology*, 12(4), 891-898. <https://doi.org/10.1111/ijac.12298>
- [91] Santos, L. N. R. M., Silva, J. R. S., Cartaxo, J. M., Rodrigues, A. M., Neves, G. A., & Menezes, R. R. (2021). Freeze-casting applied to ceramic materials: a short review of the influence of processing parameters. *Ceramica*, 67, 1-13. <https://doi.org/10.1590/0366-69132021673812923>
- [92] Anandavel, B., Mohamed Nazirudeen, S. S., Anburaj, J., & Angelo, P. C. (2015). Development and Characterization of Functionally Gradient Al-Si Alloy Using Cast-Decant-Cast Process. *Transactions of the Indian Institute of Metals*, 68, 137-145. <https://doi.org/10.1007/s12666-015-0527-7>
- [93] Nagarajan, D., & Mohana Sivam, P. (2016). Microstructure and Wear Behavior of a Functionally Gradient Al-Si Alloy Prepared Using the Cast-Decant-Cast (CDC) Process. *Materials Performance and Characterization*, 5(5), 637-647. <https://doi.org/10.1520/MPC20160055>
- [94] Hanaor, D., Michelazzi, M., Veronesi, P., Leonelli, C., Romagnoli, M., & Sorrell, C. (2011). Anodic aqueous electrophoretic deposition of titanium dioxide using carboxylic acids as dispersing agents. *Journal of the European Ceramic Society*, 31(6), 1041-1047. <https://doi.org/10.1016/j.jeurceramsoc.2010.12.017>
- [95] Farnoush, H., Mohandes, J. A., & Çimenoglu, H. (2015). Micro-scratch and corrosion behavior of functionally graded HA-TiO₂ nanostructured composite coatings fabricated by electrophoretic deposition. *Journal of the Mechanical Behavior of Biomedical Materials*, 46, 31-40. <https://doi.org/10.1016/j.jmbbm.2015.02.021>
- [96] F42 Committee. (2016). Terminology for additive manufacturing-general principles-terminology. *ASTM International*.
- [97] Halloran, J. W. (2016). Ceramic stereolithography: additive manufacturing for ceramics by photopolymerization. *Annual Review of Materials Research*, 46(1), 19-40. <https://doi.org/10.1146/annurev-matsci-070115-031841>
- [98] Li, L., Bellehumeur, C. S., & Gu, P. (2001). Composite modeling and analysis of FDM prototypes for design and

- fabrication of functionally graded parts. <http://dx.doi.org/10.26153/tsw/3262>
- [99] Cho, J. R., & Ha, D. (2002). Optimal tailoring of 2D volume-fraction distributions for heat-resisting functionally graded materials using FDM. *Computer Methods in Applied Mechanics and Engineering*, 191(29-30), 3195-3211. [https://doi.org/10.1016/S0045-7825\(02\)00256-6](https://doi.org/10.1016/S0045-7825(02)00256-6)
- [100] Scaffaro, R., Lopresti, F., Maio, A., Sutera, F., & Botta, L. (2017). Development of polymeric functionally graded scaffolds: A brief review. *Journal of Applied Biomaterials & Functional Materials*, 15(2), 107-121. <https://doi.org/10.5301/jabfm.5000332>
- [101] Lowen, J. M., & Leach, J. K. (2020). Functionally graded biomaterials for use as model systems and replacement tissues. *Advanced functional materials*, 30(44), 1909089. <https://doi.org/10.1002/adfm.201909089>
- [102] Hong, C. Q., Zhang, X. H., Li, W. J., Han, J. C., & Meng, S. H. (2008). A novel functionally graded material in the ZrB₂-SiC and ZrO₂ system by spark plasma sintering. *Materials Science and Engineering: A*, 498(1-2), 437-441. <https://doi.org/10.1016/j.msea.2008.08.032>
- [103] Kawasaki, A., & Watanabe, R. (1997). Concept and P/M fabrication of functionally gradient materials. *Ceramics International*, 23(1), 73-83. [https://doi.org/10.1016/0272-8842\(95\)00143-3](https://doi.org/10.1016/0272-8842(95)00143-3)
- [104] Dermeik, B., & Travitzky, N. (2020). Laminated object manufacturing of ceramic-based materials. *Advanced engineering materials*, 22(9), 2000256. <https://doi.org/10.1002/adem.202000256>
- [105] Gan, Y. X., Solomon, D., & Reinbolt, M. (2010). Friction stir processing of particle reinforced composite materials. *Materials*, 3(1), 329-350. <https://doi.org/10.3390/ma3010329>
- [106] Rathee, S., Maheshwari, S., & Siddiquee, A. N. (2018). Issues and strategies in composite fabrication via friction stir processing: a review. *Materials and Manufacturing Processes*, 33(3), 239-261. <https://doi.org/10.1080/10426914.2017.1303162>
- [107] Santhosh, V., Prakash, D. A., Murugan, K., & Babu, N. (2020). Thermo-mechanical analysis of Tailor-made functionally graded materials through Friction stir processing. *Materials today: Proc.*, 33, 4445-4449. <https://doi.org/10.1016/j.matpr.2020.07.687>
- [108] Sam, M., Jojith, R., & Radhika, N. (2021). Progression in manufacturing of functionally graded materials and impact of thermal treatment—A critical review. *Journal of Manufacturing Processes*, 68, 1339-1377. <https://doi.org/10.1016/j.jmapro.2021.06.062>
- [109] Lin, X., Yue, T. M., Yang, H. O., & Huang, W. D. (2005). Laser rapid forming of SS316L/Rene88DT graded material. *Materials Science and Engineering: A*, 391(1-2), 325-336. <https://doi.org/10.1016/j.msea.2004.08.072>
- [110] Andertová, J., Tláškal, R., Maryška, M., & Havrda, J. (2007). Functional gradient alumina ceramic materials—Heat treatment of bodies prepared by slip casting method. *Journal of the European Ceramic Society*, 27(2-3), 1325-1331. <https://doi.org/10.1016/j.jeurceramsoc.2006.04.088>
- [111] Traini, T., Mangano, C., Sammons, R. L., Mangano, F., Macchi, A., & Piattelli, A. (2008). Direct laser metal sintering as a new approach to fabrication of an isoelastic functionally graded material for manufacture of porous titanium dental implants. *Dental Materials*, 24(11), 1525-1533. <https://doi.org/10.1016/j.dental.2008.03.029>
- [112] Mahmoud, E. R. I., Takahashi, M., Shibayanagi, T., & Ikeuchi, K. (2009). Effect of friction stir processing tool probe on fabrication of SiC particle reinforced composite on aluminium surface. *Science and Technology of Welding and Joining*, 14(5), 413-425. <https://doi.org/10.1179/136217109X406974>
- [113] Gandra, J., Miranda, R., Vilaça, P., Velhinho, A., & Teixeira, J. P. (2011). Functionally graded materials produced by friction stir processing. *Journal of Materials Processing Technology*, 211(11), 1659-1668. <https://doi.org/10.1016/j.jmatprotec.2011.04.016>
- [114] Sudarmadji, N., Tan, J. Y., Leong, K. F., Chua, C. K., & Loh, Y. T. (2011). Investigation of the mechanical properties and porosity relationships in selective laser-sintered polyhedral for functionally graded scaffolds. *Acta Biomaterialia*, 7(2), 530-537. <https://doi.org/10.1016/j.actbio.2010.09.024>
- [115] Wang, K., Sun, W., Li, B., Xue, H., & Liu, C. (2011). Microstructures in centrifugal casting of SiC p/AlSi9Mg composites with different mould rotation speeds. *Journal of Wuhan University of Technology-Mater*, 26, 504-509. <https://doi.org/10.1007/s11595-011-0257-6>
- [116] Mahamood, R. M., Akinlabi, E. T., Shukla, M., & Pityana, S. L. (2012). Functionally graded material: an overview.
- [117] CPM, S. A., Varghese, B., & Baby, A. (2014). A review on functionally graded materials. *Int. J. Eng. Sci*, 3, 90-101.
- [118] Rikhtegar, F., & Shabestari, S. G. (2014). Investigation on solidification conditions in functionally Si-gradient Al alloys using simulation and cooling curve analysis methods. *Journal of Thermal Analysis and Calorimetry*, 117, 721-729. <https://doi.org/10.1007/s10973-014-3767-6>
- [119] Bai, H., Chen, Y., Delattre, B., Tomsia, A. P., & Ritchie, R. O. (2015). Bioinspired large-scale aligned porous materials assembled with dual temperature gradients. *Science advances*, 1(11), e1500849. <https://doi.org/10.1126/sciadv.1500849>
- [120] Mahamood, R. M., & Akinlabi, E. T. (2015). Laser metal deposition of functionally graded Ti6Al4V/TiC. *Materials & Design*, 84, 402-410. <https://doi.org/10.1016/j.matdes.2015.06.135>
- [121] Tsukamoto, H. (2015). Microstructure and indentation properties of ZrO₂/Ti functionally graded materials fabricated by spark plasma sintering. *Materials Science and Engineering: A*, 640, 338-349. <https://doi.org/10.1016/j.msea.2015.06.005>
- [122] Nie, T., Xue, L., Ge, M., Ma, H., & Zhang, J. (2016). Fabrication of poly (L-lactic acid) tissue engineering scaffolds with precisely controlled gradient structure. *Materials Letters*, 176, 25-28. <https://doi.org/10.1016/j.matlet.2016.04.078>
- [123] Moravcik, I., Cizek, J., Kovacova, Z., Nejezchlebova, J., Kitzmantel, M., Neubauer, E., ... & Dlouhy, I. (2017). Mechanical and microstructural characterization of powder metallurgy CoCrNi medium entropy alloy. *Materials Science and Engineering: A*, 701, 370-380. <https://doi.org/10.1016/j.msea.2017.06.086>
- [124] Naviroj, M., Voorhees, P. W., & Faber, K. T. (2017). Suspension-and solution-based freeze casting for porous ceramics. *Journal of Materials Research*, 32(17), 3372-3382. <https://doi.org/10.1557/jmr.2017.133>
- [125] Sharma, A., Bandari, V., Ito, K., Kohama, K., Ramji, M., & BV, H. S. (2017). A new process for design and manufacture of tailor-made functionally graded composites through friction stir additive manufacturing. *Journal of Manufacturing Processes*, 26, 122-130. <https://doi.org/10.1016/j.jmapro.2017.02.007>

- [126] Zygmontowicz, J., Wiecińska, P., Miazga, A., Konopka, K., & Kaszuwara, W. (2017). Al₂O₃/Ni functionally graded materials (FGM) obtained by centrifugal-slip casting method. *Journal of Thermal Analysis and Calorimetry*, 130, 123-130. <https://doi.org/10.1007/s10973-017-6232-5>
- [127] Omid, N., Jabbari, A. H., & Sedighi, M. (2018). Mechanical and microstructural properties of titanium/hydroxyapatite functionally graded material fabricated by spark plasma sintering. *Powder Metallurgy*, 61(5), 417-427. <https://doi.org/10.1080/00325899.2018.1535391>
- [128] Owoputi, A. O., Inambao, F. L., & Ebhota, W. S. (2018). A review of functionally graded materials: fabrication processes and applications. *International Journal of Applied Engineering Research*, 13(23), 16141-16151.
- [129] Sarathchandra, D. T., Subbu, S. K., & Venkaiah, N. (2018). Functionally graded materials and processing techniques: An art of review. *Materials today: Proc.*, 5(10), 21328-21334. <https://doi.org/10.1016/j.matpr.2018.06.536>
- [130] Khoo, W., Chung, S. M., Lim, S. C., Low, C. Y., Shapiro, J. M., & Koh, C. T. (2019). Fracture behavior of multilayer fibrous scaffolds featuring microstructural gradients. *Materials & Design*, 184, 108184. <https://doi.org/10.1016/j.matdes.2019.108184>
- [131] Odhiambo, J. G., Li, W., Zhao, Y., & Li, C. (2019). Porosity and its significance in plasma-sprayed coatings. *Coatings*, 9(7), 460. <https://doi.org/10.3390/coatings9070460>
- [132] Saleh, B., Jiang, J., Fathi, R., Al-Hababi, T., Xu, Q., Wang, L., ... & Ma, A. (2020). 30 Years of functionally graded materials: An overview of manufacturing methods, Applications and Future Challenges. *Composites Part B: Engineering*, 201, 108376. <https://doi.org/10.1016/j.compositesb.2020.108376>
- [133] Srinivas, P. N. S., & Balakrishna, B. (2020). Microstructural, mechanical and tribological characterization on the Al based functionally graded material fabricated powder metallurgy. *Materials Research Express*, 7(2), 026513. <https://doi.org/10.1088/2053-1591/ab6f41>
- [134] Xiong, Y. Z., Gao, R. N., Zhang, H., Dong, L. L., Li, J. T., & Li, X. (2020). Rationally designed functionally graded porous Ti6Al4V scaffolds with high strength and toughness built via selective laser melting for load-bearing orthopedic applications. *Journal of the Mechanical Behavior of Biomedical Materials*, 104, 103673. <https://doi.org/10.1016/j.jmbbm.2020.103673>
- [135] Yan, L., Chen, Y., & Liou, F. (2020). Additive manufacturing of functionally graded metallic materials using laser metal deposition. *Additive Manufacturing*, 31, 100901. <https://doi.org/10.1016/j.addma.2019.100901>
- [136] Reichardt, A., Shapiro, A. A., Otis, R., Dillon, R. P., Borgonia, J. P., McEnerney, B. W., ... & Beese, A. M. (2021). Advances in additive manufacturing of metal-based functionally graded materials. *International Materials Reviews*, 66(1), 1-29. <https://doi.org/10.1080/09506608.2019.1709354>
- [137] Singh, D. D., Arjula, S., & Reddy, A. R. (2021). Functionally graded materials manufactured by direct energy deposition: a review. *Materials today: Proc.*, 47, 2450-2456. <https://doi.org/10.1016/j.matpr.2021.04.536>
- [138] Goudarzi, Z. M., Valefi, Z., Zamani, P., & Taghi-Ramezani, S. (2022). Comparative investigation of the effect of composition and porosity gradient on thermo-mechanical properties of functionally graded thick thermal barrier coatings deposited by atmospheric plasma spraying. *Ceramics International*, 48(19), 28800-28814. <https://doi.org/10.1016/j.ceramint.2021.12.307>
- [139] Kashkarov, E. B., Krotkevich, D. G., Mingazova, Y. R., Pushilina, N. S., Syrtanov, M. S., Lider, A. M., & Travitzky, N. (2022). Functionally graded laminated composites fabricated from MAX-phase filled preceramic papers: microstructure, mechanical properties and oxidation resistance. *Journal of the European Ceramic Society*, 42(5), 2062-2072. <https://doi.org/10.1016/j.jeurceramsoc.2022.01.023>
- [140] Pasha, A., & Rajaprakash, B. M. (2022). Functionally graded materials (FGM) fabrication and its potential challenges & applications. *Materials Today: Proceedings*, 52, 413-418. <https://doi.org/10.1016/j.matpr.2021.09.077>



Pyrite effect: correlation between compressive strength and durability properties for concrete samples

Zafer Kurt^{a,*}, İlker Ustabaş^b, Muhammet Emin Aydın^c, Ceren İlknur Ustabaş^d

^aCivil Engineering, Faculty of Engineering and Architecture, Recep Tayyip Erdogan University, Rize, Turkey

^bCivil Engineering, Faculty of Engineering and Architecture, Recep Tayyip Erdogan University, Rize, Turkey

^cCivil Engineering, Faculty of Engineering and Architecture, Recep Tayyip Erdogan University, Rize, Turkey

^dCivil Engineering, Faculty of Engineering and Architecture, Recep Tayyip Erdogan University, Rize, Turkey

Highlights

- In this study, water absorption values of pyrite were obtained.
- Also, the effects of pyrite on compressive strength were investigated.
- With this study, the negative effect of pyrite on mechanical values was determined.

Abstract

Despite the two centuries that have passed, concrete still maintains its place at the top as a building material. Although it has different strength and performance characteristics than when it was first discovered with the developing technology, it can be said that it is still the most studied building material today. For this reason, researchers are investigating various materials that can improve the performance of concrete and at the same time can be recycled as waste. In this study, the effect of substitution of pyrite mineral rocks obtained from copper mines into concrete as fine aggregate on the compressive strength and water absorption values of concrete specimens was investigated. For this purpose; 2.5% and 7.5% by weight of pyrite aggregate was substituted for sand and crushed sand aggregate in the concrete design mix. A total of 9 concrete cube specimens of 100x100x100 mm were produced for 3 series together with the reference specimens and the averages of 3 specimens were used as data after 28 days of curing. The data obtained show that as the pyrite aggregate substitution rate increases, the water absorption rate increases by 0.41%, and the compressive strength decreases by 21.32%.

Information

Received:

31.12.2024

Received in revised:

17.01.2025

Accepted:

22.01.2025

Keywords: Concrete, compressive strength, pyrite, water absorption, sustainability, innovative materials

1. Introduction

Concrete is widely used in roads used for the transportation of pedestrians and vehicles, in the production facilities of enterprises such as food, chemistry, pharmaceuticals that work on industry, in recreation areas where people spend their leisure time, in recreation areas around the buildings used for education and training. Since concrete is a low-cost and durable building material compared to other building materials, its use is constantly increasing [1].

However, concrete is not without its drawbacks. Researchers have sought to address these issues, exploring innovative solutions to enhance the material's performance and sustainability. One of the key challenges is the low tensile strength of concrete, which can lead to cracking and deterioration, particularly in structures subjected to bending or pulling forces. Additionally, the

production of Portland cement, a primary ingredient in concrete, contributes to significant greenhouse gas emissions, underscoring the need for more environmentally friendly alternatives [2].

Conventional concrete has disadvantages such as low tensile strength, poor surface strength and rapid crack development during cracking. The performance of concrete depends on its material composition, internal structure and degradation mechanisms in the service environment. Pavement concretes used for any purpose are subjected to compressive, bending stresses as well as abrasion forces in the environment in which they serve. While the flexural strength of the concrete pavement plays an important role when designing such materials, the design of pavements used on airport runways focuses more on impact strength [3].

*Corresponding author: zafer.kurt@erdogan.edu.tr (Z., Kurt), +90 464-223-6126 # 1233

Concrete pavements on concrete roads with heavy traffic load, shopping malls, vehicle fuel stations, storage and industrial sites deteriorate in short periods of time due to the abrasion and impact forces to which they are exposed. In order to prolong the surface deterioration of concrete pavements exposed to continuous abrasion, concrete surface improvement processes are used in addition to the use of high-strength concrete and fiber concrete applications.

Pyrite, a naturally occurring mineral with a distinct golden-yellow hue, has gained attention as a potential substitute for traditional concrete in construction applications. Composed of iron and sulfur, pyrite exhibits unique properties that make it a promising alternative, particularly in terms of its mechanical and water absorption characteristics [4, 5].

Substituting pyrite for concrete could yield significant gains in terms of circular economy and sustainability. Pyrite is a mineral obtained from mineral deposits and can contribute to concrete in terms of strength and durability by using it in concrete. In addition, since pyrite is a heavy aggregate source, it can be used in the construction of imaging units of hospitals for radiation attenuation effect [6-8].

Research has shown that the integration of pyrite into concrete can significantly enhance its performance. Replacing natural sand with iron tailings, a byproduct of pyrite mining, has been shown to improve the compressive strength, splitting tensile strength, and elastic modulus of the resulting concrete mixture, making it a more durable and reliable building material [9]. Moreover, the use of pyrite-based concrete has been found to have a lower corrosion rate and decreased susceptibility to acid erosion, further enhancing its durability and longevity [9].

The utilization of industrial waste materials like pyrite in concrete production aligns with the growing emphasis on sustainable and eco-friendly construction practices. By incorporating these alternative materials, the construction industry can reduce its reliance on natural resources, minimize waste, and contribute to a more environmentally conscious built environment [10].

Pyrite, a naturally occurring mineral composed of iron and sulfur, has garnered the attention of researchers and engineers in the field of concrete construction due to its potential to influence the mechanical and physical properties of this widely-used building material. There are some studies in the literature for this purpose. The researchers found that the addition of pyrite led to a significant increase in the compressive strength of the concrete, with the optimal replacement rate being around 10% [11]. The other study investigated the use of pyrite as a fine aggregate in concrete, reporting that the inclusion of pyrite improved the density and reduced the

porosity of the concrete, contributing to enhanced durability [12]. Demirci [13] studied heavy concrete with pyrite aggregates with s/w 0.4, 0.5 and 0.6, and concluded that as the s/w ratio increases; modulus of elasticity, compressive strength and absorption coefficients decrease. Salguero et al. [14] produced concretes by substituting some of the fine aggregate with pyrite in order to create a new design by replacing fine aggregate in concrete design and conducted research on concretes. They obtained a compressive strength value of 56.44 MPa in concrete specimens using pyrite and 41.03 MPa in reference specimens without pyrite and stated that pyrite is suitable for use in concrete [14].

The use of pyrite in concrete instead of fine aggregate will add financial value to the pyrite mine by reducing waste costs and contributing to the aggregate sector. In the light of the literature research, there are studies on pyrite substitution in concrete, but it is understood that the scope of these studies is not sufficient to fully elucidate the changes caused by the substitution of pyrite in concrete. For this purpose, this paper presents the results of compressive strength and water absorption values obtained as a result of experimental studies.

2. Material and Methods

CEM I 42.5 R type cement was used for concrete design. The pyrite used was obtained from the copper mine. Waste pyrite rock was crushed to coarse aggregate sizes in a jaw crusher. It was then sieved through a 4 mm sieve and converted into fine aggregate. Table 1 shows the percentages of pyrite passing through the sieve after granulometry analysis. Figure 1 shows the granulometry curves of the aggregates used in the mixture and the mixture.

Table 1. Pyrite aggregate sieved (%) values

| Sieved size (mm) | Sieved material (%) |
|------------------|---------------------|
| 4 | 100 |
| 2 | 76.2 |
| 1 | 47.1 |
| 0.5 | 18.7 |
| 0.25 | 3.2 |
| 0.125 | 0.8 |
| 0.063 | 0.0 |
| Pan | 0.0 |

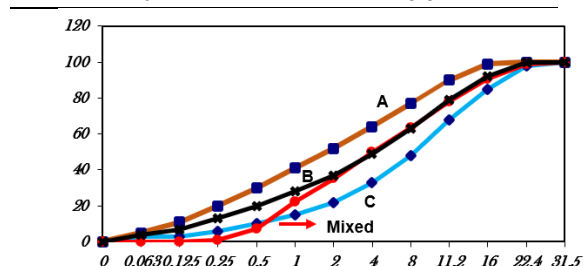


Figure 1. Granulometry curves of aggregates and mixed

The physical properties of aggregates used in concrete design are given in Table 2 [15]. Also, data on the physical

properties and density values of the pyrite mineral are given in Table 3.

Table 2. Physical features of aggregates

| | Natural Sand (0/4) | Crashed Sand (0/4) | Coarse Aggregate1 (4/16) | Coarse Aggregate2 (16/32) | Pyrite Aggregate (0/4) |
|----------------------|--------------------|--------------------|--------------------------|---------------------------|------------------------|
| Specific Weight | 2.31 | 2.48 | 2.62 | 2.69 | 4.74 |
| Water Absorption (%) | 10.6 2 | 4.48 | 1.48 | 1.13 | 0.60 |
| Moisture Content (%) | 9.46 | 2.53 | 0.44 | 0.45 | 0.00 |

Concrete design calculations were made to meet the strength criteria of C40/50 class [17]. The water/cement ratio was 0.45 and the slump was 4 cm. Concrete mixtures were prepared with a pan type mixer. The specimens were filled into 100x100x100 mm molds (Figure 2.) The concrete specimens were subjected to curing in lime-saturated water at room temperature of 20 °C until the 28th day.

Table 3. Pyrite aggregate sieved (%) values

| Explanation | Properties |
|------------------------|---|
| Chemical Composition | FeS ₂ |
| Crystal arrangement | Cubic |
| Crystal Shape | Usually cubic, octahedral, pyritohedral crystalline |
| Hardness | 6-6.5 |
| Specific Gravity | 5-5.028 |
| Color and Transparency | Metallic brass yellow, opaque |
| Line Color | Greenish black |
| Brightness | Metallic |

After the sample cured for 28 days in accordance with TS EN 1097-6 standard, the water absorption amount was removed from the curing pool, the water film around it was wiped with a cloth and the saturated dry surface mass was weighed (W1), these samples were weighed again (W2) after they were kept in a 40 °C oven until they reached constant mass (Figure 3) and the water absorption values of the samples were measured according to Equation 1.

$$Wa = (W1 - W2) / W1 \times 100 \tag{1}$$

In Eq. 1, Wa is the sample water absorption percentage, W1 is the saturated dry surface mass and W2 is the oven dry mass.



Figure 2. Prepared cube samples

The compressive strengths of the 100x100x100 mm cube specimens with 0%, 2.5% and 7.5% pyrite fine aggregate ratios were calculated according to Eq. 2 in accordance with TS EN 12390-2 standard [18] (Figure 4).

$$F_c = P \times a^2 \tag{2}$$

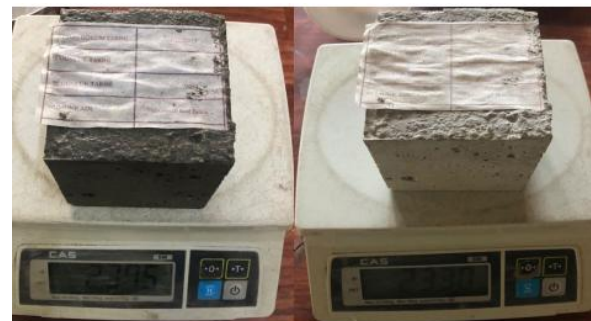


Figure 3. Air-dry weighing and dry-tube weighing

In Eq. 2, F_c is the compressive strength (N/mm²), a is the specimen edge length (100 mm), P is the maximum force at fracture (N).



Figure 4. Compressive strength measurement device

3. Result and Discussion

Water absorption and compressive strength values obtained from 100x100x100 mm concrete specimens with PC0, PC2.5 and PC7.5 pyrite fine aggregate content are shown in Figure 5. PC abbreviates concrete cube samples with pyrite mineral. The compressive strength values given in Figure 5 are the average strength values of 3 specimens measured on the 28th day. The use of 7.5% pyrite aggregate resulted in a 21.33% decrease in the compressive strength and a 21% increase in the water absorption value of the PC7.5 specimens compared to the PC0 specimen.

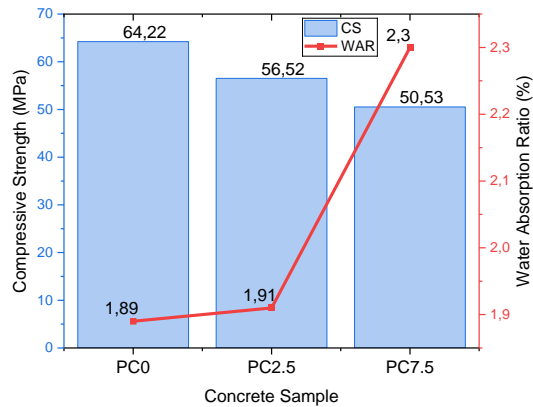


Figure 5. Compressive strength and water absorption values for reference and concrete samples with pyrite

Guo et al. [19] substituted pyrite wastes into concrete and investigated their effect on compressive strength. They showed that the compressive strength increased when the substitution rate was between 0-20%, while the compressive strength decreased between 20-40%.

In their study, Ustabas et al. [6] determined that as the pyrite fineness increased, the specific gravity decreased and the amount of water absorption increased. They observed that pyrite concrete had higher compressive strength than normal concrete at varying water/cement ratios. When the values in this study are compared with the values in the study of Ustabas et al. [6]; it is seen that the use of pyrite contributes positively to the compressive strength, while it has a negative effect on the compressive strength of conventional concrete.

Although direct concrete substitution studies with pyrite are limited, a study by Wang et al. [20] on the use of copper wastes with high sulfur content in cementitious filler pastes showed that compressive strengths generally increased with going up sulfur content, depending on the curing time. However, while the sulfur content of the wastes used was maximum 30.7%, the general sulfur content of pyrite mineral was above 40%. Due to this difference, there may be a difference between the present study and the compressive strengths.

4. Conclusion

In this study, pyrite rock from copper mines was processed into fine aggregate and substituted into concrete cube specimens at 2.5% and 7.5% by weight. In this study, which was carried out to determine the effect of pyrite mineral on the mechanical and physical properties of concrete specimens, the following conclusions can be drawn in the light of the data obtained from the compressive strength and water absorption tests.

i. When pyrite fine aggregate was used in concrete mix, water absorption increased by 0.02% in PB2.5 sample compared to PBO reference sample.

ii. When pyrite fine aggregate was used in concrete mix, compressive strength decreased by 12.00% compared to PBO reference specimen.

iii. While the water absorption value of the PB7.5 sample increased by 0.41%, the compressive strength value decreased by 21.32%.

iv. The use of pyrite decreased the compressive strength of conventional concrete with increasing substitution rate, while increasing the water absorption values of the specimens.

Although there are many parameters for the usability of a mineral in concrete, the results of the tests give us clues that pyrite can be used in concrete. However, the limits of this study include compressive strength and water absorption tests as mechanical and physical tests. In future studies, the study team plans to investigate the physical properties of pyrite specimens such as mass loss and wear length; SEM-EDS analysis for micro mechanical properties; and algae and mossing for durability properties. For upcoming studies, the durability properties of pyrite concrete (fire and acid resistance, etc.) may be interesting topics to investigate.

The sustainability and durability of the building material used against external influences is important in terms of extending the economic life of industrial buildings in terms of both housing for life and the continuation of production. Fires, which are an indirect effect of today's global warming, can have devastating effects both economically and socially. In this context, it is essential to discover innovative materials and minerals that improve the strength and durability properties of building materials against external influences such as acid and fire effects, or to emphasize the importance of those already available, in order to prepare the ground for future studies.

Declaration of Interest Statement

The authors declare that the work described has not been published before; that it is not under consideration for publication anywhere else; that its publication has been approved by all co-authors; that there is no conflict of interest regarding the publication of this article.


References


- [1] Ustabas, I. (2012). The effect of capillarity on chloride transport and the prediction of the accumulation region of chloride in concretes with reinforcement corrosion. *Construction and Building Materials*, 28(1), 640-647. <https://doi.org/10.1016/j.conbuildmat.2011.10.043>
- [2] Al-Shathr, B. S., Eedan, O. A., & Hussain, R. M. (2020). Effects of palm fronds fibers on properties of high-volume fly ash concrete. *In IOP Conference Series: Materials*

- Science and Engineering*, 737(1), 012044. <https://doi.org/10.1088/1757-899X/737/1/012044>
- [3] Fang, M., Chen, Y., Deng, Y., Wang, Z., & Zhu, M. (2023). Toughness improvement mechanism and evaluation of cement concrete for road pavement: A review. *Journal of Road Engineering*, 3(2), 125-140. <https://doi.org/10.1016/j.jreng.2023.01.005>
- [4] Li, G., Zhou, C., Ahmad, W., Usanova, K.I., Karelina, M., Mohamed, A.M., & Khallaf, R. (2022). Fly ash application as supplementary cementitious material: a review. *Materials*, 15(7), 2664. <https://doi.org/10.3390/ma15072664>
- [5] Muda, M. M., Legese, A.M., Urgessa, G., & Boja, T. (2023). Strength, porosity and permeability properties of porous concrete made from recycled concrete aggregates. *Construction Materials*, 3(1), 81. <https://doi.org/10.3390/constrmater3010006>
- [6] Ustabas, I., Demirci, M., Baltas, H., Demir, Y., Erdogdu, S., Kurt, Z., Cakmak, T. (2022). Mechanical and radiation attenuation properties of conventional and heavy concrete with diverse aggregate and water/cement ratios. *Gradevinar*, 74(8), 635-645. <https://doi.org/10.14256/jce.3382.2021>
- [7] Ustabas, I., Erdogdu, S., Akyuz, C., Kurt, Z., & Cakmak, T. (2024). Heavy aggregate and different admixtures effect on pavings: pyrite, corundum and water-retaining polymer. *Revista de la construccion*, 23(1), 31-46. <http://dx.doi.org/10.7764/rdlc.23.1.31>
- [8] Ustabas, I., Erdogdu, S., Uco, M., Kurt, Z., & Cakmak, T. (2024). Heavy aggregate and different admixtures effect on parquets: chrome, magnetite, and quartz-based surface hardener. *Revista de la construccion*, 23(2), 230-245. <http://dx.doi.org/10.7764/rdlc.23.2.230>
- [9] Zheng, W., Wang, S., Quan, X., Qu, Y., Mo, Z., & Lin, C. (2022). Carbonation resistance and pore structure of mixed-fiber-reinforced concrete containing fine aggregates of iron ore tailings. *Materials*, 15(24), 8992. <https://doi.org/10.3390/ma15248992>
- [10] Ustabas, I., & Erdogdu, S. (2016). Performance of mortars incorporating fly ash, silica fume, blast furnace slag at different temperature in magnesium sulfate solution. *Turkish Journal of Materials*, 1(1), 1-14.
- [11] Filho, J.H., Souza, D.J.D., Medeiros, M.H.F., de Pereira, E., & Portella, K.F. (2015). Ataque de matrizes cimenticias por sulfato de sódio:adições minerais como agentes mitigadores. *Cerâmica*, 61(358), 168. <https://doi.org/10.1590/0366-69132015613581905>
- [12] Gil, D. M., & Golewski, G. L. (2018). Potential of siliceous fly ash and silica fume as a substitute for binder in cementitious concretes. In *E3S Web of Conferences*. 49. 30. <https://doi.org/10.1051/e3sconf/20184900030>
- [13] Demirci, M. (2018). Mechanical and mechanical properties of heavy concretes with pyrite, chromium and magnetite aggregates determination of radiation absorption properties. Recep Tayyip Erdogan University, Master Thesis.
- [14] Salguero, F., Grande, J.A., Valente, T., Garrido, R., De la Torre, M. L., Fortes, J. C., & Sánchez, A. (2014). Recycling of manganese gangue materials from waste-dumps in the Iberian Pyrite Belt–Application as filler for concrete production. *Construction and Building Materials*. 54. 363-368. <https://doi.org/10.1016/j.conbuildmat.2013.12.082>
- [15] TS EN 1097-6 (2022). Tests for mechanical and physical properties of aggregates- Part 6: Determination of particle density and water absorption. Turkish Standards Institute. Ankara, 1-5.
- [16] Aydin, M.E. (2023). The effect of pyrite fine aggregate on the surface properties of field concretes. Recep Tayyip Erdogan University. Master Thesis.
- [17] TS 802 (2016). Design Concrete Mixes. Turkish Standards Institute. Ankara.
- [18] TS EN 12390-2 (2002). Testing hardened concrete - Part 2: Making and curing specimens for strength tests. Turkish Standard Institute. Ankara.
- [19] Guo, Z., Feng, Q., Wang, W., Huang, Y., Deng, J., & Xu, Z. (2016). Study on flotation tailings of kaolinite-type pyrite when used as cement admixture and concrete admixture. *Procedia Environmental Sciences*. 31. 644-652. <https://doi.org/10.1016/j.proenv.2016.02.118>
- [20] Wang, S., Wang, Z., Wu, A., Bi, C., Zhang, M., & Liu, W. (2024). Bleeding, flowabilities, rheology, mechanical properties and strength deterioration mechanism of sulphide-rich cemented paste backfill. *Construction and Building Materials*, 421, 135690. <https://doi.org/10.1016/j.conbuildmat.2024.135690>

Influence of corner radius on the axial compressive behavior of FRP-confined rectangular reinforced concrete columns

Ali Juma Noorzad ^{a,*} , Hakan Dilmaç ^b 

^aGraduate School of Natural and Applied Sciences, Suleyman Demirel University, Isparta, Turkey 

^bDepartment of Civil Engineering, Engineering and Natural Sciences Faculty, Suleyman Demirel University, Isparta, Turkey 

Highlights

- Corner radius significantly affects FRP confinement efficiency.
- Larger corner radii enhance strength and ductility in RC columns.
- Stress concentration at sharp corners lowers confinement efficiency.
- Higher aspect ratios reduce the impact of corner radius on strength.
- FRP confinement is most effective in square sections with rounded edges.
- Sharp corners limit FRP confinement effectiveness

Abstract

The corner radius significantly influences the axial compressive behavior of rectangular reinforced concrete columns externally confined with FRP jackets along their lengths. Fiber reinforced polymer sheets are among the most efficient techniques for enhancing both the strength and ductility of reinforced concrete columns; however, their effectiveness depends on the geometry and edge sharpness. Sharp corners increase stress concentrations and reduce the effective confinement area. This paper analytically investigates the structural behavior of rectangular columns confined with fiber reinforced polymer jackets that experience non-uniform stress distributions at the corners under axial compression. A series of rectangular reinforced concrete columns with varying corner radii were analyzed using reliable analytical models to evaluate the effects on the effective confinement factor, stress-strain response, and axial load capacity. The results reveal that edge sharpness significantly affects the axial compressive behavior of confined rectangular columns. Sections with smaller corner radii behave similarly to unconfined columns and exhibit limited effectiveness from fiber reinforced polymer confinement. Finally, the study concludes that the corner radius is directly proportional to the enhancement of strength and ductility in confined rectangular reinforced concrete columns, playing a critical role in their axial load-carrying capacity.

Keywords: Corner radius; CFRP sheets; RC columns; strength; ductility; confinement; axial behavior

Information

Received: 10.01.2025
 Received in revised: 28.01.2025
 Accepted: 28.01.2025

1. Introduction

Reinforced concrete (RC) columns are the most critical components in structural engineering, as they support axial compression loads, with or without flexural moments. However, these columns often experience deterioration due to various factors, such as seismic events, aging, environmental influences, and increasing loading demands, necessitating effective retrofitting and strengthening methods. The application of fiber-reinforced polymer (FRP) confinement has emerged as an effective technique for enhancing both the load-carrying capacity and ductility of existing RC columns over the past three decades [1–3]. The effectiveness of FRP sheets varies depending on the geometry of the columns. FRP is

more effective for circular sections, where uniform stress distribution along the section enhances performance [4]. For rectangular columns, the effectiveness depends on parameters such as the aspect ratio and corner radius. The corner radius plays a crucial role in the confinement mechanism, as sharp corners in rectangular or square cross-sections result in stress concentrations, reducing the efficiency of FRP confinement in improving the structural behavior of columns. Additionally, the maximum confinement stress in rectangular sections typically occurs at the corners [5, 6].

*Corresponding author: alijumanoorzad@gmail.com (A. J., Noorzad), +905543433490

Several experimental and analytical studies have evaluated the influence of corner radius on the structural behavior of fully CFRP-wrapped rectangular and square RC columns under pure axial compressive loads. Wang and Wu [6] conducted a series of experimental tests on 108 CFRP-wrapped square short RC columns. Their experiments, which involved various corner radii, revealed that the corner radius is directly proportional to the increase in axial compressive capacity. They found that sharp corners have little effect on the enhancement of column strength but significantly contribute to an increase in ductility. Al-Salloum [7] studied the influence of edge sharpness on the compressive behavior of square concrete columns retrofitted with FRP, both experimentally and analytically. Based on his findings, the flattening of the edges of square cross-sections plays a crucial role in delaying the failure of the composite. Furthermore, the effectiveness of FRP has a direct relationship with the corner radius.

Jiang et al.[5] introduced a new methodology to analyze the influence of FRP sheet confinement in square RC columns. They conducted numerous experimental tests and presented a new perspective on the efficiency of FRP jackets. Wei and Wu [8] evaluated the effect of cross-sectional aspect ratio on the structural behavior of rectangular RC columns strengthened with FRP jackets. Based on their experimental results, they found that the confinement ratio of sections decreases as the aspect ratio increases. Additionally, they proposed a new stress-strain model for rectangular RC columns fully confined with FRP. Shayanfar and Barros [9] conducted research on a design-oriented model for circular and non-circular FRP RC columns. They proposed a new design-oriented stress-strain model that is applicable to both circular and rectangular RC columns. Lam and Teng proposed a simple design-oriented stress-strain model for RC columns with rectangular cross-sections wrapped externally with FRP. This model predicts the compressive behavior of columns under pure axial load.

The objective of this study is to evaluate the effect of edge sharpness on the axial behavior of rectangular sections externally confined by CFRP sheets using analytical methods. While most research has focused on circular columns, and many experimental studies have been conducted on rectangular columns, limited attention has been given to the analytical assessment of corner radius effects. This gap in the existing literature underscores the

need for a comprehensive analytical investigation into how edge sharpness influences the load-carrying capacity and ductility of CFRP-confined RC columns. This paper seeks to address this gap by providing a more detailed analysis of the efficiency of edge sharpness in enhancing FRP confinement for rectangular columns.

2. Material Properties

FRP composite RC columns consist of three primary materials: plain cement concrete, reinforcing steel, and FRP jackets, each with distinct mechanical properties. Concrete is a complex material known for its high compressive strength but low tensile strength, making compressive strength a critical parameter for structural engineers. Under pure axial loads, concrete exhibits elastic-plastic behavior, and its elastic modulus varies depending on factors such as compressive strength, aggregate properties, and age.

Hognestad [10] proposed a parabolic model to describe the stress-strain behavior of unconfined concrete under pure axial compression, as presented in Table 1. In this study, the unconfined concrete has a compressive strength of 25 MPa, and its mechanical behavior under pure axial compression is illustrated in Figure 1a. Steel reinforcement, commonly known as rebar, is used to provide sufficient tensile strength in combination with concrete in RC columns. The high tensile strength of steel compensates for the tensile weakness of concrete, enhancing both the strength and ductility of reinforced concrete columns. In this paper, Grade 60 mild steel with specified structural properties is used, and its mechanical behavior under pure tensile stress is depicted in Figure 1c. FRP is a composite material characterized by high tensile strength, lightweight properties, and excellent durability, created by combining carbon fibers with a polymer matrix [1]. It is widely employed in retrofitting RC columns due to its advantageous mechanical properties. When applied to RC columns, FRP enhances confinement, thereby improving the load-bearing capacity and ductility of the columns. In this study, the FRP sheets have an ultimate tensile strain of 1.6% and an elastic modulus of 220 GPa. The tensile mechanical properties of the FRP are shown in Figure 1d. The relationships between stress and strain for concrete, steel bars, and FRP composites are detailed in Table 1 according to various analytical models, illustrating their structural behavior under axial loads.

Table 1. Properties of cross-sections and materials

| Concrete | | | Longitudinal steel | | | | FRP sheets | | | Cross-sections | | | |
|-------------------|----------------|---------------------------|--------------------|---------------|----------------|-----------------|-------------------|---------------------------|-------------------|----------------|-------------------------|---------|---------|
| F_{co} (Mpa) | E_c (Mpa) | \mathcal{E}_{co} (%) | cc (mm) | d_b (mm) | f_y (Mpa) | E_s (Mpa) | E_f (Mpa) | \mathcal{E}_{fu} (%) | n_{xtr} (mm) | ψ_f | $b \times h$ (mmxmm) | | |
| 25 | 23500 | 0.2 | 25 | 16 | 420 | 2×10^5 | 2.2×10^5 | 1.6 | 3×0.135 | 0.95 | 300x300 | 300x450 | 300x600 |

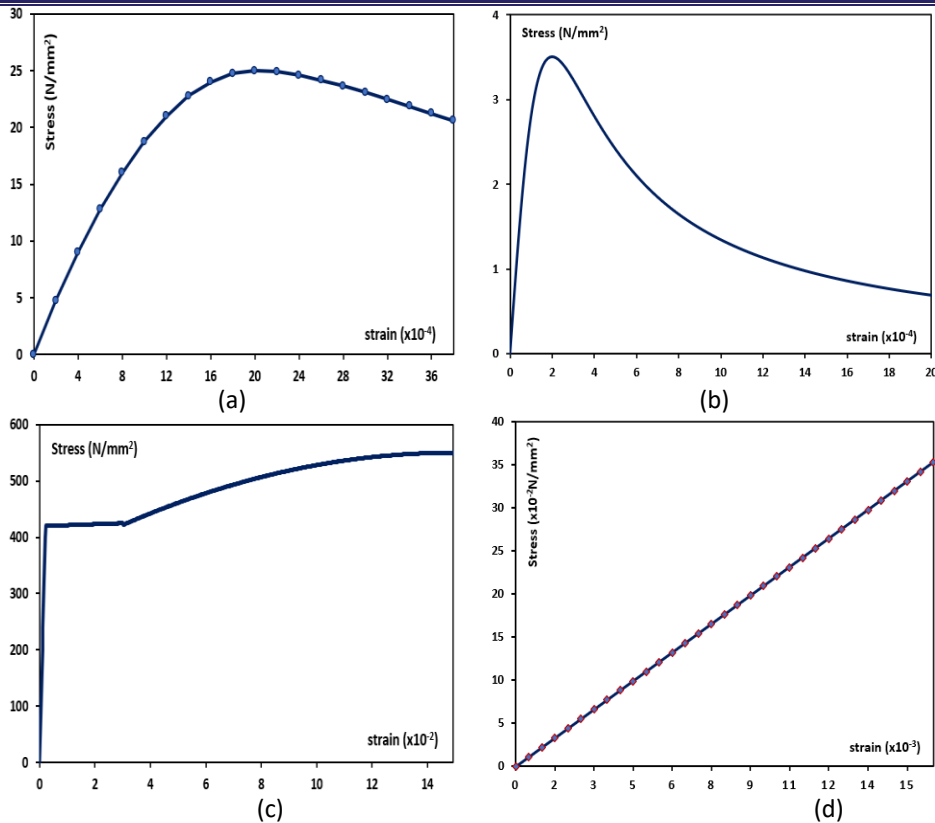


Figure 1. Stress-strain curves: (a) unconfined concrete under compression, (b) unconfined concrete under tension, (c) steel reinforcement under tension, (d) CFRP sheets under tension

3. Methodology

This study investigates the influence of corner radius on the behavior of rectangular cross-section RC columns externally confined with FRP jackets under uniaxial compression using an analytical approach. All column cross-sections are fully wrapped with FRP consisting of three plies, each with a single-layer thickness of 0.135 mm and a tensile elastic modulus of 220 GPa. The mechanical properties of the materials are assumed constants for all cross-sections: the unconfined compressive strength of concrete is 25 MPa, and the yield tensile strength of the longitudinal reinforcement bars is 420 MPa. Based on a review of the literature, several reliable and well-established analytical models for predicting the axial compression behavior of FRP-confined rectangular RC columns are selected to examine key parameters, including the cross-section aspect ratio, corner radius (edge sharpness), material properties, and FRP ply thickness, and their effects on the strength and ductility of the columns.

The relationship between the corner radius ratio and the shape factor, which represents the effective confinement area, was extensively evaluated and

illustrated using graphical representations. For more comprehensive results, three rectangular RC columns with dimensions of 300 × 300 mm, 300 × 450 mm, and 300 × 600 mm—corresponding to aspect ratios of 1, 1.5, and 2, respectively— as shown in Figure 2 were analyzed with varying corner radii of 0, 30, 60, 90, 120, and 150 mm. Additionally, stress-strain curves for all cross-sections with the three aspect ratios were plotted and compared across different corner radii using analytical models. The mechanical properties of materials, including the compressive strength, elastic modulus, and strain corresponding to the peak strength of unconfined concrete; the elastic modulus, tensile yield strength, and diameter of longitudinal steel reinforcement; and the elastic modulus, ultimate strain, and single-layer thickness of the FRP jacket, along with the cross-sectional dimensions, are summarized in Table 1.

Table 2. Summary of stress-strain relationships for concrete, steel reinforcement, and FRP sheets

| Model | Stress-strain relationships | Model parameters |
|--|--|--|
| Concrete in Compression Hognestad Model [10] | Ascending branch: $f_c = f_{co} \left[\frac{2\varepsilon_c}{\varepsilon_{co}} - \left(\frac{\varepsilon_c}{\varepsilon_{co}} \right)^2 \right]$ | $\varepsilon_{co} = \frac{2f_{co}}{E_c}$ $E_c = 4700\sqrt{f_{co}} \text{ (Mpa)}$ |
| | Descending branch: $f_c = 2f_{co} \left[\frac{\varepsilon_c / \varepsilon_{co}}{1 + (\varepsilon_c / \varepsilon_{co})^2} \right]$ | |
| Concrete in Tension: Carreira and Chu 1986 [11] | $\frac{f_t}{f_{to}} = \frac{\beta \frac{\varepsilon_t}{\varepsilon_{to}}}{\beta - 1 + \left(\frac{\varepsilon_t}{\varepsilon_{to}} \right)^\beta}$ | $f_{to} = 0.7\sqrt{f_{co}} \text{ (Mpa)}$ $\beta = \left(\frac{f_{co}}{32.4} \right)^3 + 1.55$ $\varepsilon_{to} = \varepsilon_{co} / 10$ |
| Steel in Tension [12] | $f_s = E_s \varepsilon_s$ for $\varepsilon_s \leq \varepsilon_y$ | $\varepsilon_y = \frac{f_y}{E_s}$ $E_s = 2 \times 10^5 \text{ Mpa}$ |
| | $f_s = f_y + (\varepsilon_s - \varepsilon_y) \left(\frac{f_{sh} - f_y}{\varepsilon_{sh} - \varepsilon_y} \right)$ for $\varepsilon_y < \varepsilon_s \leq \varepsilon_{sh}$ | |
| | $f_s = f_y + (f_u - f_y) \left[2 \left(\frac{\varepsilon_s - \varepsilon_{sh}}{\varepsilon_u - \varepsilon_{sh}} \right) - \left(\frac{\varepsilon_s - \varepsilon_{sh}}{\varepsilon_u - \varepsilon_{sh}} \right)^2 \right]$ for $\varepsilon_{sh} < \varepsilon_s \leq \varepsilon_u$ | |
| FRP in Tension [1] | $f_f = E_f \varepsilon_f$ $\varepsilon_f \leq \varepsilon_{fu}$ | - |

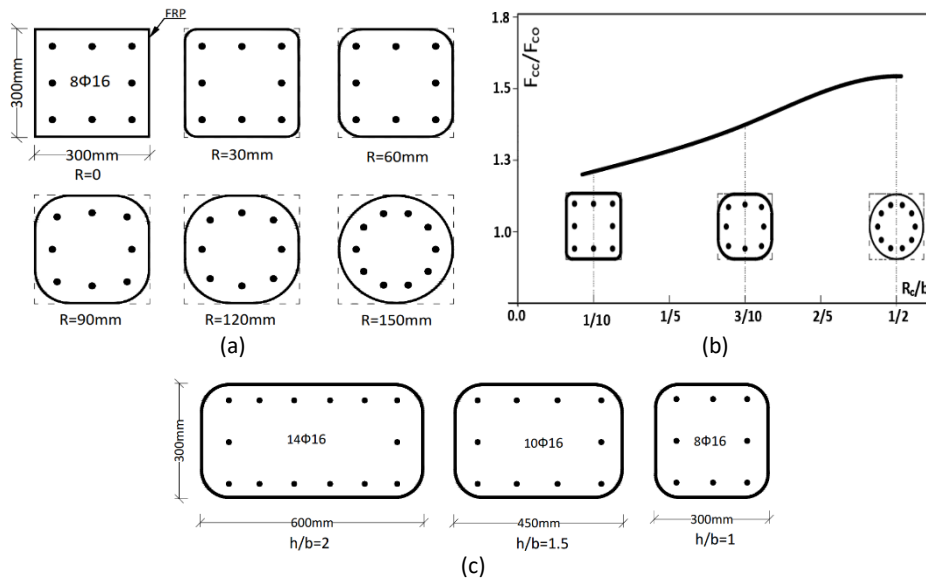


Figure 2. a) Square confined RC columns with various corner radius, b) relationship between normalized strength with corner radius ratios, c) rectangular FRP wraps RC columns with various aspect ratio

3.1. Proposed models for stress-strain prediction

3.1.1 ACI 440.2R-08 confinement model

For rectangular reinforced concrete columns externally confined solely with FRP, a predictive model was proposed by Lam and Teng [13]. This model has been

adopted by the ACI Committee [2] for FRP-confined concrete, as illustrated in Figure 3, and can be computed using the following expressions:

$$\sigma_c = \begin{cases} E_c \varepsilon_c - \frac{(E_c - E_2)^2}{4f_{co}} \varepsilon_c^2 \Rightarrow 0 \leq \varepsilon_c \leq \varepsilon_t \\ f_{co} + E_2 \varepsilon_c \Rightarrow \varepsilon_t < \varepsilon_c \leq \varepsilon_{ccu} \end{cases} \quad (1)$$

$$\frac{\sigma_{cc}}{\sigma_{co}} = 1 + 3.3\psi_f \times k_a \times \frac{\sigma_l}{\sigma_{co}} \quad (2)$$

$$f_l = \frac{2nE_f t_f \sigma_{fu}}{\sqrt{b^2 + h^2}} \quad (3)$$

Where, σ_c and ε_c represent the compressive stress and strain of concrete, respectively, while E_c and E_2 denote the slopes of the first and second branches of the stress-strain curve, σ_{co} refers to the unconfined compressive strength of concrete in a cylindrical test ψ_f is an additional reduction factor, set to 0.95. Furthermore, σ_{fu} and E_f represent the ultimate tensile strength and elastic modulus of the FRP, respectively, and b/h describes the aspect ratio of the rectangular cross-section.

The stress-strain relationship proposed by Lam and Teng [13] is illustrated in Figure 3. This curve consists of two different mathematical functions: parabolic and linear. It is applicable to RC columns confined solely with external FRP sheets and does not account for the effects of stirrups or hoops.

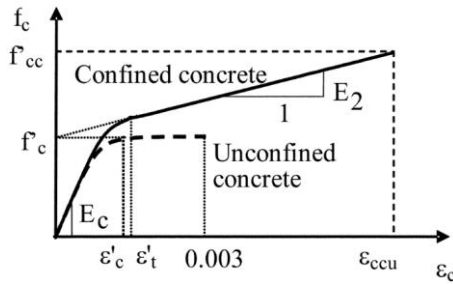


Figure 3. Lam and Teng [13] model for FRP-confined columns

According to the recommendations of the ACI code, the ultimate tensile stress of FRP jackets is calculated using the following expression.

$$\sigma_{fu} = E_f \varepsilon_{fe} = E_f k_\varepsilon \varepsilon_{fu} \quad (4)$$

Here, ε_{fu} represents the rupture strain of FRP wraps, while k_ε denotes the FRP strain efficiency coefficient, with a value for $k_\varepsilon = 0.586$ as recommended by Lam and Teng [13]. Additionally, k_a and k_b are the shape efficiency factors, whose values depend on the effective confinement area and the aspect ratio. For circular cross-sections, k_a equals 1, while for rectangular shapes, it can be determined using the following equation.

$$k_a = \frac{A_e}{A_c} \left(\frac{b}{h} \right)^2 \quad (5)$$

$$k_b = \frac{A_e}{A_c} \left(\frac{h}{b} \right)^{0.5} \quad (6)$$

Where A_e/A_c represents the effective confinement area ratio, which is directly related to the corner radius. The

effective confinement area for an FRP-confined rectangular cross-section is shown in Figure 4. This ratio increases with a larger corner radius and is expressed as follows [2]:

$$\frac{A_e}{A_c} = \frac{1 - \left[\left(\frac{b}{h} \right) (h - 2r_c)^2 + \left(\frac{h}{b} \right) (b - 2r_c)^2 \right] - \rho_g}{3A_g - \rho_g} \quad (7)$$

The maximum compressive strain in FRP-confined concrete, ε_{ccu} , which represents the ductility of the column, can be determined using the following expression [2].

$$\varepsilon_{ccu} = \varepsilon_{co} \left(1.5 + 12k_b \frac{f_l}{f_{co}} \left(\frac{\varepsilon_{fe}}{\varepsilon_{co}} \right)^{0.45} \right) \leq 0.01 \quad (8)$$

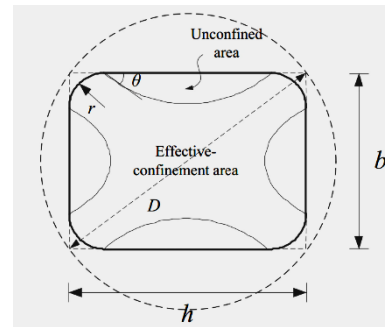


Figure 4. Effective area of confined rectangular column (Lam and Teng [13])

Here, A_e denotes the effective confinement area of the section, A_c represents the total cross-sectional area of the concrete, and A_g is the gross cross-sectional area of the column with rounded corners which is obtained as follows. Additionally, R_c is the corner radius, and ρ_g refers to the longitudinal steel percentage of the column.

$$A_g = bh - (4 - \pi)R_c^2 \quad (9)$$

The maximum theoretical axial load capacity (P_n) of an axially loaded RC column fully confined with FRP wraps along its entire length can be determined using the guidelines provided in ACI-440.2R-08 [2], as follows:

$$P_n = \alpha \left[0.85f_{cc} (A_g - A_{st}) + A_{st}f_y \right] \quad (10)$$

Where α is the accidental eccentricity reduction factor, with $\alpha=0.8$ for tied columns and $\alpha=0.85$ for spiral columns; A_{st} represents the total area of longitudinal steel, and f_y denotes the yield tensile strength of the reinforcing steel.

3.1.2 Wei and Wu model

The two-branch unified simple confinement model proposed by Wei and Wu [8] consists of a parabolic curve in the first segment and a straight line in the second segment. This model is applicable to confined FRP RC columns with circular, rectangular, and square cross-sections. In the first segment of the curve, the initial slope corresponds to the elastic modulus of unconfined concrete E_c , while the slope at the transition point remains consistent across both segments. The model can be expressed in the following general form:

$$f_c = \begin{cases} E_c \varepsilon_c + \frac{f_o - E_c \varepsilon_o}{\varepsilon_o^2} \varepsilon_c^2 \rightarrow 0 \leq \varepsilon_c \leq \varepsilon_o \\ f_o + E_2 (\varepsilon_c - \varepsilon_o) \rightarrow \varepsilon_o \leq \varepsilon_c \leq \varepsilon_{cu} \end{cases} \quad (11)$$

$$E_2 = \frac{f_{cu} - f_o}{\varepsilon_{cu} - \varepsilon_o} \quad (12)$$

The transitional stress f_o and strain ε_o values can be determined using the following equations:

$$f_o = f_{co} + 0.43 \left(\frac{2r}{b}\right)^{0.68} \left(\frac{h}{b}\right)^{-1} f_l \quad (13)$$

$$\varepsilon_o = \frac{(f_o + f_{cu} + E_c \varepsilon_{cu}) - \sqrt{(f_o + f_{cu} + E_c \varepsilon_{cu})^2 - 8f_o E_c \varepsilon_{cu}}}{2E_c} \quad (14)$$

The lateral confining pressure F_L is determined using the following expression:

$$f_l = \frac{2f_{frp}t}{b} = \frac{2E_f \varepsilon_{fu} t}{b} \quad (15)$$

The maximum confined compressive stress and strain of FRP-wrapped RC columns are calculated using the following equations:

$$\frac{f_{cu}}{f_{co}} = 0.5 + 2.7 \left(\frac{2r}{b}\right)^{0.4} \left(\frac{f_l}{f_{co}}\right)^{0.73} \left(\frac{h}{b}\right)^{-1} \quad (16)$$

$$\frac{\varepsilon_{cu}}{\varepsilon_{co}} = 1.7 + 12 \left(\frac{f_l}{f_{co}}\right)^{0.75} \left(\frac{f_{30}}{f_{co}}\right)^{0.62} \left(\frac{0.72r}{b} + 0.64\right)^{-1} \left(\frac{h}{b}\right)^{-0.3} \quad (17)$$

$$\varepsilon_{co} = 0.0009374 \sqrt[4]{f_{co}} (Mpa) \quad (18)$$

Where f_{cu} and ε_{cu} represent the ultimate confined compressive strength of concrete and its corresponding

strain, respectively; f_l denotes the lateral confining pressure; f_{30} refers to the peak compressive strength of concrete with a value of 30 MPa; b and h are the smaller and larger dimensions of the cross-section, respectively; f_{co} and ε_{co} indicate the peak strength and strain of unconfined concrete, respectively; and E_c and E_2 are the slopes of the first and second branches of the stress-strain curve, respectively.

3.1.3 Wu et al. model

They propose a two-part stress-strain relationship for RC columns confined with FRP sheets that is suitable for rectangular cross section. The first branch follows the parabolic law, and its slope is same as well as elastic modulus of unconfined concrete and the second portion of stress-strain curve is linear, and model is given by the following expressions [14]:

$$f_l = \frac{1}{2} \rho_f f_f \quad (19)$$

$$\rho_f = \frac{2(b+h)t_f}{bh} \quad (20)$$

$$f_t = f_{co} (1 + 0.0008 \alpha k_1 \lambda_1) \quad (21)$$

$$\varepsilon_t = \varepsilon_{co} (1 + 0.0034 \alpha k_2 \lambda_1) \quad (22)$$

where, F_t and ε_t represent the transitional stress and the corresponding strain, respectively; F_{cu} and ε_{cu} denote the ultimate confined stress and strain of the concrete, respectively; and ρ_f is the volumetric ratio of FRP sheets to the concrete cross-section.

4. Analytical Study

4.1. Effect of corner Radius

Numerous experimental and analytical studies have investigated the structural compression behavior of rectangular RC columns retrofitted externally with FRP jackets, focusing on the factors influencing confinement effectiveness [5–7, 15]. One crucial parameter is the corner radius, which directly affects the axial compressive behavior of confined columns. This parameter plays a significant role in the distribution and concentration of lateral confining stresses at the corners, the shape factor, and the peak confined compressive strength and strain of the concrete.

Table 3. Shape factor and peak confined strength

| Model | Shape factor | Ultimate stress |
|----------------------------|--|---|
| Al-Salloum and Youssef [7] | $k_a = 1 - \frac{2}{3} \left[\frac{\left(1 - \frac{2r}{b}\right)^2}{1 - (4 - \pi)\left(\frac{r}{b}\right)^2} \right]$ | $\frac{f_{cc}}{f_{co}} = 1 + 3.14k_a \frac{b}{D} \left(\frac{f_l}{f_{co}} \right)$ |
| Lam and Teng [13] | $k_a = \frac{1 - \left[\left(\frac{b}{h}\right)(h - 2r_c)^2 + \left(\frac{h}{b}\right)(b - 2r_c)^2 \right]}{3A_g} - \rho_g \left(\frac{b}{h}\right)^2}{1 - \rho_g}$ | $\frac{f_{cc}}{f_{co}} = 1 + 3.3k_a \left(\frac{f_l}{f_{co}} \right)$ |
| Youssef et al. [18] | $k_a = 1 - \frac{(b - 2r_c)^2 + (h - 2r_c)^2}{3bh(1 - \rho_g)}$ | $\frac{f_{cc}}{f_{co}} = 0.5 + 1.225 \left(\frac{k_a f_l}{f_{co}} \right)^{3/5}$ |
| Saleem and Pimanmas [19] | $k_a = 1 - A_1 - A_2$ $A_1 = \frac{(b - 2r_c)^2 + (h - 2r_c)^2}{3bh}$ $A_2 = \frac{4r_c^2 - \pi r_c^2}{bh}$ | $\frac{f_{cc}}{f_{co}} = 0.56 + 3.3 \left(\frac{f_l}{f_{co}} \right)$ |
| CNR DT 2004 [20] | $k_a = 1 - \frac{(b - 2r_c)^2 + (h - 2r_c)^2}{3bh}$ | $\frac{f_{cc}}{f_{co}} = 1 + 2.6 \left(\frac{f_l}{f_{co}} \right)^{2/3}$ |
| FIB 2019 [21] | $k_a = 1 - \frac{(b - 2r_c)^2 + (h - 2r_c)^2}{3bh}$ | $\frac{f_{cc}}{f_{co}} = 1 + 3.3 \frac{f_l}{f_{co}}$ |

A confined rectangular RC column cross-section with fully wrapped FRP is presented in Figure 5a. This figure illustrates the confinement effectiveness of FRP-wrapped rectangular RC columns, highlighting the influence of the rounded corner radius. The external FRP sheets are depicted by the thin black outline around the cross-section.

The central region, shown in white, is the most effectively confined area, experiencing the full benefits of FRP jacket confinement. This region undergoes uniform stress variation due to lateral confining pressures. In contrast, the hatched areas near the rounded corners represent unconfined zones, where confinement effectiveness is reduced because of the rectangular geometry, especially when the corner radius is small or sharp. A larger corner

radius enhances confinement efficiency by increasing the effective confinement area, distributing lateral stresses more evenly, and reducing stress concentrations along the sides [16].

The confinement efficiency of rectangular columns wrapped with FRP depends significantly on the corner radius and the aspect ratio. Circular cross-sections, which can be viewed as a special case of rectangular sections with large corner radii, offer uniform confinement since the entire concrete area benefits from the FRP wraps. In comparison, rectangular sections demonstrate lower confinement effectiveness, particularly at corners with small radii. Increasing the corner radius substantially improves the confinement of rectangular cross-sections [17].

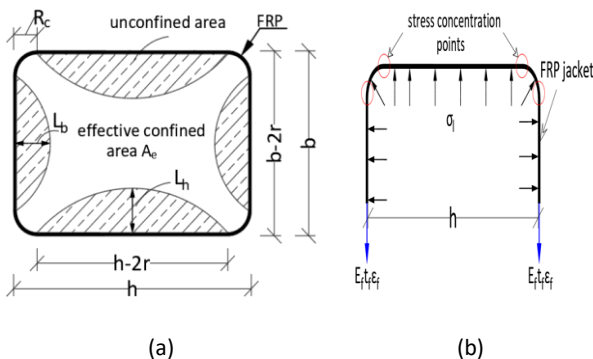


Figure 5. Rectangular cross-sections: a) Area of confined and unconfined concrete, b) distribution of lateral pressures.

The distribution of lateral confining pressure σ_l exerted by FRP sheets on a rectangular FRP-wrapped RC column, along with the locations of stress concentration points, is

illustrated in Figure 5b. The FRP jackets provide lateral confinement to the concrete, enhancing its peak compressive strength and ductility. Stress concentration points, indicated by red circles, experience higher stress levels due to the sharp curvature of the FRP, which can lead to premature failure of the FRP wraps. Lateral confining pressure, represented by black arrows pointing inward, is most significant near the rounded corners. This pressure is generated by hoop stresses within the FRP sheets, which resist the lateral expansion of the concrete under axial compressive loading [16].

The shape factor K_a is defined as the ratio of the effective confined area A_e to the total concrete area A_c for rectangular FRP-wrapped RC columns. It depends on the cross-sectional dimensions, aspect ratio, rounded corner radius, and the percentage of longitudinal steel

reinforcement [2, 9, 15]. The expressions used to calculate the shape factor and peak confined strength, as proposed by various analytical models, are presented in Table 3.

4.2. Impact of aspect ratio

Various column cross-sections, including rectangular, square, and circular configurations, are illustrated in Figure 6. The confinement efficiency of FRP wraps is evaluated for each section type based on corner radius and aspect ratio. Rectangular cross-sections, the most used in RC structural columns, typically have an aspect

ratio greater than one. Their confinement efficiency improves as the aspect ratio decreases and the corner radius increases. Square cross-sections are a specific case of rectangular sections, characterized by an aspect ratio of one and a corner radius ratio $2R_c/b < 1$. The efficiency of square sections is primarily influenced by the degree of edge sharpness. Circular cross-sections, another special case of rectangular sections, have both an aspect ratio and a corner radius ratio of one. These sections are particularly well-suited for FRP wrapping, as stress is uniformly distributed across the entire cross-section, making all areas effective in resisting confinement forces [22].

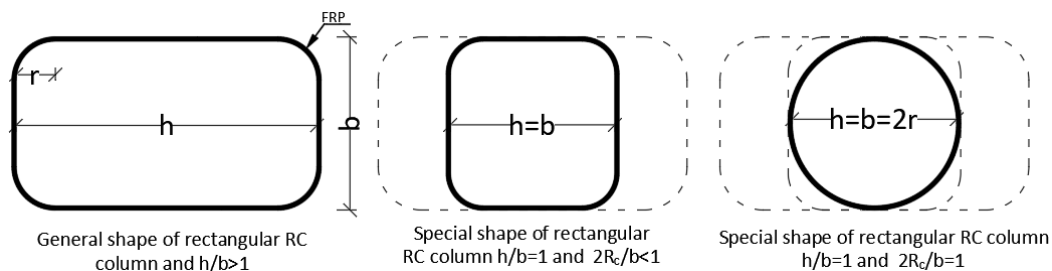


Figure 6. Rectangular cross sections and its special shapes

4.3. Results of parametric study

The relationship between maximum confined compressive strength and the ductility of concrete is illustrated in Figures 7a and 7b for three confined rectangular cross-sections with varying rounded corner radii. According to the figures, the confined peak strength of concrete exhibits significant variation with different aspect ratios.

The column with dimensions 300×300 mm and an aspect ratio of 1 demonstrates a higher maximum stress

compared to the other two columns. Conversely, the section with dimensions 300×600 mm and an aspect ratio of 2 shows lower confined stress at the same corner radius. As shown in Figure 7b, the ultimate confined strain of concrete remains relatively unaffected by changes in aspect ratio. Consequently, the aspect ratio significantly impacts the axial strength of confined FRP-wrapped RC columns, thereby influencing the effectiveness of the corner radius. Furthermore, as the cross-sectional aspect ratio increases, the influence of the corner radius diminishes [23].

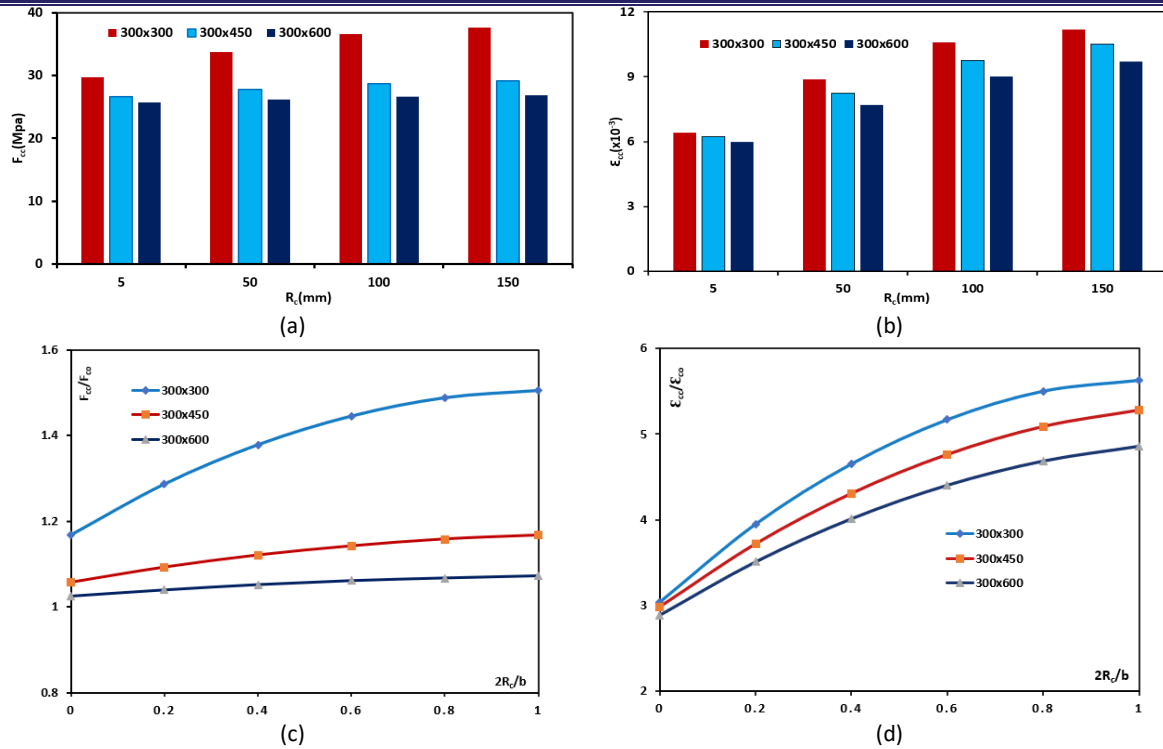


Figure 7. Relationship between strength and ductility with corner radius for various aspect ratio, (a) normalized peak strength with corner radius, (b) maximum confined strain with edge corner, (c) normalized strength with corner radius ratio, (d) normalized strain with corner radius ratio

The normalized peak stress and strain, defined as the ratios of peak stress and strain to the unconfined stress and strain of concrete (F_{cc}/F_{co} and $\epsilon_{cc}/\epsilon_{co}$), are shown in Figures 7c and 7d, respectively, as functions of the corner radius ratio for various aspect ratios. The figures indicate that the corner radius significantly influences square cross-sections, improving confinement efficiency; however, its effect diminishes as the aspect ratio

increases. Additionally, for ultimate confined compressive strain, the aspect ratio does not substantially affect the effectiveness of the corner radius, as depicted in Figure 7d. The analytical results presented in Table 6 and Figure 8 demonstrate the influence of varying corner radii on the peak compressive strength (F_{cc}) and ultimate strain (ϵ_{ccu}) of rectangular RC columns strengthened with FRP jackets.

Table 4. Results of the analytical parameters

| Sections mm | R_c/b | F_{cc} (Mpa) | | | | | | ϵ_{ccu} (%) | | | | | |
|-------------|---------|-------------------|-------|------------------|-------|----------------------|-------|----------------------|-------|------------------|-------|----------------------|--------|
| | | ACI440.2 R-17 [2] | %in | Wei&Wu Model [8] | %in | Wu et al. Model [14] | %in | ACI440.2R-17 [2] | %in | Wei&Wu Model [8] | %in | Wu et al. Model [14] | %in |
| 300x300 | 0 | 29.19 | 0 | 28.15 | 0 | 31.33 | 0 | 0.60 | 0 | 1.27 | 0 | 2.09 | 0 |
| | 0.1 | 32.16 | 10.17 | 31.95 | 13.50 | 33.42 | 6.67 | 0.78 | 30 | 1.34 | 5.51 | 2.03 | -2.87 |
| | 0.2 | 34.45 | 18.02 | 36.45 | 29.45 | 35.51 | 13.34 | 0.93 | 55 | 1.43 | 12.60 | 1.95 | -6.69 |
| | 0.3 | 36.13 | 23.77 | 39.66 | 40.88 | 37.60 | 20.01 | 1.0 | 66.6 | 1.53 | 20.47 | 1.88 | -10.05 |
| | 0.4 | 37.22 | 27.51 | 42.93 | 52.50 | 39.68 | 26.65 | 1.10 | 83.3 | 1.63 | 28.34 | 1.81 | -13.39 |
| | 0.5 | 37.63 | 28.91 | 45.82 | 62.77 | 41.77 | 33.32 | 1.2 | 100 | 1.73 | 36.22 | 1.74 | -16.74 |
| 300x450 | 0 | 29.21 | 0 | 26.46 | 0 | 28.53 | 0 | 0.61 | 0 | 1.17 | 0 | 1.86 | 0 |
| | 0.1 | 32.19 | 10.20 | 28.22 | 6.65 | 29.80 | 4.45 | 0.79 | 29.51 | 1.22 | 4.27 | 1.82 | -2.15 |
| | 0.2 | 34.50 | 18.11 | 30.30 | 14.51 | 31.07 | 8.90 | 0.93 | 52.46 | 1.31 | 11.96 | 1.77 | -4.84 |
| | 0.3 | 36.19 | 23.89 | 32.10 | 21.32 | 32.33 | 13.32 | 1.04 | 70.49 | 1.40 | 19.66 | 1.73 | -6.99 |
| | 0.4 | 37.28 | 27.63 | 33.73 | 27.47 | 33.60 | 17.77 | 1.10 | 80.33 | 1.49 | 27.35 | 1.69 | -9.14 |
| | 0.5 | 37.71 | 29.10 | 35.25 | 33.22 | 34.87 | 22.22 | 1.13 | 85.25 | 1.57 | 34.19 | 1.65 | -11.29 |
| 300x600 | 0 | 25.66 | 0 | 25.51 | 0 | 27.04 | 0 | 0.58 | 0 | 1.08 | 0 | 1.73 | 0 |
| | 0.1 | 26.02 | 1.40 | 26.86 | 5.29 | 27.94 | 3.33 | 0.70 | 20.69 | 1.15 | 6.48 | 1.70 | -1.73 |
| | 0.2 | 26.31 | 2.53 | 28.07 | 10.04 | 28.84 | 6.66 | 0.80 | 37.93 | 1.23 | 13.89 | 1.67 | -3.47 |
| | 0.3 | 26.54 | 3.43 | 29.11 | 14.11 | 29.74 | 9.98 | 0.88 | 51.72 | 1.31 | 21.30 | 1.64 | -5.20 |
| | 0.4 | 26.70 | 4.05 | 30.06 | 17.84 | 30.65 | 13.35 | 0.94 | 62.07 | 1.39 | 28.70 | 1.61 | -6.94 |
| | 0.5 | 26.80 | 4.44 | 30.93 | 21.25 | 31.55 | 16.68 | 0.97 | 67.24 | 1.47 | 36.11 | 1.59 | -8.09 |

The analysis examines three confinement models: ACI 440.2R-17 [2], Wei and Wu [8,14], and Wu et al. [14]. As the corner radius ratio (R_c/b) increases from 0 to 0.5, the models show notable variations in performance. Larger corner radii reduce stress concentrations at corners, enhancing confinement efficiency, which leads to improvements in both strength and ductility. Among the models, ACI 440.2R-17 [2] provides conservative estimates, particularly for columns with higher aspect ratios, while the Wei and Wu model predicts greater gains in F_{cc} and ϵ_{ccu} , reflecting improved confinement behavior. The Wu et al. model [14], although accounting for geometric factors, tends to overestimate peak strength, especially in smaller sections. The ultimate strain proves more responsive to changes in corner radius, underscoring the role of FRP in enhancing ductility. For design purposes, the Wei and Wu model strikes a balance between accuracy and safety [24].

Furthermore, a comparative analysis of peak confined strength and ductility for columns with aspect ratios of 300×300 mm, 300×450 mm, and 300×600 mm reveals that ACI 440.2R-17 [2] often underestimates confinement effects for smaller aspect ratios but overestimates them for larger ones. In contrast, the Wei and Wu [8] model offers more balanced and realistic predictions, particularly in capturing the influence of corner geometry on peak compressive strength.

The effect of the corner radius ratio on the shape factor, or the effective confinement area ratio, is illustrated in Figures 9a and 9c, based on various confinement models and corner radii. According to Figure 9a, rounded corners improve the effective confinement area of rectangular cross-sections, particularly for sections with smaller aspect ratios. For evaluating the shape factor, five analytical models were utilized, including the ACI 440.2R-17 [2] proposed model, Lam and Teng's [13] model, Al-Salloum and Youssef's model [7], the FIB 2019 [21] proposed model, and the model by Youssef et al. [18] and Pimanmas and Saleem [19]. As shown in Figure 9c, four of these models closely agree, while the Pimanmas and Saleem model diverges significantly for larger corner radius ratios. The relationship between the confinement area and cross-sectional aspect ratios is presented in Figure 9b for three corner radius ratios. It is evident that larger corner radius ratios and smaller aspect ratios significantly enhance the effective confinement area. Additionally, the impact of edge sharpness on the theoretical axial load capacity of RC columns is investigated and shown in Figure 9d. The axial compression load capacity of FRP-wrapped rectangular RC columns is directly proportional to the corner radius [23,24].

4.3.1. Stress-strain curves

The stress-strain curves of FRP-confined rectangular reinforced concrete (RC) columns with varying cross-sectional aspect ratios (e.g., 1, 1.5, and 2) and corner radii (e.g., $R_c=30$ mm, 90 mm, and 150 mm) are compared with those of unconfined concrete, as illustrated in Figures 10a, 10b, and 10c. Unconfined concrete demonstrates brittle compression behavior, characterized by a sharp peak stress followed by a rapid decline and limited axial strain. In contrast, FRP-wrapped RC columns exhibit significantly enhanced compression performance, including increased maximum strength and greater ductility. The confinement efficiency in rectangular cross-sections improves with larger corner radii, which critically influence the axial stress-strain response. Analytical curves show that the $R_c=30$ mm configuration yields lower peak axial stress and reduced ductility compared to larger corner radii. The $R_c=90$ mm and $R_c=150$ mm configurations substantially enhance both strength and ductility, with the $R_c=150$ mm configuration achieving more uniform stress distribution and reduced stress concentrations at the corners. This leads to higher peak confined compressive strength and improved ductility. These findings emphasize the importance of incorporating rounded corners to enhance confinement efficiency and mitigate stress concentrations in FRP-confined rectangular RC columns.

The axial stress-strain behavior of FRP-wrapped RC columns with dimensions of 300×300 mm and an aspect ratio of $h/b=1$, including a corner radius ratio of $R_c/b=0.1$, is illustrated in Figure 10d using three analytical models: the ACI recommended model [2], the Wei and Wu model [8], and the Wu et al. model [14]. The curve generated by the ACI model exhibits lower initial stiffness compared to the other two models, although the differences in ultimate strength are minimal.

Conversely, the Wu et al. model overestimates ductility relative to the other models. While its overall behavior is similar to that of the Wei and Wu model, the transitional point between elastic and plastic behavior differs. The Wei and Wu model represents an intermediate response between the ACI and Wu et al. models, with results closely aligned to both. The initial slopes of the ACI and Wei and Wu models are identical, corresponding to the elastic modulus of unconfined concrete, E_c . All three models provide comparable predictions for the ultimate confined compressive strength of concrete, confirming their reliability for modeling rectangular cross-sections. Each model comprises two mathematical branches: an initial parabolic segment followed by a linear portion. This study primarily emphasizes the ACI model, with many parameters derived from its formulations.

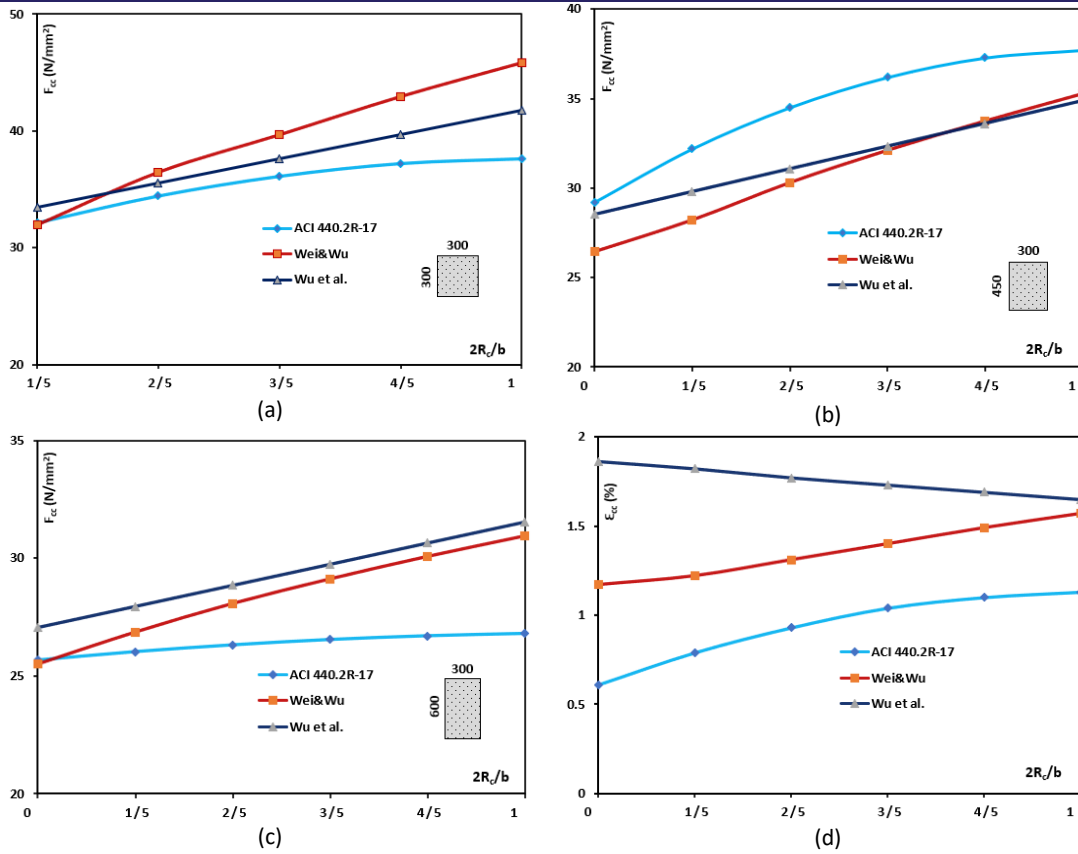


Figure 8. Relationships between peak confined stress and strain for various aspect ratios based on three confinement models.

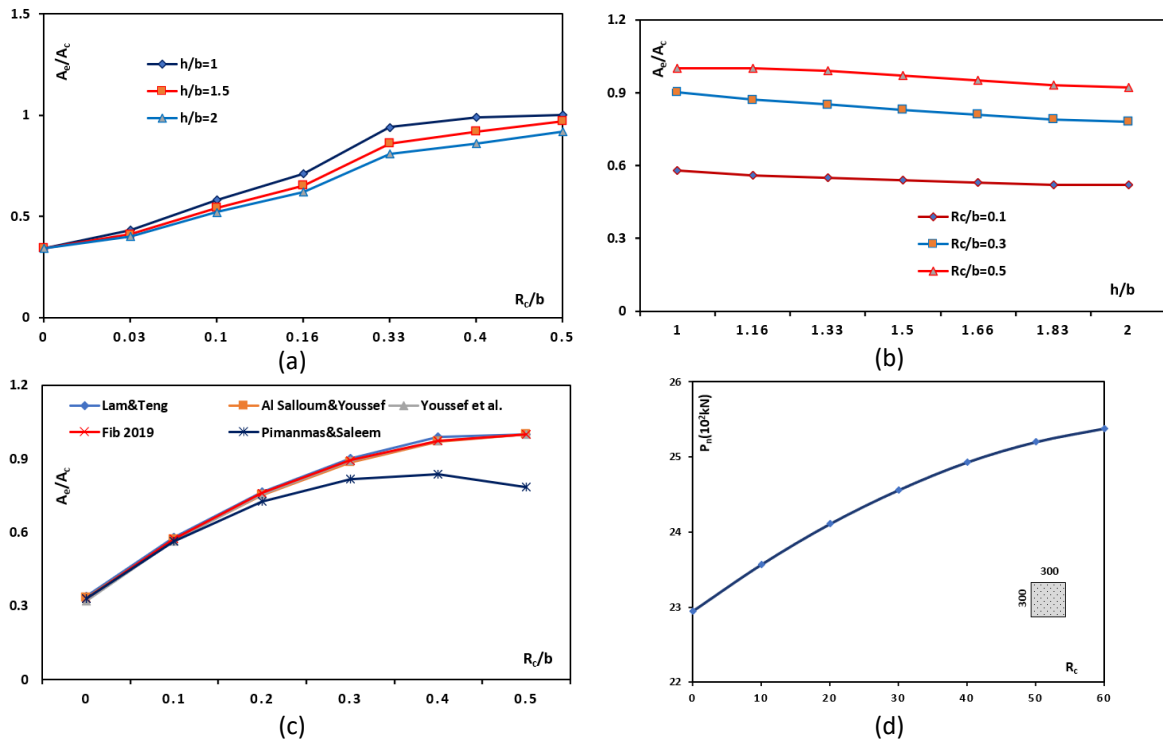


Figure 9. (a) Relationship between confinement area ratio with corner radius ratio, (b) shape factor and aspect ratio, (c) shape factor and corner radius ratio, (d) nominal axial load capacity and corner radius

According to Figure 10, the effectiveness of the corner radius in rectangular FRP-confined RC columns is influenced by the cross-sectional aspect ratio. For smaller aspect ratios (e.g., $b/h=1$), the impact is pronounced, leading to significant increases in both strength and

ductility. As illustrated in Figure 10a, the maximum stress and strain exhibit considerable differences. However, for larger aspect ratios, such as $h/b=2$, the influence of the corner radius is less pronounced, as shown in Figure 10c. In this case, the stress and strain values for the three

corner radii are similar, indicating that the effect of the corner radius diminishes as the aspect ratio increases.

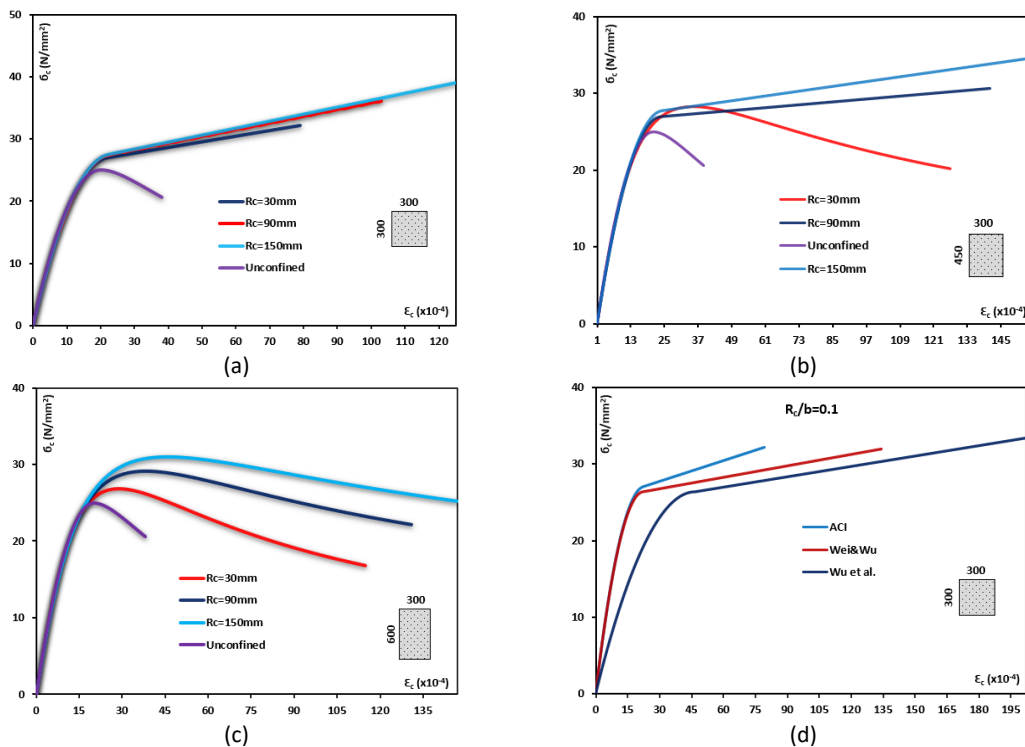


Figure 10. Stress-strain curves based on corner radius, (a) square RC column, (b) rectangular section with aspect ratio of 1.5, (c) rectangular section with aspect ratio of 2, (d) comparison of stress-strain based three models

5. Conclusions

This paper presents a comprehensive analytical investigation into the influence of corner radius on the axial compressive behavior of rectangular reinforced concrete (RC) columns wrapped with fiber-reinforced polymer (FRP) jackets. The findings highlight the significant impact of edge sharpness on confinement efficiency, which directly affects both the strength and ductility of RC columns subjected to pure axial loads. The study evaluates rectangular cross-sectional shapes with aspect ratios of 1.0, 1.5, and 2.0, along with six corner radii (0, 30, 60, 90, 120, and 150 mm). Established analytical models are utilized to examine key parameters, including the shape factor, maximum confined compressive strength, confined strain capacity of concrete, and nominal theoretical axial load capacity. The results indicate that edge sharpness plays a critical role in determining the stress distribution and overall performance of FRP confinement. Larger corner radii improve confinement efficiency by reducing stress concentrations at the edges and expanding the effective confinement area, leading to higher peak compressive strength and enhanced ductility in rectangular sections. Conversely, sharp corners restrict the distribution of lateral confining stresses, thereby diminishing the effectiveness of FRP wraps. The influence of corner radius is most significant in square cross-sections with an aspect ratio of 1.0, where it markedly affects axial strength capacity. In contrast, for rectangular sections with higher

aspect ratios, its impact decreases as stress distribution becomes less sensitive to edge geometry. Among the analytical models evaluated, the Wei and Wu [8] model provided a well-balanced prediction of both strength and ductility, demonstrating strong consistency with improved confinement behavior across various corner radius.

The ACI 440.2R-17 [2] model yielded conservative estimates, particularly for columns with smaller corner radii, while the Wu et al. [14] model tended to overestimate strength, especially for columns with lower aspect ratios. These variations highlight the critical need to select an appropriate analytical model tailored to specific geometric configurations and loading conditions when designing FRP-confined RC columns. When the corner radius reaches 150 mm, a square section exhibits confinement behavior similar to that of a circular section, offering enhanced performance due to the uniform distribution of lateral stresses at the corners. This finding underscores the advantages of rounding corners to maximize the effectiveness of FRP wraps in retrofitting and strengthening applications. Additionally, the results show that the shape factor—defined as the ratio of the effective confinement area to the total cross-sectional area—increases significantly with larger corner radii, particularly in square and low-aspect-ratio rectangular sections. In conclusion, this study emphasizes the critical role of corner geometry in the design and retrofitting of rectangular RC columns with FRP confinement.

Declaration of Interest Statement

The authors declare that there is no conflict of interest regarding the publication of this article. No financial, professional, or personal relationships influenced the research, analysis, or conclusions presented in this study.

Acknowledgement

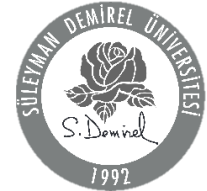
The authors would like to express their gratitude to Süleyman Demirel University for providing the necessary resources and support for this research. Special thanks to the Department of Civil Engineering for their valuable guidance and insights.

References

- [1] Rasheed, H. A. (n.d.). Strengthening design of reinforced concrete with FRP.
- [2] American Concrete Institute. (2017). Guide for the design and construction of externally bonded FRP systems for strengthening concrete structures. ACI 440.2R-17.
- [3] Cao, Y. G., Jiang, C., & Wu, Y. F. (2016). Cross-sectional unification on the stress-strain model of concrete subjected to high passive confinement by fiber-reinforced polymer. *Polymers (Basel)*, 8(5), 186. <https://doi.org/10.3390/polym8050186>
- [4] Eid, R., & Paultre, P. (2017). Compressive behavior of FRP-confined reinforced concrete columns. *Engineering Structures*, 132, 518–530.
- [5] Jiang, J., Li, P., & Nisticò, N. (2019). Local and global prediction on stress-strain behavior of FRP-confined square concrete sections. *Composite Structures*. <https://doi.org/10.1016/j.compstruct.2019.111205>
- [6] Wang, L. M., & Wu, Y. F. (2008). Effect of corner radius on the performance of CFRP-confined square concrete columns: Test. *Engineering Structures*, 30, 493–505.
- [7] Al-Salloum, Y. A. (2007). Influence of edge sharpness on the strength of square concrete columns confined with FRP composite laminates. *Composite Structures*, 38, 640–650.
- [8] Wei, Y. Y., & Wu, Y. F. (2012). Unified stress-strain model of concrete for FRP-confined columns. *Construction and Building Materials*, 26, 381–392.
- [9] Shayanfar, J., & Barros, J. A. O. (2024). Design-oriented model of unified character to determine softening–hardening stress–strain behavior of FRP-confined concrete columns of general cross section. *Journal of Composites for Construction*. <https://doi.org/10.1061/JCCOF2.CCENG-4772>
- [10] Hognestad, E. (1951). A study of combined bending and axial load in RC members. University of Illinois, *Engineering Experiment Station Bulletin Series*, (399).
- [11] Sultan, W. H., & Hamza, D. M. (2023). Formulation of mathematical model for stress-strain relationship of normal and high strength concrete under compression. *Civil and Environmental Engineering*, 19, 119–133.
- [12] Jacques, E., Lloyd, A., & Saatcioglu, M. (2013). Predicting reinforced concrete response to blast loads. *Canadian Journal of Civil Engineering*, 40, 427–444.
- [13] Lam, L., & Teng, J. G. (n.d.). Design-oriented stress-strain model for FRP-confined concrete in rectangular columns. *Journal of Reinforced Plastics and Composites*, <https://doi.org/10.1177/073168403035429>
- [14] Wu, G., Wu, Z. S., & Lü, Z. T. (2007). Design-oriented stress-strain model for concrete prisms confined with FRP composites. *Construction and Building Materials*, 21, 1107–1121.
- [15] Rasheed, H. A. (2014). Strengthening design of reinforced concrete with FRP. <https://doi.org/10.1201/b17968>
- [16] Liao, J. J., Zeng, J. J., Zhuge, Y., Zheng, Y., Ma, G., & Zhang, L. (2023). FRP-confined concrete columns with a stress reduction-recovery behavior: A state-of-the-art review, design recommendations, and model assessments. *Composite Structures*, <https://doi.org/10.1016/j.compstruct.2023.117313>
- [17] Abbasnia, R., & Ziaadiny, H. (2015). Experimental investigation and strength modeling of CFRP-confined concrete rectangular prisms under axial monotonic compression. *Materials and Structures/Materiaux et Constructions*, 48, 485–500.
- [18] Youssef, M. N., Feng, M. Q., & Mosallam, A. S. (2007). Stress-strain model for concrete confined by FRP composites. *Composite Structures*, 38, 614–628.
- [19] Saleem, S., Pimanmas, A., Qureshi, M. I., & Rattanapitikon, W. (2021). Axial behavior of PET FRP-confined reinforced concrete. *Journal of Composites for Construction*. [https://doi.org/10.1061/\(ASCE\)CC.1943-5614.0001092](https://doi.org/10.1061/(ASCE)CC.1943-5614.0001092)
- [20] Janwaen, W., Barros, J. A. O., & Costa, I. G. (2019). A new strengthening technique for increasing the load carrying capacity of rectangular reinforced concrete columns subjected to axial compressive loading. *Composite Structures*, 158, 67–81.
- [21] Ali, O., Abbas, A., Khalil, E., & Madkour, H. (2021). Numerical investigation of FRP-confined short square RC columns. *Construction and Building Materials*.

<https://doi.org/10.1016/j.conbuildmat.2020.122141>

- [22] Wu, Y. F., & Wei, Y. Y. (2010). Effect of cross-sectional aspect ratio on the strength of CFRP-confined rectangular concrete columns. *Engineering Structures*, 32, 32–45.
- [23] Noorzad, A. J., & Dilmaç, H. (2024). Structural behavior of RC columns retrofitted with FRP under axial load. *Journal of Structural Engineering & Applied Mechanics*, 7(4), 315–342. <https://doi.org/10.31462/jseam.2024.04315342>
- [24] Noorzad, A. J., & Dilmaç, H. (2024). Analytical study of structural behaviour of RC columns strengthened with CFRP wraps under axial load. Proceedings of the 2nd International Symposium on Innovations in Civil Engineering and Technology (I Civil 2024), October 30–November 1, 2024, Isparta, Turkey. <https://iciviltech2024.sdu.edu.tr/>



Comparison of offshore fish cage flotation systems designs using finite element method

Mehmet Emin Özdemir^{a,*}, Şevval Öztürk^b, Sevil Ay^c, İrem Mirzaloğlu^d, Merve Terzi^e, Murat Yaylacı^f

^aDepartment of Civil Engineering, Cankiri Karatekin University, Çankırı, Turkey

^bDepartment of Civil Engineering, Recep Tayyip Erdogan University, Rize, Turkey

^cDepartment of Civil Engineering, Artvin Coruh University, Artvin, Turkey

^dDepartment of Civil Engineering, Recep Tayyip Erdogan University, Rize, Turkey

^eDepartment of Civil Engineering, Istanbul Rumeli University, İstanbul, Turkey

^fDepartment of Civil Engineering, Recep Tayyip Erdogan University, Rize, Turkey

Highlights

- Finite element analysis of offshore structures
- Use of High-Density Polyethylene (HDPE) in cage systems
- Comparison of design geometries of floating collar systems

Abstract

Cage fishing is a sustainable production method that enables the controlled rearing of fish populations through cage systems established in inland waters or seas. Threats such as increasing environmental pollution, global warming, and irresponsible hunting negatively affect marine populations. This method offers significant advantages in meeting the need for seafood in a controlled and healthy way. To benefit from cage fishing effectively and healthily, the necessary conditions must be provided optimally, thus creating a suitable environment. However, the performance of cage systems is directly affected by environmental conditions, requiring designs to be analyzed under environmental effects. This study examined the designs of stable floating structures that ensure cage systems remain stable in the desired position and serve as a safe platform in situations requiring intervention. Floating structures with different geometric designs used in the application were analyzed using the finite element method under varying current speeds (0.5 m/s, 0.7 m/s, 1 m/s), and the results were compared. ANSYS Workbench, a software program based on the finite element method, was used during the analyses. In this context, it aims to provide information that can guide design decisions before implementation to prevent problems that may occur with the data obtained.

Keywords: Finite element method, cage systems, computational fluid dynamics

Information

Received:

15.01.2025

Received in revised:

31.01.2025

Accepted:

31.01.2025

1. Introduction

Although not as ancient as land-based farming, the history of aquaculture dates back to 3000 years ago. However, it is less developed than as land farming and contributes less to production. With the development of technology, aquaculture, in other words cage fishing, has also developed in the last 50 years and has contributed to commercial changes and developments in aquaculture. It can be said that these changes and developments were caused by factors such as population growth, increased welfare, urbanization, and increased demand for aquaculture protein sources.

The development of cage systems has been progressively modernized over the last 50 years, along with the development of the salmon farming industry. In this regard, cages have been designed to create protected areas in onshore waters. The designed cages were made of wood steel, and plastic [1]. Cage fishing can be done in different environments, such as inland waters and seas. Factors such as wave amount, water temperature, current strength, and wind intensity vary in inland waters or seas. In this case, the cage and fastening systems to be installed must be designed carefully, considering the specified factors [2]. Today, cage systems used in aquaculture are generally seen as fixed, floating, submersible, and underwater systems. Each of these systems has its advantages and disadvantages. The most

*Corresponding author: meozdemir@karatekin.edu.tr (M. E., Özdemir), +90(376) 213 26 26 - 8285

widely used system worldwide is the floating cage system due to its versatility and flexible design options [3]. Cage systems are used in different structures and different ways. Mesh net bags can be expressed in various ways, such as being flexible or rigid, the way the net is woven according to the shape of the taut net bag, or whether it is knotted. Depending on their swimming position, they are grouped into underwater swimming and surface floating cage systems. In addition, their applications and uses are common in circular, square, and polygonal shapes. The purpose of cage systems is to maximize the water mass in the existing resource storage [4]. The elements that make up truss systems generally consist of three main groups. These are: net cage, a net bag whose open part remains above the water; Floating collar, elements that provide swimming around the system; and Mooring systems, a mooring system that connects the system to the land or the bottom. These elements primarily operate under the influence of current.

There are many studies on cage systems. Some studies that have contributed to the literature are summarized below. Li et al. (2013) investigated the dynamic responses of floating fish cages to horizontal waves and currents using ABAQUS software and observed large geometric deformations and movements in the buoys and nets, and emphasized that the friction forces in the nets can significantly affect the dynamic movements of the buoy [5]. Liu et al. (2019) evaluated the structural strength and failure of the floating collar of single-point mooring fish cages based on the finite element method and stated that static analysis, vibration analysis and fatigue analysis of FEM can be preferred as reliable ways to evaluate the structural strength and failure for the floating system [6]. In their study examining fluid-structure interactions in cage-based aquaculture, Xu and Qin summarize studies showing how ocean environmental loads can affect offshore aquaculture cages and fish swimming behavior [7]. Chen et al. (2022) used numerical and experimental methods to study the fluid-structure interaction (FSI) problem of a wedge structure with stiffeners colliding with water during the free-falling water ingress process, and comprehensively analyzed the impact response results obtained by numerical simulation and experiments, including displacement, velocity, acceleration, impact pressure, deformation, structural stresses, and total forces on the wedge, taking into account the hydroelasticity effects under different free-fall height conditions [8]. Shaik et al. (2023) analyzed the hydrodynamic behavior of open-net offshore fish cages of single, double and quadruple cage systems exposed to regular sinusoidal waves with Ansys software. The analysis results concluded that the four-cage system performed better than other cage configurations [9].

Before analyzing the floating collar system with FEM, the model geometry must be created accurately in the digitized environment. In this stage, the most suitable

Veigas et al. (2024) investigated the hydrodynamic behavior of a cage exposed to a steady current using a fluid-structure interaction model. As a result of the study, they stated that there were decreases in flow within the network and downstream, consistent with previous experimental findings and research, and that knotted networks gave better results than knotless networks in line with mechanical analysis [3].

The analysis of the behavior of the floating collars of the open sea fish cages, which are the subject of this study, when exposed to the current effect was made using the finite element method. The floating collars are connected to the mooring systems to ensure the net cage is stable in and above the water. Floating collars are produced in various shapes and sizes according to needs and design conditions. In general, the most common floating collar shapes are circular and angled. In the study, two different floating collar designs, circular and quadrangular, were made and modeled.

The data obtained as a result of the study is intended to provide valuable data to designers regarding the design of floating collars, one of the most important elements of cage fishing systems, and their positioning according to the direction of the current.

2. Materials and Method

This study conducted a Fluid-Structure Interaction (FSI) simulation using ANSYS Fluent. FSI simulation is a method that combines the effects of hydrodynamic loads on the model with structural mechanics. The loads calculated in Computational Fluid Dynamics (CFD) are transferred to the mechanical model (FEM) for this combination. This simulation (FSI) is an approach that integrates the effects of hydrodynamic forces on the structure with structural analysis. The forces obtained with the help of simulation were transferred to the Finite Element Model (FEM) used for structural analysis. Analyses of the systems were performed based on the finite element method.

The Finite Element Method (FEM) is an influential numerical analysis method used to perform complicated physical and mechanical problems in engineering applications. This method allows a system with a complex geometry to be easily analyzed by breaking it down into smaller and easier-to-solve finite elements. FEM is a method that has proven its reliability in terms of interdisciplinary analyses. Researchers have examined nanoscale analyses [10, 11], biomechanical studies [12-15], and complex engineering problems [16-18] with this method and presented their results to the literature.

geometry representing the system is created, and the most optimal finite element types are selected when creating the mesh structure. Specifying the appropriate finite element type and size greatly affects the

correctness of the analysis results. The mesh structure is enhanced using the selected element types, and the material properties of the model are defined. Then, the loading and boundary conditions to be imposed on the system are specified. After all these steps are accomplished, the FEM analysis of the model is conducted. The findings of the FEM analysis enabled the detection of critical factors that should be considered in the design of Floating Collar systems and aimed to guide the pre-implementation process.

2.1. Geometry

The floating collars of the systems were designed with a height of 1 meter and a width of 1.11 meters to fit the grid element (Figure 1a). For the floating collars to act as a floating structure on the water, 4 independent hollow pipe geometries with a wall thickness of 2 mm were created. These pipes were connected with the help of another geometry on top, and a hollow structure was designed. A three-dimensional circular floating system was formed by rotating around a 5 m diameter axis. Similarly, a three-dimensional angular floating system was formed by moving it around axes of 5x5 m (Figure 1b, c).

To successfully simulate the flow of water in CFD analysis, a flow field surrounding the model must be defined. This flow area should allow water to move freely around the floating collar system. The correct application of boundary conditions in the analysis is also important to represent the physical behavior of the flow in the most realistic way (Figure 2).

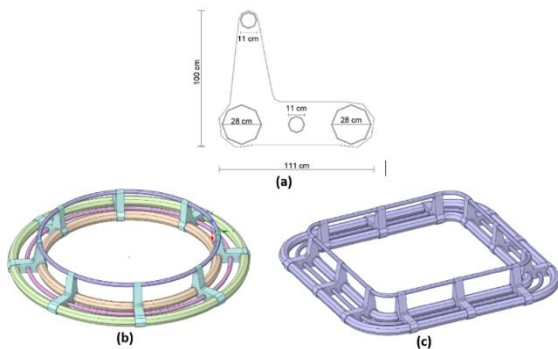


Figure 1. a) Cross section of floating collar models, b) circular floating collar system, c) angular floating collar system

2.2. Mesh structures

The models were transferred from AutoCAD to ANSYS Fluent for finite element analysis, and a separate meshing process was performed for each model. To obtain realistic and reliable results, great attention has been paid to correctly selecting the dimensions of the finite elements that comprise the mesh structure and using the appropriate finite element types. Each finite element is defined in this direction by a tetrahedral (tetrahedron)

element with eight nodes for the mesh configuration. These finite elements suit displacement and rotational movements in the x, y, and z axes. The number of nodes and elements of each system are summarized as follows: The circular floating collar system has a total of 50633 nodes and 167616 finite elements, and the flow field designed by the geometry of the circular floating collar system has a total of 165929 nodes and 912552 finite elements (Figure 3). The angular floating collar system has 136863 nodes and 489283 finite elements; the flow field designed by the angular floating collar system geometry has 387075 nodes and 2128071 finite elements (Figure 4). Additionally, each mesh structure is modeled to have isotropic, homogeneous, and linear elastic properties.

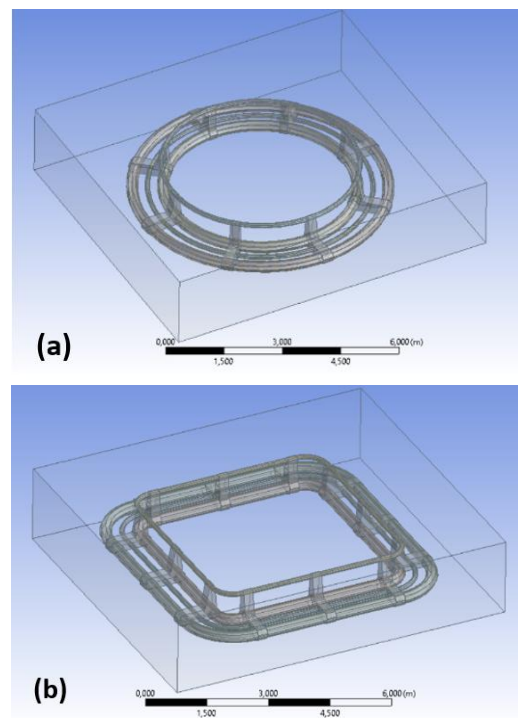


Figure 2. CFD analysis models a) circular floating collar system, b) angular floating collar system

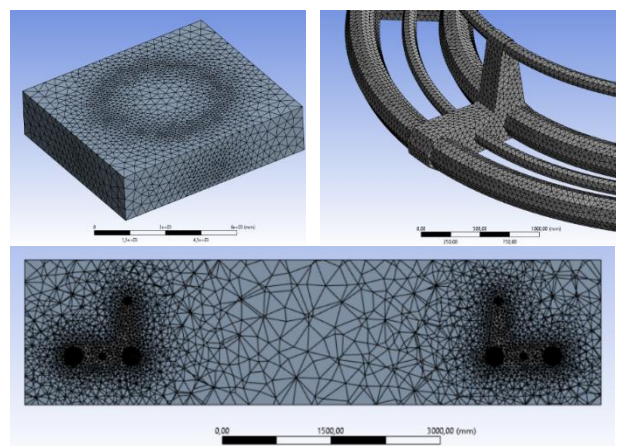


Figure 3. Mesh structures of the circular floating collar system and flow fields

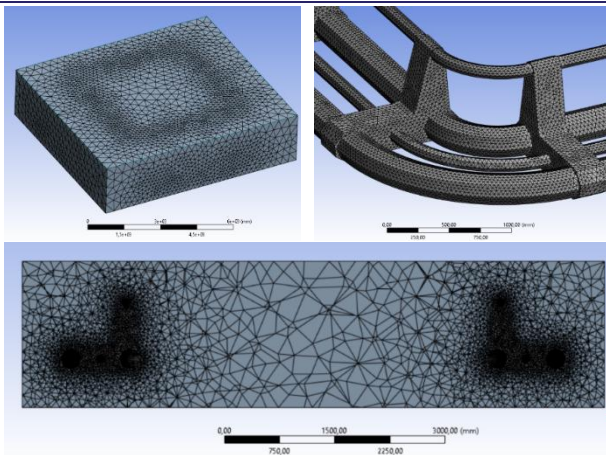


Figure 4. Mesh structures of the angular floating collar system and flow fields

2.3. Material properties, boundary and loading conditions

The mechanical properties of the materials for the floating collar systems and flow areas were specified in compliance with the literature. All the materials identified are such that they are isotropic, homogeneous, and have linear elastic properties, and were appropriately assigned to each site. The mechanical properties of the material used in the present study are provided in detail in Table 1.

Table 1. Material properties

| | Density (kg/m ³) | Young modulus (E) (MPa) | Poisson's ratio(v) |
|----------------------------------|------------------------------|-------------------------|--------------------|
| High-Density Polyethylene (HDPE) | 950 | 1000 | 0.46 |

Before proceeding to the finite element analysis, the model's boundary conditions were determined, and simulations were performed for various loading scenarios. At first, CFD analyses were conducted to determine the pressure values generated by the fluid on the models. During the CFD analyses, no deformation analysis was conducted on the models; only the pressures generated on the surface of the models depending on the flow velocity were calculated. In the analyses, the "water-liquid" material was selected from the Fluent material database, and the constant viscosity for this material was defined as 0.001003 kg/(m-s), with a density of 998.2 kg/m³. Within the scope of the study, the models were analyzed under three different flow velocities (0.5 m/s, 1.0 m/s, and 5.0 m/s).

Analyses were performed under these defined boundary and loading conditions. The maximum stress and deformation values exposed to the floating collar systems were calculated and registered.

3. Results and Discussion

In this section, the results of mechanical analyses of floating collars designed in two different geometries under the boundary conditions explained in the previous section will be examined. As a result of the analyses, total deformation, equivalent (von Mises) stress, and equivalent strain values were obtained, and the obtained values were compared (Table 3-5). Images of the analysis results are given in Figure 6.

Table 2. Pressure magnitudes (MPa) obtained from CFD analysis and transferred to mechanical models

| | 0.5 m/s | 1.0 m/s | 5.0 m/s |
|-----------------|------------|------------|----------|
| Circular collar | 0.00021509 | 0.00085873 | 0.021361 |
| Angular collar | 0.00022346 | 0.00088937 | 0.022065 |

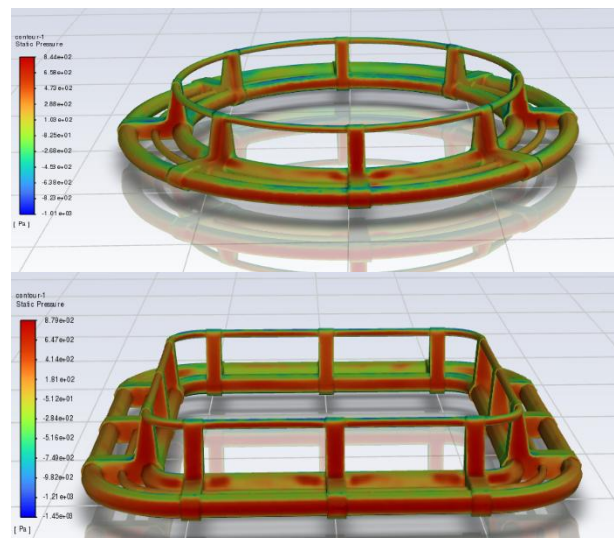


Figure 5. Pressure distributions calculated for 1.0 m/s flow velocity in CFD analysis

The CFD analysis calculated the pressure distributions formed by the fluid effect on the models, which influenced the models in the mechanical analysis. The magnitudes of the pressures obtained from the CFD analysis and transferred to the mechanical model are given in Table 2 and shown Figure 5.

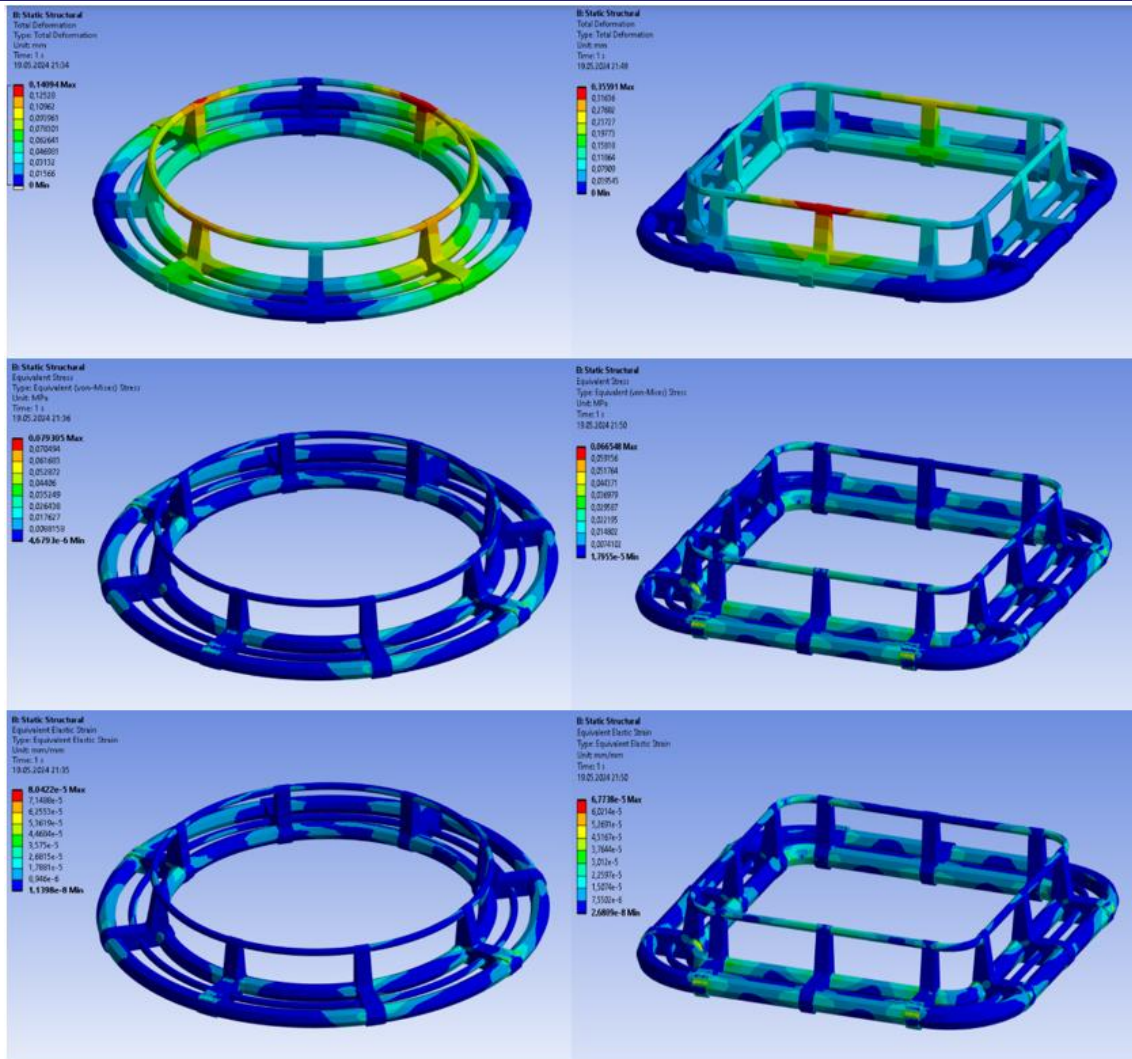


Figure 6. Analysis result images obtained from circular and angular floating collar under 0.5 m/s current speed.

Table 3. Total deformation values obtained as a result of the analysis (mm)

| | Flow velocities | | |
|-----------------|-----------------|---------|---------|
| | 0.5 m/s | 1.0 m/s | 5.0 m/s |
| Circular collar | 0.14904 | 0.56775 | 14.264 |
| Angular collar | 0.35591 | 14.237 | 35.996 |

When Table 3 is examined, the deformations occurring in both models increase as the flow velocity increases. The deformation occurring in the angular model was much larger than in the circular model. This difference can be explained by variations in the surface areas directly exposed to the flow and the fixation areas.

Table 4. Equivalent (von Mises) stress values obtained as a result of the analysis (MPa)

| | Flow velocities | | |
|-----------------|-----------------|---------|---------|
| | 0.5 m/s | 1.0 m/s | 5.0 m/s |
| Circular collar | 0.079305 | 0.31645 | 7.9069 |
| Angular collar | 0.066548 | 0.26639 | 6.6375 |

When Table 4 is examined, it is seen that the obtained stress values increase with the flow velocity. The stress values obtained for the angular collar are slightly smaller than the values obtained for the circular collar.

Table 5. Equivalent strain values obtained as a result of the analysis

| | Flow velocities | | |
|-----------------|-------------------------|------------|-----------|
| | 0.5 m/s | 1.0 m/s | 5.0 m/s |
| Circular collar | 8.0422x10 ⁻⁵ | 0.00032092 | 0.0080186 |
| Angular collar | 6.7738x10 ⁻⁵ | 0.00027116 | 0.0067562 |

When Table 5 is examined, it is seen that the obtained strain values increase with the flow velocity. The strain values obtained for the angular collar are slightly smaller than the values obtained for the circular collar.

4. Conclusions

As a result of the analysis, it was seen that there was no harm in the use of both models. The stress and strain values for the angular collar were slightly lower than those for the circular collar, indicating a slightly better performance. Angular floating collars placed perpendicular to the flow direction were subjected to more stress effects under liquid influence than circular floating collars. This situation can be solved by adjusting the position of the floating collar according to the flow direction. However, the deformation value for the angular

collar was significantly higher, particularly in the upper parts of the collar. Despite this, it does not pose a threat to the overall structural integrity. Although both models show approximately the same reactions under loads, the angular model provides slightly more space, which makes it slightly more advantageous. In addition, the analysis results showed that the use of HDPE for collar production was quite suitable.

Declaration of Interest Statement

The authors declare that they have no known competing financial interests or personal relationships that could have appeared to influence the work reported in this paper.

References

- [1] Scott, D.C.B. and Muir, J.F. (2000). Offshore cage systems-a practical overview. *Options Mediterr. Edts Muir and Basurco*, 30(79-90)
- [2] Özdemir, M.E. (2021). Solid-liquid interaction analysis of fish cages by finite element method. Master's Thesis. Recep Tayyip Erdogan University, Institute of Graduate Education, Rize, Turkey, 54 p.
- [3] Veigas, M.D., Wang, S and Soares, C.G (2024). One-way CFD/FEM analysis of a fish cage in current conditions. *Journal of Marine Science and Engineering*, 12(12), 2268. <https://doi.org/10.3390/jmse12122268>
- [4] Dikel, S. (2005). *Cage Fishing*. Adana: Çukurova University Faculty of Fisheries Publications.
- [5] Li, L., Fu, S., Xu, Y., Wang, J. and Yang, J. (2013). Dynamic responses of floating fish cage in waves and current. *Ocean Engineering*, 72, 297-303.
- [6] Liu, H.Y., Huang, X.H., Wang, S.M., Hu, Y., Yuan, T.P. and Guo, G.X. (2019). Evaluation of the structural strength and failure for floating collar of a single-point mooring fish cage based on finite element method. *Aquacultural Engineering*, 85, 32-48.
- [7] Xu, Z. and Qin, H. (2020). Fluid-structure interactions of cage based aquaculture: From structures to organisms. *Ocean Engineering*, 217, 107961.
- [8] Chen, Z., Jiao, J., Wang, Q. and Wang, S. (2022). CFD-FEM simulation of slamming loads on wedge structure with stiffeners considering hydroelasticity effects. *Journal of Marine Science and Engineering*, 10(11):1591
- [9] Shaik, A.S., Thuvanismail, N., Vijayakumar, M. and Kumar, P. (2023). Numerical investigation on different configurations of offshore fish cages in submerged conditions subjected to regular waves. *Journal of Marine Science and Application*, 22(3): 445-455.
- [10] Uzun Yaylacı, E., Özdemir, M.E., Güvercin, Y., Öztürk, Ş. and Yaylacı, M. (2023). Analysis of the mechano-bactericidal effects of nanopatterned surfaces on implant-derived bacteria using the FEM. *Advances in Nano Research*, 15(6), 567-577. <https://dx.doi.org/10.12989/anr.2023.15.6.567>.
- [11] Uzun Yaylacı, E., Yaylacı, M., Özdemir, M.E., Terzi, M. and Öztürk, Ş. (2023). Analyzing the mechano-bactericidal effect of nano-patterned surfaces by finite element method and verification with artificial neural networks. *Advances in Nano Research*, 15(2), 165-174. <https://dx.doi.org/10.12989/anr.2023.15.2.165>.
- [12] Güvercin, Y., Yaylacı, M., Dizdar, A., Özdemir, M.E., Ay, S., Yaylacı, E.U., Karahasanoğlu, U., Uygun, H. and Peker, G. (2025). Biomechanical analysis and solution suggestions of screw replacement scenarios in femoral neck fracture surgeries: finite element method. *Orthop Surg*. <https://doi.org/10.1111/os.14337>.
- [13] Benouis, A., Zagane, M.E.S., Moulgada, A., Yaylacı, M., Kacı, D.A., Terzi, M., Özdemir, M.E. and Uzun Yaylacı, E. (2024). Finite element analysis of the behavior of elliptical cracks emanating from the orthopedic cement interface in total hip prostheses. *Structural Engineering and Mechanics*, 89(5), 539-547. <https://dx.doi.org/10.12989/sem.2024.89.5.539>.
- [14] Kurt, A., Yaylacı, M., Dizdar, A., Naralan, M.E., Uzun Yaylacı, E., Öztürk, Ş. and Çakır, B. (2024). Evaluation of the effect on the permanent tooth germ and the adjacent teeth by finite element impact analysis in the traumatized primary tooth. *International Journal of Paediatric Dentistry*, 34(6), 822-831. <https://dx.doi.org/10.1111/ipd.13183>.
- [15] Zagane, M.E.S., Moulgada, A., Yaylacı, M., Abderahmen, S., Özdemir, M.E. and Uzun Yaylacı, E. (2023). Numerical simulation of the total hip prosthesis under static and dynamic loading for three activities. *Structural Engineering and Mechanics*, 86(5), 635-645. <https://dx.doi.org/10.12989/sem.2023.86.5.635>.
- [16] Yaylacı, M., Yaylı, M., Öztürk, Ş., Ay, S., Özdemir, M.E., Uzun Yaylacı, E. and Birinci, A. (2024). Examining the contact problem of a functionally graded layer supported by an elastic half plane with the analytical and numerical methods. *Mathematical Methods in the Applied Sciences*, 1-21. <https://dx.doi.org/10.1002/mma.10129>.
- [17] Sekban, D.M., Uzun Yaylacı, E., Özdemir, M.E. and Yaylacı, M. (2024). Determination of formability behavior of steel used in ships by various methods. *Structural Engineering and Mechanics*, 92(2), 189-196. <https://dx.doi.org/10.12989/sem.2024.92.2.189>.
- [18] Sekban, D.M., Uzun Yaylacı, E., Özdemir, M.E., Yaylacı, M. and Tounsi, A. (2024). Investigating formability behavior of friction stir-welded high-strength shipbuilding steel using experimental finite element and artificial neural network methods. *Journal of Materials Engineering and Performance*. <https://doi.org/10.1007/s11665-024-09501-8>.